METAL NITRIDE DIFFUSION BARRIERS FOR COPPER INTERCONNECTS

A Dissertation

by

ROY ADOLFO ARAUJO

Submitted to the Office of Graduate Studies of
Texas A&M University
in partial fulfillment of the requirements for the degree of

DOCTOR OF PHILOSOPHY

December 2008

Major Subject: Electrical Engineering

METAL NITRIDE DIFFUSION BARRIERS FOR COPPER INTERCONNECTS

A Dissertation

by

ROY ADOLFO ARAUJO

Submitted to the Office of Graduate Studies of
Texas A&M University
in partial fulfillment of the requirements for the degree of

DOCTOR OF PHILOSOPHY

Approved by:

Co-Chairs of Committee,	Haiyan Wang
	Tahir Cagin
Committee Members,	Frederick Strieter
	Takis Zourntos
Head of Department,	Costas Georghiades

December 2008

Major Subject: Electrical Engineering

ABSTRACT

Metal Nitride Diffusion Barriers for Copper Interconnects. (December 2008)

Roy Adolfo Araujo, B.S., Universidad Nacional de Ingenieria, Lima, Peru;

M.E., University of South Carolina, South Carolina

Co-Chairs of Committee: Dr. Haiyan Wang
Dr. Tahir Cagin

Advancements in the semiconductor industry require new materials with improved performance. With the introduction of copper as the interconnect material for integrated circuits, efficient diffusion barriers are required to prevent the diffusion of copper into silicon, which is primarily through grain boundaries. This dissertation reports the processing of high quality stoichiometric thin films of TiN, TaN and HfN, and studies their Cu diffusion barrier properties.

Epitaxial metastable cubic TaN (B1-NaCl) thin films were grown on Si(001) using an ultra-thin TiN (B1-NaCl) seed layer which was as thin as 1 nm. The TiN/TaN stacks were deposited by Pulsed Laser Deposition (PLD), with the TiN thickness systematically reduced from 15 to 1 nm. Microstructural studies included X-ray diffraction (XRD), transmission electron microscopy (TEM) and high resolution TEM (HRTEM). Preliminary Cu diffusion experiments showed that the TiN seed layer thickness had little or no obvious effect on the overall microstructure and the diffusion barrier properties of the TaN/TiN stacks.

Epitaxial and highly textured cubic HfN (B1-NaCl) thin films (~100 nm) were deposited on MgO(001) and Si(001) using PLD. Low resistivities (~40 μΩ-cm) were measured with a four point probe (FPP). Microstructural characterizations included XRD, TEM, and HRTEM. Preliminary Cu diffusion tests demonstrated good diffusion barrier properties, suggesting that HfN is a promising candidate for Cu diffusion barriers.

Cubic HfN (B1-NaCl) thin films were grown epitaxially on Si(001) substrates by using a TiN (B1-NaCl) buffer layer as thin as ~10 nm. The HfN/TiN stacks were deposited by PLD with an overall thickness less than 60 nm. Detailed microstructural characterizations included XRD, TEM, and HRTEM. The electrical resistivity measured by FPP was as low as 70 μΩ-cm. Preliminary copper diffusion tests showed good diffusion barrier properties with a diffusion depth of 2~3 nm after vacuum annealing at 500°C for 30 minutes.

Additional samples with Cu deposited on top of the cubic HfN/TiN/Si(001) were vacuum annealed at 500°C, 600°C and 650°C for 30 minutes. The diffusivity of copper in the epitaxial stack was investigated using HRTEM. The measured diffusion depths, $2\sqrt{Dt}$, were 3, 4 and 5 nm at 500°C, 600°C and 650°C respectively. Finally, the diffusivity of Cu into epitaxial HfN was determined to be $D = D_0 \exp(-Q/kT)\,\mathrm{cm^2 s^{-1}}$ with $D_0 = 2.3 \times 10^{-14} cm^2 s^{-1}$ and $Q = 0.52 eV$.

Dedicado a mi Madre y Padre

ACKNOWLEDGEMENTS

I first and foremost thank my Ph.D. advisor, Dr. Haiyan Wang, for the opportunity to work with her. She has been a great mentor, and I could not have chosen a better advisor. It has been a great experience being tutored by such an outstanding scientist; to learn from her broad science and engineering knowledge will benefit me throughout my life.

I want to thank Dr. Frederick Strieter. As a teacher and a friend, he continuously inspired me with invaluable discussions. Especially, I appreciated the great opportunity he gave me as a teaching assistant for his class in microelectronics fabrication.

I also thank Dr. Tahir Cagin and Dr. Mustafa Uludogan. I am very grateful for their help and patience with the simulation part of my dissertation. Their profound knowledge about computational science is already of great benefit.

I am indebted to Dr. Takis Zourntos for taking part in my committee, his suggestions and for attending my final examination.

Thanks also go to my colleagues in the Wang and Cagin groups, all of whom have provided invaluable discussion and feedback regarding the studies presented in this dissertation.

Finally, I am grateful for the funding provided through Texas A&M University that has financially supported my research and living expenses.

TABLE OF CONTENTS

Page

CHAPTER

LIST OF FIGURES

FIGURE Page

FIGURE Page

FIGURE Page

FIGURE Page

LIST OF TABLES

TABLE Page

CHAPTER I

INTRODUCTION: NITRIDE DIFFUSION BARRIERS FOR COPPER INTERCONNECTS

1.1 Introduction

Metal nitrides are useful materials with numerous current and foreseeable industrial applications. They are materials of great interest to the scientific community as well. Although most of their applications are recent, these so-called refractory nitrides have been known for over one hundred years because they have high melting points. Titanium carbonitride was first described in 1822 and identified by chemical analysis in 1850. The industrial importance of transition metal nitrides is growing rapidly because of their well established applications based on their high hardness and high melting point. These properties make them great as coatings for cutting tools and abrasives. They also show promise in fields such as microelectronics and optoelectronics [1, 2].

Some of the important applications of metal nitrides are listed below:

- Titanium nitride, Tantalum nitride and Hafnium nitride for Cu diffusion barriers
- Titanium nitride, Tantalum nitride and Hafnium nitride as the metal gate material for next generation semiconductor device.
- Silicon nitride for rotors, blades, rings, and burner tiles for gas turbines
- Titanium nitride coatings on high speed steel drill bits

This dissertation follows the style and format of Thin Solid Films.

While a wide range of applications reflect the variety of these materials and the diversity of their use in industry, in recent years nitride based thin films have attracted much research effort for improving hard coating applications, introducing them in electronic device fabrication as barriers or metal gates, and their use in optical light emitting diodes [3-8]. TiN has been extensively used as a hard wear-resistant coating for cutting tools, or as the corrosion and abrasion resistant layers on optical and mechanical components. A better understanding of the microstructure and composition of nitride films has dramatically improved some properties of these nitride films [9, 10]. As an example a nanocrystalline TiN film enhances grain boundary sliding and grain boundary diffusion related creep phenomena, and the ductility of the coatings is also improved. On the other hand, compositional designed TiN based alloys, such as cubic-phase $Ti_{1-x}Al_xN$ thin films in a state of compressive residual stress, and compositionally modulated nitride films such as multilayer and superlattices, show much higher thermal stability and better mechanical properties [11-13]. For electronic device fabrications, TiN has been widely used in semiconductor back end technology as a diffusion barrier material due to its high melting point, low resistivity, good adhesion, and ease of processing [1, 2, 14]. The introduction of Cu interconnects early this decade and the constant improvements needed in the semiconductor industry have required more efficient diffusion barrier materials in order to fulfill and continue with Moore’s Law. TaN is considered to be an even more promising candidate than TiN [15-17]. Accordingly, the processing and property correlations of TaN thin films are studied in this thesis as diffusion barriers for the next generation of Cu interconnects [18]. Similarly, HfN is also being studied as a Cu diffusion barrier. In addition to this experimental research effort, theoretical studies of the mechanical and electronic properties of TiN, TaN and HfN are explored by using *Ab-initio* computational modeling of the crystalline phases of TiN, TaN and HfN. Specifically, these calculations are performed by using Density Functional Theory and compared to experimental results from the available literature.

The nitride based materials studied and presented in this dissertation are from the transition metal nitrides family such as TiN, TaN and HfN, either as a single film layer or a multilayer structure.

1.2 Diffusion Barriers for Metal Interconnects

At the beginning of the twenty-first century, rapidly growing market needs accelerated the development of integrated circuitry (IC) with increasingly higher speeds and more functionality. To achieve the primary goal of increasing device density per chip requires shrinking of the feature size of every individual device and enhancing the overall metallization scheme to minimize interconnect wire-length distribution [19]. Resistance times capacitance (RC) time delay has replaced intrinsic device delay as the major speed limiter in sub-quarter-micron device nodes, due primarily to the increasingly higher RC time constant in the ever narrower, more-closely spaced interconnect lines. Minimizing RC delay has forced a transition from aluminum-copper (Al-Cu) and tungsten (W) interconnects with silicon dioxide (SiO_2)-based insulating layers to Cu and low dielectric constant (k) metallization schemes. This transition results in a reduction in RC time delay due to the higher conductance of Cu and lower capacitance of low *k* materials. Copper is a better choice than gold or silver. Because silver has corrosion problems and poor electromigration resistance. Gold suffers from contamination problems and high cost. Cu has lower resistivity, 1.72 μΩ-cm versus 2.7 μΩ-cm for Al, and much better electromigration resistance than Al. Higher electromigration resistance also allows for circuit operation at higher current densities in the interconnects, resulting in potentially faster circuit speed.

For interconnect lines with a thickness of about 80 nm, the resistivity of pure Cu ranges from 1.7 to around 2.0 μΩ-cm, depending on film texture and morphology as driven primarily by the processing technique used and underlying substrate. In comparison, Al lines exhibit resistivities ranging from 3.0 μΩ-cm to around 3.5 μΩ-cm. When combined with a low *k* material with a dielectric constant of 2 (compared with ~4.5 for SiO_2), the transition from the Al/SiO_2 to the Cu/low *k* node provides ~400% reduction in RC delay.

The shift to the Cu/low *k* node has generated significant challenges in the identification and development of the robust material and process technologies required to form reliable copper-based interconnects. In the case of copper, the need for a diffusion barrier/adhesion promoter is even more critical in view of the high diffusivity of Cu into Si and SiO_2. The presence of copper in silicon produces highly adverse effects, including the formation of deep trap levels that cause serious device degradation and failure. Such layers are further required due to the poor adhesion of copper not only to SiO_2, but also to the various low *k* materials under consideration for use in gigascale interconnects [4].

Furthermore, as device sizes continue their trend toward smaller features, barrier materials must provide the required performance at continually reduced thickness in order to maximize space availability for the actual copper conductor. Predictions published in the International Technology Roadmap for Semiconductors 2007 Edition, Table 1.1, reveal that the maximum allowable values for barrier thickness for coming years to be less than 5 nm in thickness.

Table 1.1. Selected target specifications of diffusion barriers for next device nodes [19].

Device Node	**2008**	**2009**	**2010**	**2011**	**2012**	**2015**
Global wiring aspect ratio (dual damascene)	2.3/2.1	2.4/2.2	2.4/2.2	2.4/2.2	2.5/2.3	2.6/2.4
Contact aspect ratio (DRAM)	17	17	>20	>20	>20	>20
Conductor effective resistivity (μΩ-cm)	3.63	3.80	4.08	4.30	4.53	5.58
Barrier cladding thickness (nm)	4.3	3.7	3.3	2.9	2.6	1.9

1.3 Predominant Diffusion Mechanisms in Diffusion Barriers

The identification of a viable barrier for Cu metallization requires establishing a fundamental understanding of the underlying mechanisms that drive atomic mobility and associated interdiffusion phenomena. It is well known that the placement of chemically different atoms in close proximity leads to atomic migration in order to lower the overall free energy and establish equilibrium. Atomic migration is typically driven by the presence of concentration differences, existence of a negative free energy of reaction, application of an electric field, availability of thermal energy, generation of a strain gradient, or a combination of some or all of these factors.

Atomic migration could result in a diffusion flux, with the net flow of atoms being characterized by a diffusion coefficient D. The latter is described by Fick's law in one dimension:

$$J = -D(\frac{dC}{dx}) \text{ ....(1.1)}$$

where C is the atomic concentration, J the atomic flux per unit area per second, and x is distance. The temperature dependence of the diffusion coefficient D takes on the form of an Arrhenius relationship:

$$D = D_0 \exp\left(\frac{-Q}{kT}\right) \text{ ....(1.2)}$$

where D_o is a constant, Q is the activation energy for diffusion, k is Boltzmann's constant, and T is the temperature in degrees Kelvin. The diffusion parameters D_o and Q implicitly contain information on the thermodynamic and kinetic properties of the diffusion mechanisms.

In the case of the Cu diffusion barrier system, three mechanisms typically dominate the diffusion barrier failure:

(a) Diffusion of copper or substrate atoms through bulk defects in the barrier.

(b) Diffusion of copper along grain boundaries of the barrier.

(c) Loss of barrier layer integrity due to a metallurgical or chemical reaction with the copper and/or substrate (Si).

Two types of bulk defects tend to contribute to diffusion: vacancies and dislocations. Diffusion resulting from vacancies, defects, and grain boundaries occurs at significantly different rates. It was experimentally observed that lattice diffusion rates are proportional to the absolute melting temperature T_m of the host material [4], with the corresponding behavior being given by the following empirical relationship:

$$D \sim AT_m \qquad (1.3)$$

where A is proportionality constant that depends on a variety of factors, including lattice structure and type of material. Diffusion rates due to atom-vacancy exchange tend to be the lowest (smallest A), thus corresponding to the slowest diffusion. Dissociated dislocations exhibit intermediate rates, whereas high-angle grain boundaries, which result from a large misfit between adjoining grains, have the highest diffusion rates (largest A). Although significant uncertainty exists in the estimated values of A, the empirical relationship above provides a reasonable estimate of diffusion rates in different materials systems. Therefore, it represents a reasonable guideline in the selection of appropriate materials for diffusion barrier applications. In particular, it indicates that materials with elevated melting points could act as better barriers [4].

The previous discussion clearly states the critical role that microstructure plays in the resulting diffusion barrier performance of the barrier material. Film microstructure can be categorized as single crystal, polycrystalline, nanocrystalline (i.e. polycrystalline with grain size below ~5 nm), and amorphous (no long-range atomic periodicity), as shown schematically in Figure 1.1. Polycrystalline barriers tend to yield the poorest barrier performance and are thus the least desirable for diffusion barrier applications. This assessment is especially true for barriers with grain sizes on the order of the film thickness or films with columnar structure. The latter exhibit grain boundaries that extend throughout the entire film thickness and are mostly normal to the substrate surface, as shown in Figure 1.1c, this structure provides an effective pathway for copper diffusion.

Single crystal diffusion barriers are ideal barriers. However, material and process constraints, including lattice mismatch with the underlying substrate and thermal budget limitations, make it unlikely to deposit barriers in single crystal form. Therefore, stable nanocrystalline or amorphous materials are more probable for diffusion barrier applications, especially in light of material and process limitations.

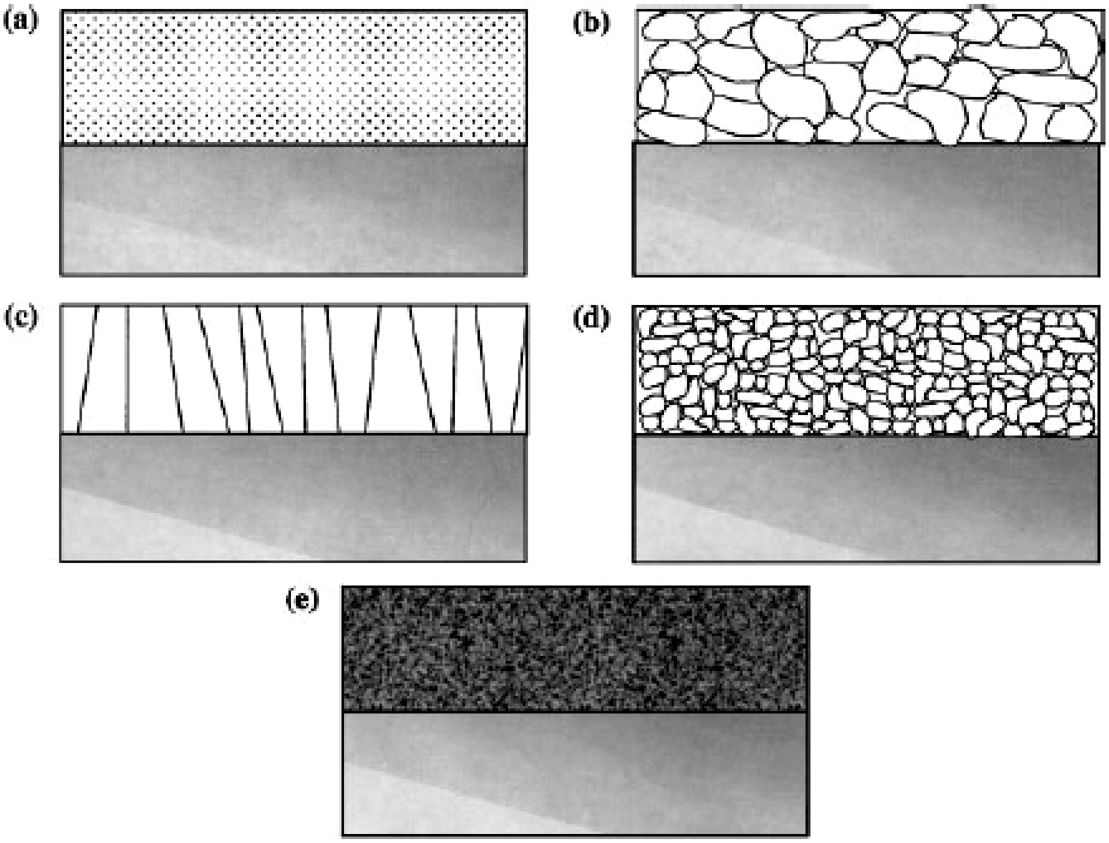

Figure 1.1. Barrier microstructure can be categorized as (a) single crystal, (b) polycrystalline, (c) polycrystalline columnar, (d) nanocrystalline, and (e) amorphous.

1.4 Titanium Nitride and Titanium Diffusion Barriers

For Al based metallization, titanium (Ti) and its nitride (TiN) were the most commonly used diffusion barriers/adhesion promoters to improve the wettability and texture of the aluminum interconnect and enhance its mechanical stability. Ti/TiN was also applied in the contact plug to reduce contact resistance and improve W adhesion, whereas TiN is further used to protect the contact from the fluorine-containing CVD W precursors. The effectiveness of TiN barriers for Al was attributed to the improved barrier upon processing. TiN was exposed to air prior to the Al deposition, leading to oxygen stuffing. The oxygen subsequently reacted with Al to form an aluminum oxide phase, which blocked any further material transport through the TiN barrier. The same processing mechanism does not work for Cu [20]

As such, the possibility of extending their applicability to copper based interconnects represents a highly attractive option, both for technical and economic reasons. Unfortunately, Ti and TiN have not been able to provide adequate copper barrier performance for a film thickness of or below 20 nm [21]. A Ti barrier failed primarily through a metallurgical reaction with copper, which occurred readily at 350°C [22], while TiN typically failed through grain boundary diffusion.

TiN deposited by either physical vapor deposition (PVD) or inorganic chemical vapor deposition (CVD) techniques exhibited mostly columnar type morphology, with grain boundaries running along the entire thickness of the TiN film. This morphology provided a fast diffusion pathway for copper migration across the barrier to the underlying substrate.

TiN films grown by metal organic CVD (MOCVD) techniques, on the other hand, displayed an amorphous microstructure and were thus thought to provide improved barrier performance due to the absence of grain boundary pathways for fast Cu diffusion. Unfortunately, the presence of high levels of carbon, oxygen, and hydrogen contaminants for films deposited below 450°C led to the formation of a low-density, high-resistivity, and porous TiN microstructure that acted as a poor barrier to Cu diffusion. Efforts to remedy this problem included the use of plasma-assisted MOCVD growth and the application of post-deposition annealing treatments, in the presence or absence of a plasma environment. However, these attempts did not yield the optimized TiN barrier performance needed [23-25].

Other efforts included the implementation of a cycled deposition approach, whereby multiple deposition and plasma treatment cycles were sequentially performed. This approach was successful at enhancing the stability, lowering the resistivity, and improving the barrier properties of MOCVD TiN. The resulting performance of the post-treated MOCVD TiN films was equivalent to that of their PVD analogs, with both sets of barriers surviving thermal stressing at temperatures up to 650±°C. Unfortunately, the TiN thickness used in this study was 50 nm and was thus too thick to be considered for sub-quarter-micron device applications [4].

Another approach, using a pulsed laser deposition (PLD) technique studied the diffusion of Cu through a TiN diffusion barrier of different microstructures such as polycrystalline, nanocrystalline and single crystal quality. The diffusion test performed at 500°C for 30 minutes showed that polycrystalline samples have the maximum diffusion of Cu in TiN films compared with single crystalline and nanocrystalline TiN films due to the columnar grains proving a direct diffusion path. The few low angle grain boundaries present in the highly textured single crystalline TiN films sample also provided a direct diffusion path between the grain boundaries. This also allowed some diffusion of Cu. Nanocrystalline TiN films showed the least diffusion but overall their diffusion distance is greater than 20 nm [26].

1.4.1 Cu Diffusion in TiN

Cu diffusion through TiN diffusion barriers has been mainly reported to be a grain boundary diffusion mechanism. The diffusivity of Cu in polycrystalline TiN films by grain boundary diffusion has been measured and reported by several groups. For example, one of the first studies of the diffusion mechanism of Cu in polycrystalline TiN by Chamberlain et al. [27], is by thermal annealing at temperatures between 600 - 700°C. Nevertheless, the reported values are too different from those expected and are not even comparable to that of Al diffusing in TiN, Table 1.2. The uncertainty of the reported data may have been affected by the oxidized grain boundaries. Other studies also show that polycrystalline TiN thin films allow Cu diffusion through grain boundaries and report values more reasonable with respect to the values of diffusion in crystal structures. The thermal annealing studies for these results are conducted between 400 and 900°C. Table 1.2 shows the diffusion impurity (Al, Cu), the main mechanism of diffusion, diffusion coefficient, activation energy, temperature of study, and the TiN thin film quality.

Table 1.2. Diffusion properties of Cu in TiN layer at temperatures ranging from 300 to 900°C.

Impurity	**TiN**	**Mechanism**	**D_o (cm^2s^{-1})**	**Q (eV)**	**Temperature (°C)**
Al	Polycrystalline	Grain Boundary	$3x10^{-14}$	0.3	300-550 [28]
Cu	Polycrystalline	Grain boundary	$9x10^{7}$	4.43	608-700 [27]
Cu	Nanocrystalline	Grain boundary	$6x10^{-11}$	0.29	400-650 [29]
Cu	Polycrystalline	Grain boundaries	$1.2x10^{-9}$	1.4	600-800 [30]
Cu	Polycrystalline	Lattice diffusion	$2.1x10^{-3}$	2.7	800-900 [30]

1.5 Tantalum Nitride and Tantalum Diffusion Barriers

Tantalum nitride (TaN_x) has a variety of different phases, as will be shown in the next chapter, with all sharing similar characteristics like very high melting point and elevated heat of formation. The stoichiometric TaN phase exhibits a melting point T_m=3093°C, and a heat of formation ΔH_f (298 K) = -252.3 kJ/mol, which demonstrates excellent structural strength at elevated temperatures. As with tantalum, all tantalum nitrides are more stable thermodynamically than Cu, as demonstrated by the absence of Cu-Ta and Cu-N compounds. Moreover the TaN_x/Si interface is more stable than its counterpart Ta/Si, based on the higher activation energy needed for silicide formation in the case of tantalum nitride. This property is attributed to the increased thermal energy required to ensure the dissociation of Ta-N bonds prior to the formation of Ta-Si bonds [31]. From a structural perspective, all TaN_x phases can be simply described as close-packed arrangements of Ta atoms, with the smaller N atoms inserted into interstitial sites. Therefore the resulting structure has significantly higher resistance to copper diffusion than does the pure metal.

Experimental results suggest that the diffusion barrier effectiveness of tantalum-based barriers increases with higher nitrogen content, at least up to a Ta to N ratio of 1:1. This trend is documented and shown in Figure 1.2, which plots barrier failure temperatures for 50 nm thick Ta, Ta_2N, and TaN films, as shown by sheet resistance measurements, XRD, and Secco etch pit observations by SEM [20]. The effectiveness of these tantalum-based barriers is also supported by the electrical diffusion barrier study of Wang et al. [32], which indicates a better diffusion barrier performance for TaN_x relative to its pure metal analog. Various studies agree with the stoichiometry dependence of the barrier failure mechanism [33, 34]. It is demonstrated that stoichiometric TaN fails through Cu diffusion along grain boundaries, but at a higher temperature than Ta. Amorphous Ta_2N, on the other hand, fails through the occurrence of thermally induced recrystallization, forming grain boundaries that act as Cu diffusion paths [33, 35].

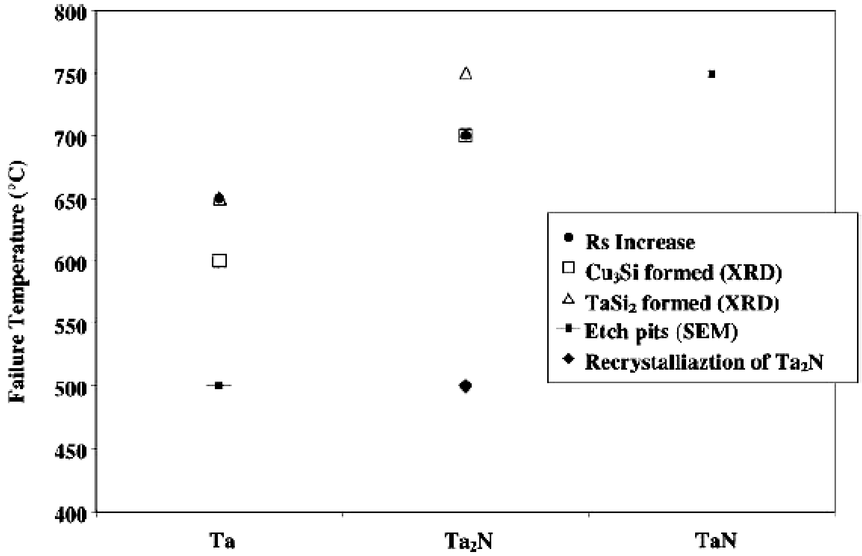

Figure 1.2. Plot of barrier failure temperatures for 50 nm thick Ta, Ta_2N, and TaN films, as examined by sheet-resistance measurements, XRD, and Secco etch pit observations by SEM [20].

Most of the TaN_x materials investigated for diffusion barriers are grown by physical vapor deposition (PVD) techniques. However, significant activities have focused on the development and testing of chemical vapor deposition (CVD) deposited TaN_x barriers, employing both metal-organic and inorganic Ta sources. As mentioned above, this interest was driven primarily by the inherent ability of CVD to provide conformal coatings needed by the more aggressive topographies of submicron devices. For low-temperature MOCVD TaN_x, various investigators examined the applicability of source precursors of the type pentakis dimethyl-amidotantalum (PDMAT) and pentakis diethyl-amidotantalum (PDEAT). However, significant C contamination, prohibitively high resistivity (>1000 μΩ-cm), and poor diffusion barrier performance were observed in films deposited below 450°C. For all MOCVD grown films, low density and large crystallites were determined to be the cause of premature barrier failure. The composition and mediocre barrier performance of MOCVD-grown TaN_x films generated serious concerns regarding their usefulness in advanced copper metallization technologies [36].

As a result, inorganic low temperature CVD Ta and TaN processes were also pursued by using primarily the halide source precursors TaF_5, $TaCl_5$, and $TaBr_5$. A thermal CVD (TCVD) process that employed the reaction of $TaBr_5$ and ammonia at temperatures below 450°C, produced the amorphous nitrogen-rich phase TaN_x, where $x=1.83$. Bromine incorporation was less than 0.5 at%. Resistivity was around 2,500 μΩ-cm for 50 nm thick films and step coverage was good [37, 38]. The most successful results were obtained by Chen et al. who used plasma-assisted CVD (PACVD) to grow a low resistivity, cubic TaN phase. TaN films were produced in a low density plasma using $TaBr_5$, H_2, and N_2 as co-reactants. The films were reported to be stoichiometric, and carbon and oxygen free. They had a bromine concentration below 3 at%, and exhibited resistivities as low as 150 μΩ-cm. Additional thermal stress studies showed that diffusion barrier performance was proportional to film thickness, as shown in Figure 1.3. In particular, a 3 nm thick PACVD TaN_x film provided a barrier to Cu diffusion up to 550°C, as measured by RBS, sheet resistance, and Secco etch pit observation with SEM [39].

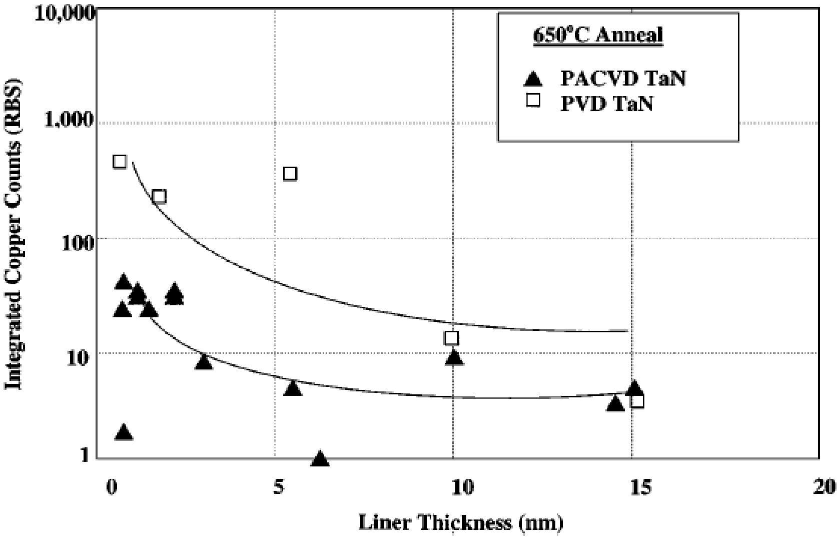

Figure 1.3. Thermal stress of ultrathin (1 - 15 nm thick) PACVD and PCD TaN_x films show that diffusion barrier performance is proportional to the film thickness. The PACVD films were grown by the plasma reaction of tantalum pentabromide, nitrogen, and hydrogen [4].

1.5.1 Cu Diffusion in TaN

Various experimental methods used to determine the thermal stability of thin layers of TaN against Cu diffusion have been reported in the literature. These methods include secondary ion mass spectrometry (SIMS), transmission electron microscopy associated with energy dispersive X-ray spectrometry (TEM/EDS), Rutherford backscattering spectrometry (RBS), sheet resistance measurements and X-ray diffraction (XRD). The calculated Cu diffusion coefficients are obtained from onset times of Cu silicide formation for TaN. The diffusion coefficient of Cu through TaN thin films is generally calculated from Fick's 1st and 2nd laws. When the diffusion mechanism is governed by Fick's laws, the diffusion length (L) of the atoms is approximated by $L = 2(Dt)^{1/2}$, where D is the diffusivity of the atoms and t is the diffusion time. With the above experimental diffusion length (L) values and the time t, the calculation of the D value of Cu in the barrier layer is straightforward. The most important results and findings for diffusion coefficients of Cu through TaN barriers, D, are listed in Table 1.3. The values of the Cu diffusion coefficient have a significant dispersion which may be due to variations in the experimental procedure used by the authors. Oku et al. [40] calculated the Cu diffusion coefficients from onset times for Cu silicide formation determined from XRD after annealing in a 5% H_2/N_2 mixture atmosphere. Jiang et al. [41] studied the TaN barrier thermal stability after annealing at 903 K for 60 minutes in an inert N_2 atmosphere. They observed the formation of Cu silicide at the TaN/Si interface and calculated the Cu diffusion coefficient using the Cu concentration profiles from the surface to the Si substrate, determined by EDS. On the other hand, Loh et al. [42] and Wang et al. [17], calculated the Cu diffusivity from the Cu penetration depth after annealing, before any TaN/Si interfacial reaction has been observed. Samples were annealed for 30 minutes in a standard furnace where the atmosphere is not reported [42] or in 3×10^{-6} Pa vacuum [17], and investigated by using SIMS [42] or high resolution transmission electron microscopy [17], respectively. Some of these authors [17, 40, 41] found that the diffusion coefficients of Cu through TaN layers in the 873–973 K temperature range are smaller than in the work by Nazon et al. [43]. The dispersion of the results may be attributed to the TaN layer microstructure, which governs the diffusion mechanisms. The actual microstructure, which is not always reported in the literature, is greatly dependent on the process parameters. Moreover, impurities (especially oxygen) can have a strong effect on the kinetics.

Table 1.3. Diffusion coefficients and activation energies of Cu in TaN layer at temperatures ranging from 300 to 700°C.

Impurity	**TaN**	**Mechanism**	**D_o (cm^2s^{-1})**	**Q (eV)**	**Temperature (°C)**
Cu	Polycrystalline	Grain Boundary	$2.4x10^{-14}$	0.14	300-550 [42]
Cu	Polycrystalline	Grain boundary	$2.8x10^{-10}$	1.3	600-700 [40]
Cu	Nanocrystalline	Grain boundary	$1.6x10^{-16}$		600-700 [41]
Cu	Polycrystalline	Grain boundary	$1.7x10^{-6}$	1.4	500-700 [43]
Cu	Single crystal	Bulk diffusion	160±9.5	3.27	600-700 [17]

1.6 Applications of Transition Metal Nitride Thin Films in Microelectronics

Transition metal nitrides such as TiN, TaN and HfN have many electrical properties in common with their silicides, which are already used extensively in the IC industry. Transition metal nitrides have been recently introduced in state of the art microelectronic devices. A quick comparison is made in Table 1.4 for the materials of interest TiN, TaN and HfN. Table 1.4 clearly shows that the melting point (T_m) and the heat of formation of the transition metal nitrides is higher that of the silicides, whereas the electrical resistivity, and the Schottky barrier height are comparable. The superior thermal stability of the metal nitrides makes them a good choice for applications in microelectronics.

Table 1.4. Electrical and structural properties of selected transition metal nitrides and their correspond silicide [44].

	TiN	**$TiSi_2$**	**HfN**	**HfSi**	**TaN**	**$TaSi_2$**
Structure	fcc	Orthor.	fcc	Orthor.	Hex.	Hex.
Melting Point (T_m)	2950	1500	3330	-	2950	2200
H (kcal/mol)	-80.4	-32.1	-88.2	-	-60.3	-28.5
Resistivity (μΩ-cm)	20±10	15-25	33	-	130	10-50
Work function (eV)	0.49	0.60	-	0.53	-	0.59

1.6.1 Diffusion Barriers

The constant progression of microelectronics into submicron dimensions creates a continuous demand for better contact metallurgies. The possibility of materials reactions in multilayer thin film assemblies increases with decreasing geometric dimension, because the proximity of layers of different materials and the structural defects inherent in these layers become important. Barrier layers can be effectively used to reduce or prevent such materials reactions. Metal nitrides have been proved to perform extremely well as barriers layers.

The standard interconnect material for semiconductor devices is copper. Barrier layers are used to prevent the interdiffusion of copper and silicon during the processing stage such as contact sintering, passivation or packaging of the device.

The performance of TiN, TaN and HfN as diffusion barriers in copper metallizations has been investigated in detail in this thesis. It was found that these transition metal nitrides provide very efficient barrier layers in contact structures with copper interconnect metallization. The barriers under thermal test show good barrier capability of up to 500°C. The exceptional stability is due to the very low diffusivity of atomic impurities in these materials. The activation energy for copper diffusion in TiN thin films is about 4.4 eV [27]. This value is much higher then the average value of 1 to 2 eV for metals.

1.6.2 Low Barrier Schottky Diodes

A Schottky barrier diode is a majority carrier device which operates under low-level injection conditions. Consequently, the storage time of minority carriers is virtually eliminated and the diode has an inherently fast response. For most metals, the forward voltage drop of the metal-semiconductor junction is lower than that of silicon p-n junction. These favorable features have given the Schottky barrier widespread use in injection logic. High barrier diodes are used as clamps to prevent saturation of the transistor, and low barrier diodes are employed to reduce the output swing of the transistor. A TiN contact made on lightly n-doped silicon forms a Schottky diode with a low barrier of height 0.49 V. This value is close to the barrier height of Ti on n-Si, which is 0.5 V. Because the barrier height is midgap, TiN can also be used to form low barrier voltage ohmic contacts, and a low barrier Schottky diode is advantageous because both device structures could be prepared in one processing step.

1.6.3 MOS Gate Electrode

The most used gate material for MOS transistors is a bilayer structure of polycrystalline silicon and copper, or polycrystalline silicon and a metal silicide. However, the use of a polycrystalline silicon layer has several disadvantages. The most important one is that it has to be doped to a high level in order to keep its electrical resistivity low. The high doping level of the polycrystalline silicon is unfavorable from the device point of view because its low work function yields a high threshold voltage for the MOS transistor. Generally, the threshold voltage has to be lowered by a channel implant. However, a high doping level in the channel reduces the carrier mobility. A channel implant can be omitted if the gate material has a work function which is about midgap. This is the case for transition metal nitrides.

For applications to VLSI, it is desirable that the gate material be thermally stable during annealing in an oxidizing environment. When a polysilicon-refractory metal silicide bilayer film is used as gate material, silicon atoms diffuse through the overlying silicide and react with oxygen to form an oxide layer over the silicide. Once the polysilicon layer is depleted by oxide formation, the silicide is decomposed when the annealing is prolonged. The oxidation mechanism of transition metal nitrides is different because diffusion of silicon atoms through these materials is minimal. It has been found that dry oxidation of TiN transforms the nitride into rutile TiO_2. The oxidation proceeds by diffusion of oxygen through the growing oxide layer. The activation energy for this process can be found from the Arrhenius plot of the diffusivity in Figure 1.4. In the temperature range of 475 to 650°C the activation energy is 2.05 eV for the oxidation of TiN. The temperature at which TiN, TaN and HfN oxidize is much lower that of the transition metals (800-1100°C). On the other hand, the nitrides withstand prolonged heat treatment up to 1000°C if the annealing atmosphere is inert.

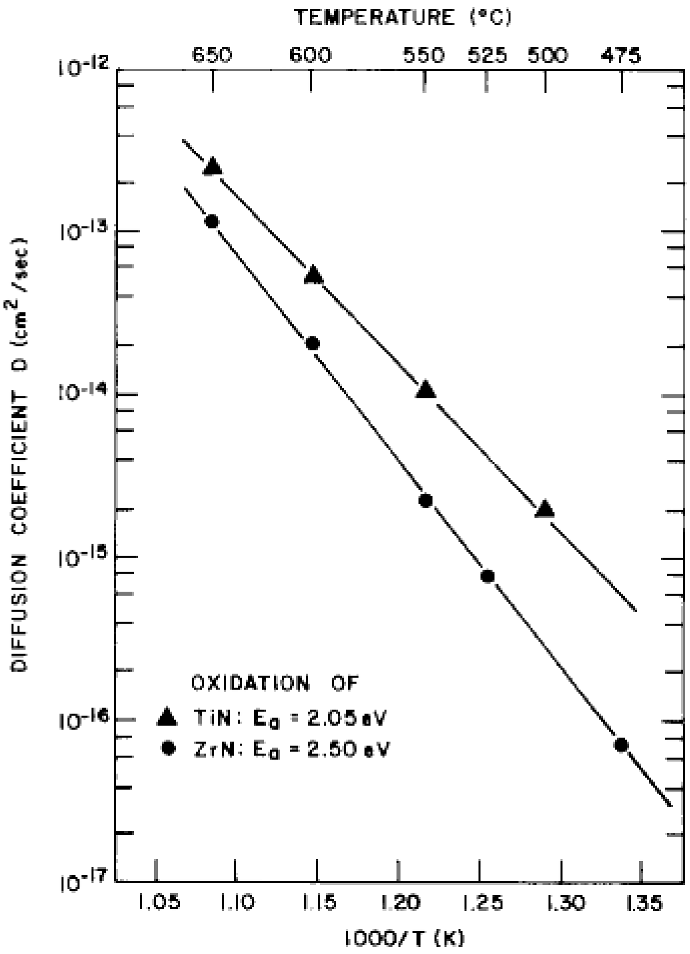

Figure 1.4. Arrhenius plot of the diffusion coefficients for dry oxidation of TiN and ZrN. Both are thermally activated with activation energies of 2.05 eV and 2.5 eV respectively [44].

CHAPTER II

TRANSITION METAL NITRIDES: PROPERTIES AND PROCESSING

2.1 Introduction

Transition metal nitrides, also referred to as refractory materials, have outstanding chemical and physical properties such as high melting point, low resistivity, high thermal conductivity, extreme hardness, and good corrosion resistance. These properties make them important as industrial materials and lead to a significant number of major applications in cutting and grinding tools, wear surfaces, semiconductor devices, as well as other areas.

In this chapter a review of the physical properties of the transition metal nitrides, their classification, and processing techniques are presented. Generally, transition metal nitrides include: TiN, ZrN, HfN, VN, NbN, TaN, CrN, MoN, and WN. The following sections describe their most important properties: electrical, mechanical, structural, and thermodynamic properties.

2.2 General Properties of Transition Metal Nitrides

2.2.1 Structural Properties

Table 2.1. Structural properties of transition metal nitrides including molecular weight, density, crystal structure, lattice parameters and color [1, 2].

Nitride	**Molecular Weight**	**Density (g/cm^3)**	**Crystal Structure**	**Lattice parameters (nm)**			**Color**
				a	**b**	**c**	
TiN	61.91	5.40	fcc (B1-NaCl)	0.424	–	–	Gold
ZrN	105.23	7.32	fcc (B1-NaCl)	0.4567	–	–	Pale yellow
HfN	192.497	13.8	fcc (B1-NaCl)	0.452	–	–	Greenish yellow
VN	64.95	6.8	fcc (B1-NaCl)	0.4126	–	–	Brown
NbN	106.91	7.3	hcp	0.4395	–	0.4338	Dark gray
TaN	194.96	14.3	hcp	0.5191	–	0.2906	Yellowish gray
CrN	66	6.14	fcc (B1-NaCl)	0.4149	–	–	Black
Mo_2N	205.89	8.04	fcc (B1-NaCl)	0.4269	–	–	Dark gray

The data from Table 2.1 are for the corresponding bulk material, which may differ from thin films. The corresponding colors for these transition metal nitrides range from gold yellowish tones to dark gray and black. It is interesting to note that most of them present a face center cubic (fcc) crystal structure like that of sodium chloride (B1-NaCl) which is shown in Figure 2.1. On the other hand, TaN and NbN have a hexagonal crystal structure for their stable phase. The details of the structural properties of TiN, TaN and HfN are presented in the following sections.

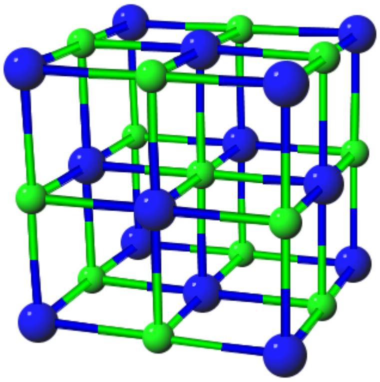

Figure 2.1. Unit cell of the face centered cubic crystal structure (B1-NaCl).

In the B1-NaCl crystal structure, the (100) and (110) surfaces have equal concentrations of metal and nonmetal atoms in every layer at the stoichiometric composition of 1:1. The (111) surfaces, however, are composed of alternating planes of metal and nonmetal atoms, resulting in polar surfaces which are metal-terminated. The (111) surfaces have been found to be the most reactive ones while the (100) surfaces has been found to be the most inert ones. The common method for preparing clean and well ordered surfaces of these materials is repeated high temperature annealing cycles; sometimes these are combined with a short initial sputter-clean cycle. However, this method does not work for the reactive (111) and (110) surfaces. Most of experimental information to date has been collected for (100) surfaces [45].

2.2.2 Thermal and Thermodynamics Properties

The thermal and thermodynamic properties of transition metal nitrides are listed in Table 2.2. Interestingly, these materials have very high melting points, which make them ideal for hard coatings. TiN, TaN, HfN, and ZrN stand out on this list because they all have melting points over 3200 K, which make them good candidates for high temperature resistant coatings and diffusion barrier materials for copper interconnects in the semiconductor industry. As shown in Table 2.2, transition metal nitrides can be considered good thermal conductors, reflecting the metallic characteristics of these materials. However, their thermal conductivity is still considerably lower than the best conductors such as aluminum nitride (220 W/m-K). Their thermal conductivity generally increases slightly with increasing temperature. The thermal expansion is essentially linear with increasing temperature as shown in Figure 2.2 [1, 44].

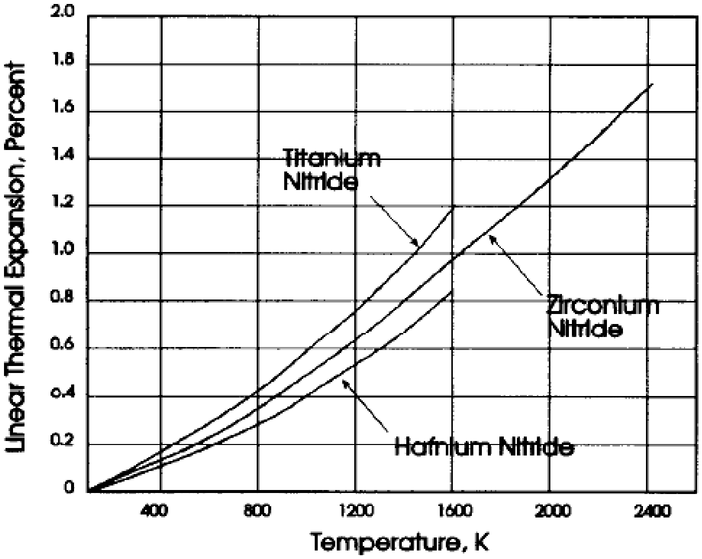

Figure 2.2. Linear thermal expansion of transition metal nitrides vs. temperature [1].

Table 2.2. Thermal and thermodynamic properties of transition metal nitrides: melting point, thermal expansion coefficient, thermal conductivity, heat of formation, gibbs free energy and entropy [1, 44].

Nitride	**Melting Point (K)**	**Specific Heat at 298K (J/mole·K)**	**Thermal expansion at 20°C (x10^{-6}/°C)**	**Thermal Conductivity at 20°C (W/m·K)**	**Heat of formation at 298K -ΔH_f (kJ/mol)**	**Gibbs free energy formation at 298K -ΔG_f (kJ/mol)**	**Entropy at 298K S (J/mol·K)**
TiN	3223	33.74	9.35	19.2	337.7	308.9	30.2
ZrN	3253	40.39	7.24	20.5	365.3	337.0	38.9
HfN	3660	38.01	6.9	21.7	373.6	345.5	44.8
VN	2450	38.00	8.7	11.29	217.2	191.1	37.3
NbN	2673	39.01	10.1	3.76	220.3	194.8	35.3
TaN	3366	40.60	8.0	8.78	252.3	223.9	41.8
CrN	1773				117.2	92.8	37.7
Mo_2N	1173						

2.2.3 Mechanical Properties

Table 2.3. Mechanical properties of transition metal nitrides: hardness, Young's modulus, bend strength, compressive strength, and tensile strength [1, 44].

Nitride	**Vickers Hardness (GPa)**	**Young Modulus (GPa)**	**Bend Strength (MPa)**	**Compressive Strength (MPa)**	**Tensile Strength (MPa)**
TiN	18-21	251	260	1298	37
ZrN	15.8	397	190		35
HfN	16.3	480			
VN	14.2	357			
NbN	13.3	493			28
TaN	14.4	576			
CrN	10.8	320			
Mo_2N	6.3				

Some mechanical properties of these transition metal nitrides are missing in Table 2.3; the main reason for the missing properties is because of the difficulty in measuring such properties. Nevertheless, most transition metal nitrides have very high hardness, high Young's modulus and are the materials of choice for hard coatings. Observations have been made of the failure mechanism, ductile-brittle transition, and hardness of the transition metal nitrides. These materials have a ductile-brittle transition temperature at approximately 800°C. The values reported in Table 2.3 are averages reported in recent reports. The hardness values shown in Table 2.3 are somewhat lower than that of the corresponding carbides. The Group IV transition metal nitrides (TiN, ZrN, and HfN) generally have higher hardnesses than those of Groups V (VN, NbN, and TaN). This reflects a greater contribution of the M-N bonding found in these Group IV compounds. The hardness varies with the film stoichiometry. For the transition metal nitrides TiN, ZrN, and presumably HfN, the hardness reaches a maximum at stoichiometric composition while the maximum hardness of Group V metal nitrides NbN, TaN, and presumably VN occurs before stoichiometric composition is reached. The hardness also varies with the crystal orientation, the (111) orientation being the hardest. Extremely high hardness, up to 50 GPa, has been reported for epitaxial superlattices of metal nitrides such as NbN/TiN and VN/TiN [1, 14, 44].

2.2.4 Electrical and Magnetic Properties

As shown in Table 2.4, the interstitial nitrides are good electrical conductors. They do have a resistivity slightly higher than that of their respective parent metals, but the resistivity still reflects the essentially metallic characteristics of the compounds. The electrical resistivity of TiN (and presumably of other interstitial nitrides) increases almost linearly with temperature. Table 2.4 presents the electrical and magnetic properties of the transition metal nitrides, in most cases for the bulk material. The listed resistivity values include more defects such as grain boundaries, dislocations, stacking faults, and point defects than for an epitaxial or nanocrystalline thin film. More defects in the material increases the resistivity. Table 2.4 shows that the resistivity of TaN is very high compared to that of TiN and HfN. The high resistivity of TaN corresponds to its stable hexagonal phase; research on TaN has shown that cubic metastable TaN exhibits lower resistivity and good diffusion barrier properties [16-18]. An extensive discussion of these properties for TiN, TaN and HfN will be presented in the following sections.

Table 2.4. Electrical and magnetic properties of transition metal nitrides: resistivity, Seebeck coefficient, Hall coefficient, work function and magnetic susceptibility [1, 14, 44].

Nitride	**Resistivity (μΩ-cm)**	**Seebeck coefficient (μV/K)**	**Hall coefficient R_Hx10^{10} (m^3/K)**	**Work function Φ (eV)**	**Magnetic susceptibility (10^{-6} emu/mol)**
TiN	20±10	-7.7	-0.55	4.09	+38
ZrN	7-21	-5.9	-1.44	3.97	+22
HfN	33	-2.9	-4.0	4.27	
VN	85	-5.0	-1.44		+130
NbN	58	-1.5	0.52	3.92	+31
TaN	135	-1.0	-0.53		+25
CrN	640	-92±4	-264		+16
Mo_2N	19.8	2.18±0.5	2.83		

The Hall coefficients are obtained by measuring the transverse electrical potential in samples made to carry current in a magnetic field. The coefficient gives a measure of the carrier concentration; the larger the carrier concentration, the smaller the coefficient. The sign of the coefficient indicates the sign of the charge, negative for electrons, positive for holes [14].

2.3 Composition and Structures of TiN, TaN and HfN

2.3.1 TiN

The phase diagram of Ti-N is not completely clear. The known intermediate phases are the cubic TiN (B1-NaCl) and the tetragonal ε-Ti_2N, the phase diagram is shown in Figure 2.4. The cubic TiN (B1-NaCl) phase has a broad composition range from $TiN_{0.38}$ [46] to $TiN_{1.18;}$ this upper limit is a results of vacancies in both the Ti and N lattices [47]. The lattice parameter of the cubic TiN_{1-x} (B1-NaCl) has a maximum at the stoichiometric composition and decreases rapidly at other stoichiometric ratios. The maximum value of the lattice parameter for TiN (B1-NaCl) is 0.4240 nm, [1] (see Figure 2.3). The tetragonal phase ε- Ti_2N lattice parameters are, a = 0.4945 nm and c = 0.3034 nm. Density studies in conjunction with lattice parameter studies show that at substoichiometric compositions ($N/Ti < 1$), the N lattice is predominantly defective, and at hyperstoichiometric compositions, the Ti lattice is defective ($N/Ti > 1$) [48].

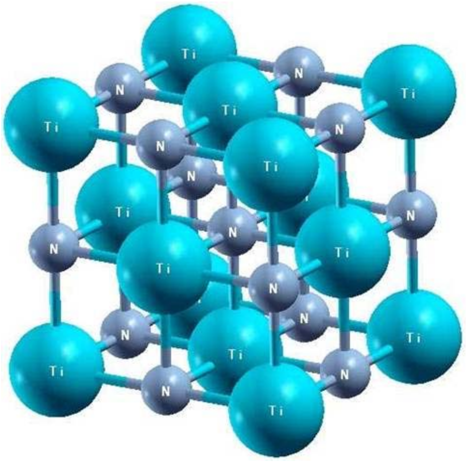

Figure 2.3. Schematic of the cubic crystal structure of TiN (B1-NaCl), lattice parameter a = 0.424 nm.

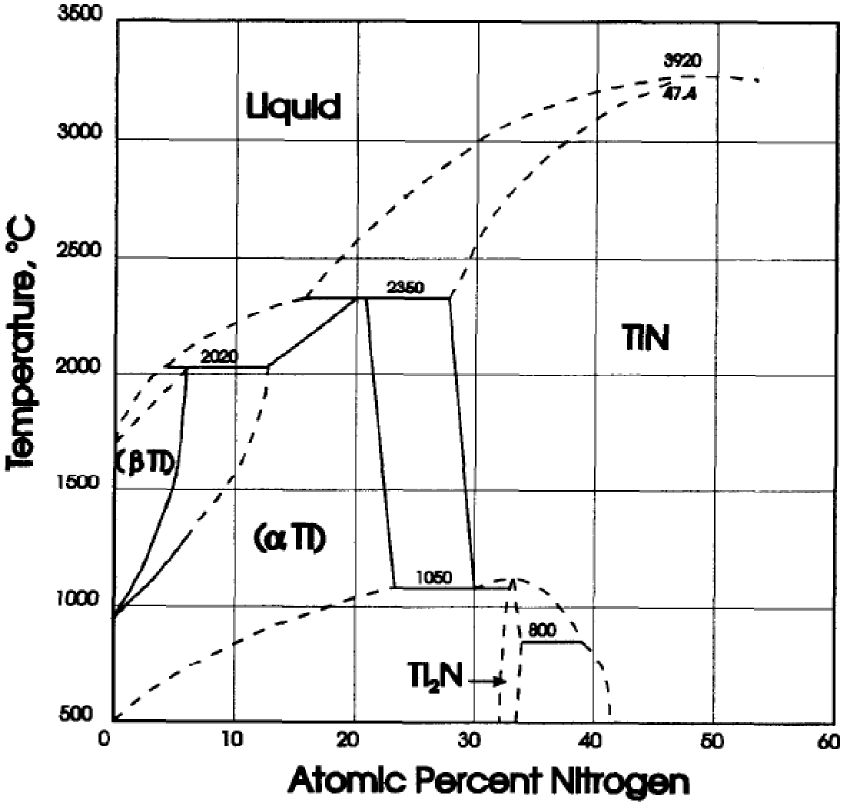

Figure 2.4. Phase diagram of the Titanium-Nitrogen system [1].

2.3.2 TaN

TaN has a variety of compositions and crystalline phases. The two naturally occurring crystalline phases correspond to the hexagonal structures Ta_2N (hcp) and ε-TaN (B35 type structure). The phase diagram of these stable hexagonal phases Ta_2N and ε-TaN is shown in Figure on page 39. Additionally, other crystal phases have been identified such as: tetragonal phases (Ta_3N_5 and Ta_4N_5), hexagonal phases (Ta_5N_6 and δ-TaN), body centered cubic ($TaN_{\sim 0.005}$), [49] and face centered cubic TaN (B1-NaCl) [1, 50]. The information about the crystal structures of the 8 phases of TaN is listed in Table 2.5. Among them, the stable hexagonal ε-TaN (B35) and the metastable cubic TaN (B1-NaCl) are the most important ones and will be further discussed as follows.

Table 2.5. The 8 different TaN phases, their stoichiometric composition, phase, crystal structure and lattice parameters [1, 49, 50].

Composition	Phase	Crystal structure	Lattice parameters	
			a (nm)	c (nm)
$TaN_{0.05}$	β phase	BCC	0.337	_
Ta_2N	γ phase	HCP	0.305	0.492
TaN		FCC	0.433	_
δ-TaN	δ phase	Hexagonal	0.293	0.286
ε-TaN	ε phase	Hexagonal (B35)	0.518	0.290
Ta_5N_6		Hexagonal	0.517	1.030
Ta_4N_5		Tetragonal	0.683	0.427
Ta_3N_5		Tetragonal	1.022	0.387

The stable hexagonal ε-TaN (B35) crystal structure is shown in Figure 2.5. The structure of the hexagonal ε-TaN (B35) phase belongs to the space group P_6/mmm (#191), with lattice parameters a = 0.518 nm, c = 0.290, c/a = 0.560. Detailed information about the atomic distribution in lattice cell is described in terms of the primitive vectors and atomic position:

Primitive Vectors:

A_1 = $\frac{1}{2}$ a X - $\frac{1}{2}$ $3^{1/2}$ a Y

A_2 = $\frac{1}{2}$ a X + $\frac{1}{2}$ $3^{1/2}$ a Y

A_3 = c Z

Atomic Position:

B_1 = 0 = 0, 0, 0 (Ta)

B_2 = 1/3 A_1 + 2/3 A_2 + $\frac{1}{2}$ A_3 = 1/3, 2/3, 1/2 (Ta)

B_3 = 2/3 A_1 + 1/3 A_2 + $\frac{1}{2}$ A_3 = 2/3, 1/3, 1/2 (Ta)

B_4 = $\frac{1}{2}$ A_1 = 1/2, 0, 0 (N)

B_5 = $\frac{1}{2}$ A2 = 0, 1/2, 0 (N)

B_6 = $\frac{1}{2}$ A_1 + $\frac{1}{2}$ A_2 = 1/2, 1/2, 0 (N)

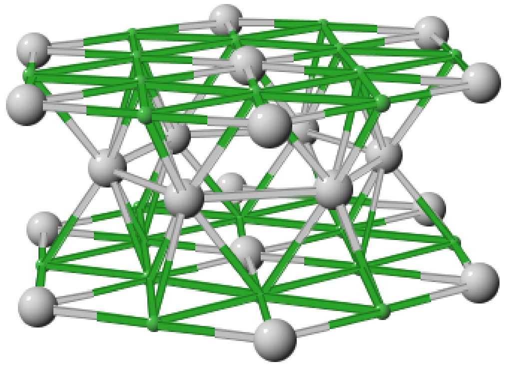

Figure 2.5. Schematic of the crystal structure of the hexagonal stable ε-TaN (B35), Ta atoms are represented by big spheres and N by the small ones.

The crystal structure of metastable cubic TaN is shown in Figure 2.6; this is similar to the NaCl face centered cubic structure which is similar to the TiN presented previously. The lattice parameter for the cubic TaN (B1-NaCl) crystal structure is a = 0.433 nm.

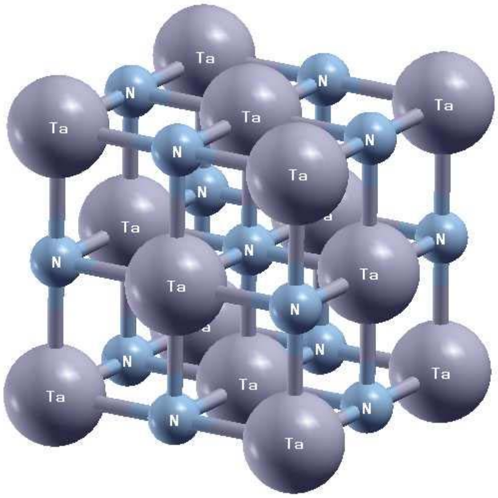

Figure 2.6. Schematic of the metastable cubic TaN (B1-NaCl) crystal structure, lattice parameter a = 0.433 nm.

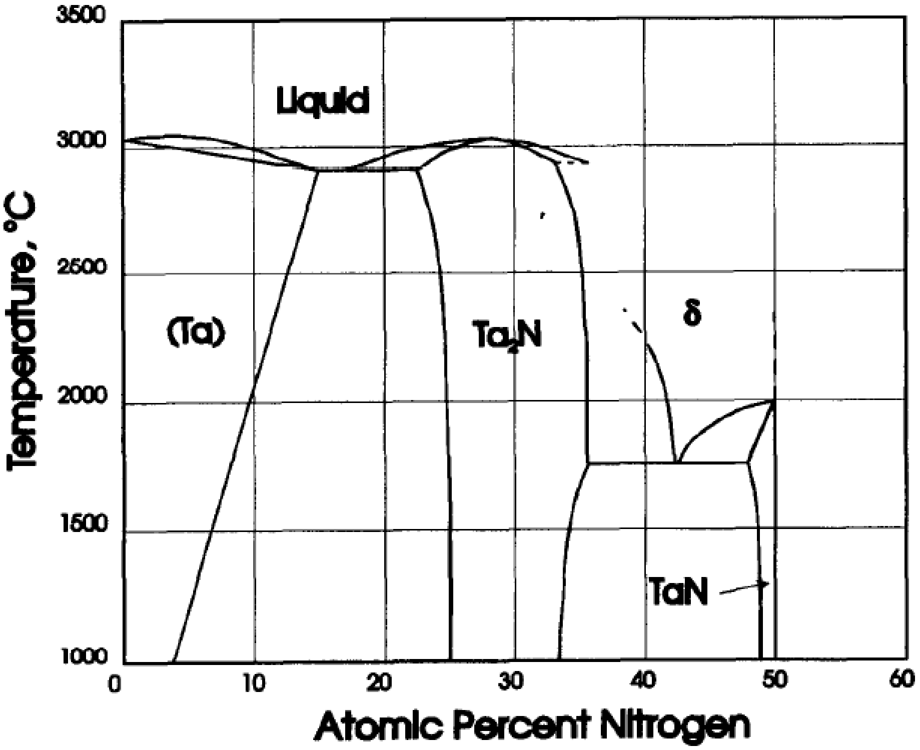

Figure 2.7. Phase diagram of the Tantalum-Nitrogen system [1].

TaN powder can be produced by nitridation of the Ta metal with nitrogen or ammonia at 1200°C. Then, sintering of the powder at 1300°C to 1400°C produces the bulk hexagonal ε-TaN (B35).

2.3.3 HfN

The phase diagram of Hf-N is not completely known (Figure 2.9). The most observed intermediate phase is the cubic HfN (B1-NaCl). The cubic HfN (B1-NaCl) has a broad composition range, which extends from $HfN_{0.74}$ to an upper phase limit of $HN_{1.13}$. The crystal structure of the stoichiometric cubic HfN (B1-NaCl) is shown in

Figure 2.8, with a corresponding lattice parameter of a = 0.452 nm. The decrease of the lattice parameter with the composition indicates that the Hf lattice points are defective when the N/Hf ratio is greater than one [48]. It is worth noting that the physical properties of HfN vary significantly as the stoichiometry of HfN changes. For example, the reported resistivity of stoichiometric HfN (1:1 ratio) thin films growth on silicon substrates is greater than 100 μΩ-cm, while a non-stoichiometric HfN_x ($x>1$) could be an insulator [51] or semiconductor [52-54]. HfN powder is produced by nitridation of the Hf metal with nitrogen or ammonia at 1200°C.

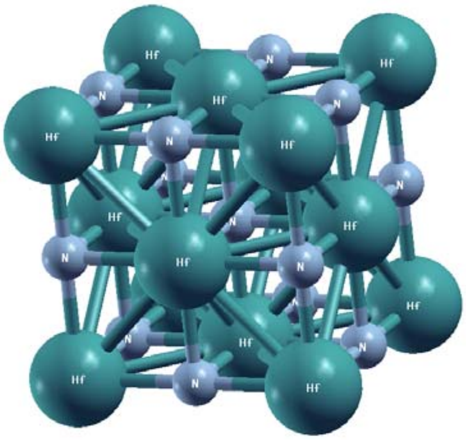

Figure 2.8. Schematic of the stable cubic crystal structure HfN (B1-NaCl), lattice parameter a = 0.452 nm.

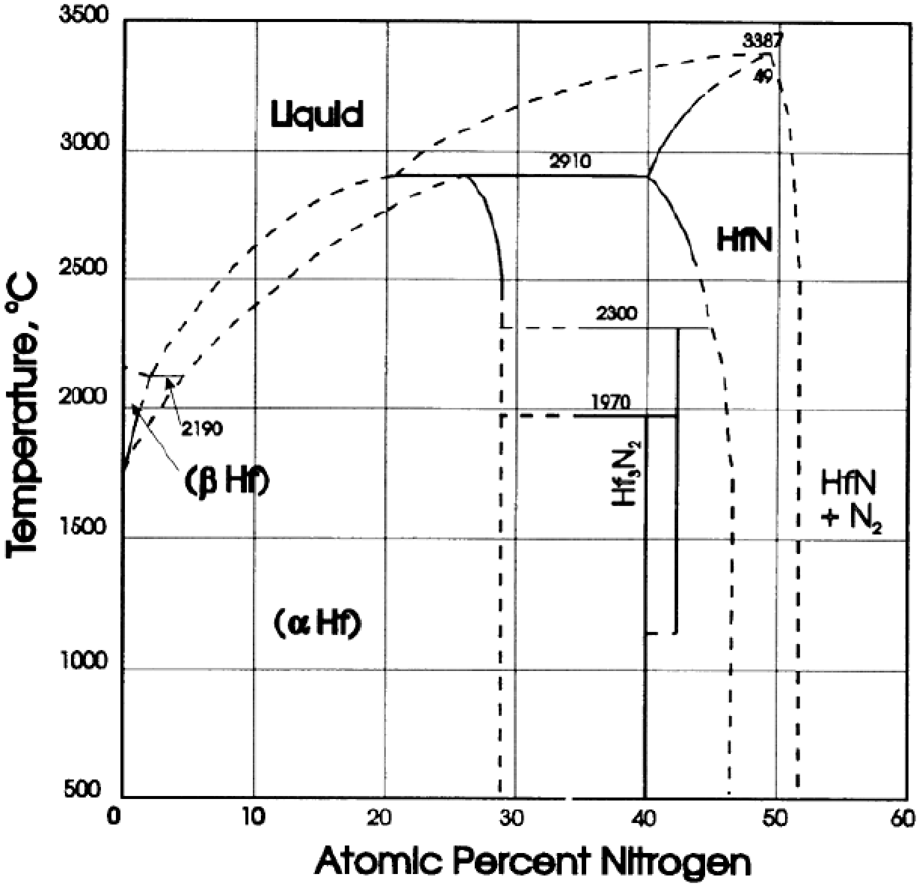

Figure 2.9. Phase diagram of the Hafnium-Nitrogen system [1].

2.4 Nitride Formation, Electronegativity, Atomic Radius and Bonding

The factors that play an important role in the formation of transition metal nitrides are the difference in electronegativity between nitrogen and the other element forming the nitride, the size of the atoms, and the electronic bonding characteristics of these atoms.

2.4.1 Electronegativity

Electronegativity can be roughly defined as the tendency of an element to gain electrons and form negative ions. Table 2.6 shows the electronegativity of the transition metals and nitrogen, as well as their electronegativity difference. The electronegativity is calculated by Pauling and others [1, 2]. It should be noted that the electronegativity of an element is not a fixed value, and is dependent on its valence state. In Table 2.6, nitrogen has a higher electronegativity than any other element on the left. The difference in electronegativity between nitrogen and the other element forming a nitride is an important factor in the structure and electronic bonding of the transition nitrides that determines the nature of the compound.

The electronegativity of nitrogen is high while that of the transition metals is low (Table 2.6), resulting in ionic bonding because of the transfer of electrons from one atom to the other resulting in an electrostatic interaction. A qualitative relationship between the difference in electronegativity and the ionic character of the bond is well recognized; the greater the difference, the greater the ionicity. In the case of TiN, the ionic bonding of TiN indicates a charge transfer from the titanium atom to the nitrogen atom, resulting in the formation of Ti^+ and N^- ions and, correspondingly, an electrostatic interaction. The ionic bonding is similar for the other nitrides of group IV (Zr and Hf) and lower for those of group V (Ta, V, Nb). Generally, in the ionic bonding, it is likely that the M-N bond is predominant due to the octahedral grouping of the metal atoms around the nitrogen atom. This grouping has six bonds to the six corners and, in forming the mononitrides, the valence electrons of the nitrogen atom hybridize with the *p*-state metal atom, with likely d^2sp^3 hybridization, which is common for metals in group IV.

Table 2.6. Electronegativity and electronegativity difference between nitrogen and the transition metal nitrides [1].

Element	**Electronegativity (χ_M)**	**Electronegativity difference (χ_N-χ_M)**
Nitrogen	3.0	-
Titanium	1.5	1.5
Zirconium	1.4	1.6
Hafnium	1.3	1.7
Vanadium	1.6	1.4
Niobium	1.6	1.4
Tantalum	1.5	1.5
Chromium	1.6	1.4
Molybdenum	1.8	1.2

2.4.2 Atomic Radius

The second factor controlling nitride formation is the atomic radius of the constituent elements. The radii of the elements of interest are listed in Table 2.7. It is important to be cautious when considering the radius of an element since the size of an atom is related to a wave function and it follows that no atom has a precise radius. The values presented in Table 2.7 are assumptions but they form an empirically useful set of values. Additionally, the radius of an atom may change depending on the hybridization.

It is interesting to note that nitrogen is one of the smallest atoms, and it is smaller than carbon. Table 2.7 also shows the type of nitride formed, i.e., interstitial (IS), covalent (C), or intermediate (IM). The transition metals of interest to us have a host lattice that is large enough for the nitrogen atom to fit in readily and thus form stable interstitial compounds.

Table 2.7. Approximate atomic radius of transition metals, nitrogen, and selected elements for reference [1].

Element	**Atomic Number**	**Atomic Radius (nm)**	**Type of Nitride**
Carbon	6	0.078	
Nitrogen	7	0.074	
Oxygen	8	0.066	
Aluminum	13	0.126	C
Silicon	14	0.117	C
Titanium	22	0.1467	IS
Vanadium	23	0.1338	IS
Chromium	24	0.1267	IM
Zirconium	40	0.1597	IS
Niobium	41	0.1456	IS
Molybdenum	42	0.1386	IS
Hafnium	72	0.1585	IS
Tantalum	73	0.1457	IS
Tungsten	74	0.1394	IS

2.4.3 Atomic Bonding

The other important factor governing the structure of nitrides is the nature of the bond between the nitrogen and the other element forming the compound. It is important to note that bonding, electronegativity, and atomic size are all interrelated. A bond, the attractive force that holds atoms or molecules together, is usually characterized by two factors: its length – determined by spectroscopic or diffraction techniques; and its strength - determined from quantitative measurements of the bond formation or dissociation energy. The type of bond is a function of the electronic configuration of the constituent elements, the orbital types, and the bond polarity. Generally, the shorter the bond the stronger the bond. The bonds in nitride compounds can be ionic, metallic, covalent or a combination of them.

The bonding of the transition metal nitrides of interest to us, interstitial nitrides, is not completely understood. Their characteristics and properties indicate that they are more than a simple solution of nitrogen atoms within the lattice of a transition metal. Indeed, the differences between nitrides and host metals are significant and indicate the presence of metal to nitrogen (M-N) bonds with essentially no nitrogen to nitrogen bonds (N-N). The overall bonding scheme is a combination of these three types of bonding:

a. **Ionic Bonding.** Formed by transfer of valence electrons between two different atoms, giving a positive and negative ion, and producing an electrostatic attraction between these ions of opposite charge. A large difference in electronegativity favors ionic bonding. The best known ionic material is sodium chloride (NaCl).

b. **Metallic Bonding.** Here the atoms are considered to be ionized, with the positive ions arranged in the lattice positions. The electrons are delocalized; that is, they are able to move freely throughout the lattice. The bonding occurs by the electrostatic attraction between the electrons and the positive metal ions. Most metals can be considered as close packed arrays of atoms held together by these delocalized electrons.

c. **Covalent Bonding.** The major type between the metal *d*-state and the nitrogen *p*-state with some metal to metal interaction. The nature of a covalent bond is the sharing of electrons, rather than the transfers that takes place in ionic bonds. Typically, two atoms share a pair of electrons.

The electronic configuration of the mononitrides, including band structure, density of states, and other bonding considerations, has been the matter of much research interest and is now relatively well known (as shown in later sections). As an example, Figure 2.10 presents an schematic of the bonding orbitals of TiN on the (100) crystallographic plane which is typical of transition metal nitrides. The nitrogen *p* orbitals and the titanium *d* orbitals form both α and π covalent bonds. The σ bonded overlapping titanium *d* orbitals indicate a certain degree of Ti-Ti interaction.

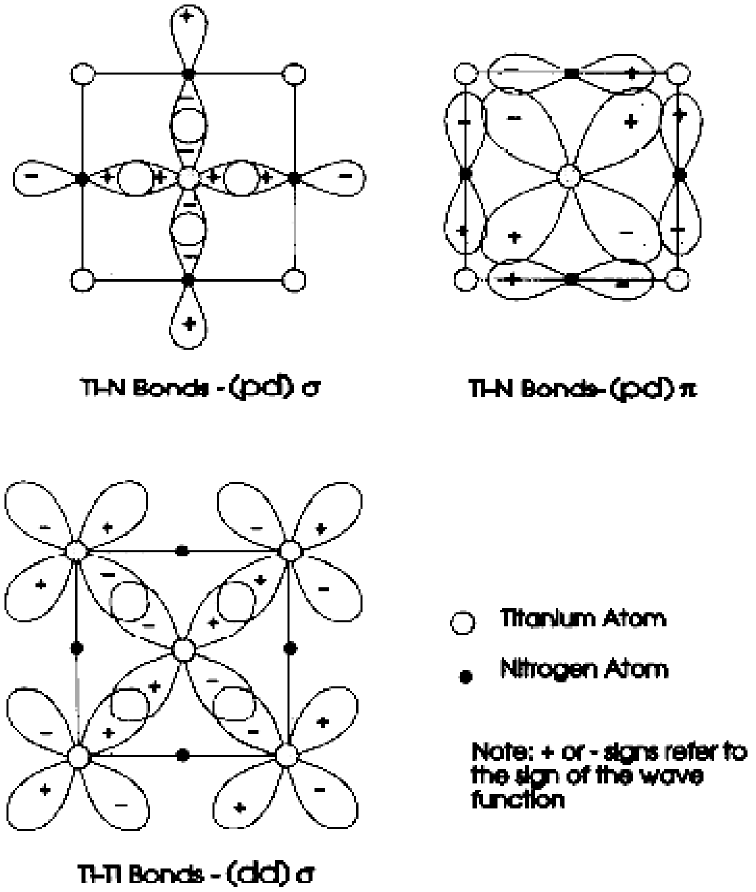

Figure 2.10. Planar view of the (100) plane of the bonding orbitals of TiN [1].

2.5 Properties of TiN, TaN and HfN

2.5.1 Mechanical Properties

Transition metal nitrides are potentially important materials in engineering applications because of their high hardness. Certain commercial applications include cutting tool bits and wear resistant surface finishes; in addition, they have a high potential for a variety of other applications such as electrically conducting diffusion barriers in microelectronic devices and coatings for solar applications. The mechanical characteristics of hard constituents critically influence the performance of composites because they are not only subjected to loads at ambient temperature, but also to loads during temperature cycling. Therefore hardness, Young's modulus, Poisson's ratio, shear, and bulk modulus are very important.

The mechanical properties and the failure mechanisms of transition metal nitrides are reviewed in detail by Toth [48]. Generally, large spreads in the reported values found in the literature are common. This is particularly true for older reports which were mostly performed on sintered materials. More recent testing has been made on single crystals or polycrystalline materials obtained from the melt or by thin-film deposition. These are believed to yield more accurate and consistent information. Yet, any test must be carefully characterized in order to be meaningful. The following factors influence mechanical testing: stoichiometry, impurities (oxygen and nitrogen), grain size, grain orientation, structural defects (vacancies, dislocations), and presence of different phases.

Transition metal nitrides are often processed by sintering with a metal binder such as cobalt or nickel. The mechanical properties of such composites are often quite different from those of single crystal or polycrystalline materials. This adds to the confusion when quoting property values.

2.5.1.1 Hardness

Hardness is a complex property which involves elastic and plastic deformation, crack initiation, and the development of new surfaces. It can be defined in terms of bonding energy, covalence level, atomic spacing, and by the parameters of fracture and deformation characteristics. Hardness is dependent on the fabrication process, composition, and the presence of impurities. To understand hard materials, it is important to know in detail the type of bonding in the material and have a hardness measurement technique that provides consistent and reproducible results.

Materials which exhibit high intrinsic hardness can, in general, be categorized as having high cohesive energy, short bond length, and a high degree of covalent bonding. Covalent bonds are characterized by comparable orbital energies for neighboring atoms, strong overlap between orbitals, and similar orbital sizes. Such bonds are highly directional and can affect the deformation mechanism. As an example, diamond is the hardest material and has pure covalent bonds, while cubic boron nitride, the second hardest material, is predominantly covalent but is thought to have a small ionic contribution. Therefore, it is expected that the intrinsic hardness of a material will be reduced by an amount proportional to the fraction of ionic or metallic bonding present.

The hardness and other mechanical properties of HfN are listed in Table 2.3. The microhardness values reported range from 16.3 GPa (bulk) [1] to 25 GPa. An early measurement of the microhardness of single crystal HfN thin films was reported by Johansson et al. in 1985 to be 34.3 GPa, about twice that of the bulk value [53]. The large difference arises primarily from differences in thin film microstructures, such as grain size, columnar vs. equiaxed structure, void density, and film purity. The hardness was measured by Vickers hardness measurement. The reason for the lower hardness observed in bulk or polycrystalline HfN is intergrain boundary failure, as explained in the paper.

2.5.2 Electrical and Magnetic Properties

Transition metal nitrides have electrical and magnetic properties similar to those of the transition metal elements. Their properties are typically metallic. Electrical and structural properties of some transition metal nitrides and their corresponding silicides and the values of parameters such as electrical resistivity, Hall coefficient, and magnetic susceptibility are comparable to those of the metal transition elements and their alloys. A review of these parameters will be presented later in this chapter, and then several simple correlations with electron concentration are discussed. Nevertheless, the knowledge of electrical and magnetic properties of nitrides is still incomplete. Just a few properties have been carefully measured but most measurements were made in poorly processed samples; therefore, the presence of impurities that can change the stoichiometry of the nitride is critical to the measured values.

2.5.2.1 Resistivity

Most transition metal nitrides are metallic conductors with a room temperature resistivity ρ in the range 7-250 $\mu\Omega$-cm. Resistivity values have been compiled by several authors and are listed in Table 2.4. For example, the value of the resistivity for TiN is of 20 ± 10 $\mu\Omega$-cm; older values are probably not as reliable and therefore not included. The difference in the resistivity value is usually attributed to factors such as:

1) Different non metal to metal composition ratios, i.e. stoichiometric composition.
2) Different concentration of impurities, in this case the other impurity could be interstitial oxygen.
3) Different residual porosity and different empirical formulas for porosity correction.

Deviations from the stoichiometric TiN, TaN and HfN rapidly increase the value of the resistivity to the extent that the materials even become an insulator. As example, the resistivity values recently reported by Langereis et al., shows a wide variety in resistivity values. They used a plasma atomic layer deposition (ALD) technique, to deposit thin films of various composition ratios, N/Ta, on silicon substrates. Table summarizes some of the results for the various TaN_x thin films, their respective resistivity measured by four point probe (FPP), the thickness determined by x-ray reflectivity (XRR) and the N/Ta ratio and impurity concentration from Rutherford backscattering spectrometry (RBS) measurements. It is clearly understood that the N/Ta ratio as well as the concentration of impurities such as oxygen and carbon (residues from the precursor gases) play an important role in the overall properties of the thin film [55].

Table 2.8. Material properties of TaN_x films deposited at various plasma conditions, substrate temperatures, and plasma gas mixtures. In situ spectroscopic ellipsometry (SE), x-ray reflectivity (XRR), Rutherford backscattering spectroscopy (RBS), and four-point probe (FPP) measurements were used to determine the material properties [55].

Composition			**Thickness (nm)**	**Resistivity (μΩ-cm)**
N/Ta ratio	**O (at. %)**	**C (at. %)**		
0.45	7	12	28.1	380
0.55	15	10	30.9	1300
0.76	15	10	26.4	48±10
1.0	15	<2	51.6	1.1×10^4
1.5	8	<2	68.1	$>5 \times 10^4$

2.5.2.2 Hall Coefficients

Hall coefficients yield information about the number of carriers in the conduction band, the band shape as a function of electron concentration, and, when measured in conjunction with the resistivity, the mobility of the carriers. In Table 2.4 the Hall coefficient of some transition metal nitrides is listed; this is sensitivity to impurity contents, N/M ratio composition, and temperature. Over a narrow range of N/M composition the Hall coefficient doesn't vary appreciably at room temperature. A number of researchers have calculated the carrier concentrations by assuming a simple one band model equation,

$$R_0 = \frac{M}{enN_0 \rho_0} \quad \text{...(2.1)}$$

where n is the carrier concentration, M is the formula weight, and ρ_0 is the density. All values of R_0 in Table 2.4 are negative, which means that the dominant carriers in transition metal nitrides are electrons.

2.5.2.3 Magnetic Susceptibilities

The magnetic susceptibilities of several stoichiometric transition metal nitrides are shown in Table 2.4. This susceptibility is strongly dependent on the metal-to-non-metal ratio. Measurements of nearly stoichiometric binary nitrides suggest that the magnetic susceptibility can be correlated with the valence electron concentration and with the concept of band structure. Band structure will be presented in the following sections.

2.5.3 Electronic Properties of Transition Metal Nitrides

The distribution of charges between the atoms in a solid determines the nature of the chemical bond and the corresponding electronic states. The electron states directly involved in the bonding in an ordered solid are described by the band structure, $E(k)$, and are commonly referred to as valence band and conduction band states. The band structure describes the distribution of the electron states in energy and momentum space and provides a means for understanding the electronic properties on a microscopic level.

Band structures calculated by theoretical methods have shown that bonding in transition metal nitrides involves simultaneous contributions from metallic, covalent and ionic bonding. Various aspects of the bonding have been discussed, such as the importance of covalent bonds between transition metals and nonmetals and the ionic contribution in terms of charge transfer between metal and nonmetal atoms [45].

2.5.3.1 Band Structure

Recent reports on the calculations of band structure are based on density functional theory (DFT). Band structure and density of states calculations are based on the FLAPW (full linear augmented plane wave) methods with the LDA (local density approximation) exchange potential. The transition metal nitrides that crystallize in the sodium chloride structure were reviewed fairly recently**.** The band structures of transition metal nitrides are fairly similar. They are all characterized by an energetically low-lying band, which is derived from non metal 2s states, as illustrated in Figure 2.11, for the cubic HfN (B1-NaCl) structure. Separated by an energy gap from the nonmetal 2s band, three overlapping bands are found, which originate from the state at Γ. These bands can be derived from the 2p states of the non metal atom but also contain a significant contribution of states with d-symmetry. The amount of hybridization varies from compound to compound. The next five bands, which originate at Γ around the 0 value predominantly derive from the transition metal d states, but also exhibit some p state character. The highest lying bands represent a mixture of states with different symmetries, originating from both constituents [56].

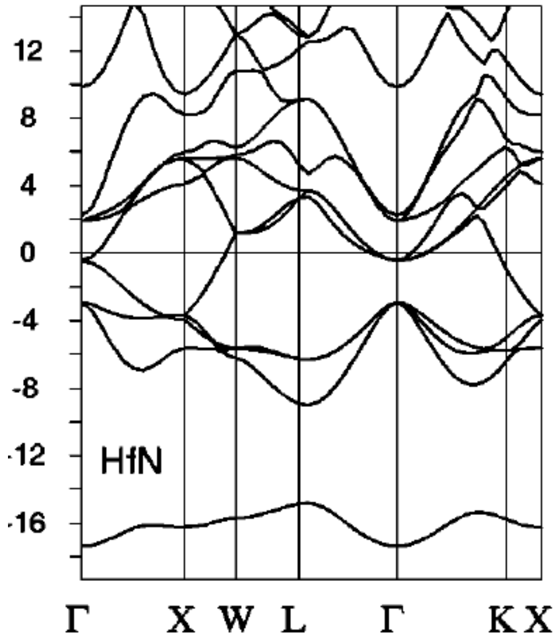

Figure 2.11. Band structure of the cubic HfN (B1-NaCl) crystal structure calculated using FLAPW [56].

2.5.3.2 Bulk Energy Band Mappings

Detailed information about the band structure in solids can be obtained from angle resolved photoemission experiments (ARP) on single crystals [57, 58]. Location and dispersion of the two-dimensional energy bands are usually mapped out by determining the energy positions of features in photoemission spectra. The solid lines in

Figure 2.12 show the calculated band structure of TiN along the <100> direction (Γ-X symmetry). The dotted lines and open dots represent the position of shoulders and peaks in the ARP spectra. This band mapping was derived from non-emission spectra recorded using synchrotron radiation and photon energies from about 15 to 35 eV. Individual bulk bands and their symmetry and dispersions ca n be identified and mapped out by applying the direct transition model [45].

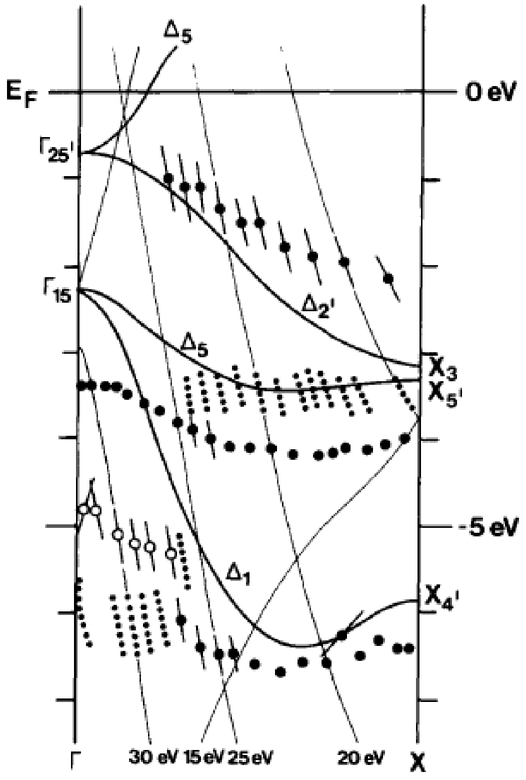

Figure 2.12. Calculated (solid lines) and experimental (solid dots) bulk energy band dispersions along the <100> direction for TiN. The thin solid lines represent the Δ_1 final-state bands displaced downwards by the amounts indicated [45].

2.6 Processing of Transition Metal Nitrides

2.6.1 Bulk Samples

Bulk samples are either prepared from their powders by hot-pressing, hot-isostatic-pressing (hiping) and self-propagating high temperature synthesis (STS) or from compacted materials using diffusion processes. The advantage of preparing samples from their powders is that samples of different composition and porosity can be made in a relatively short time. A minor disadvantage of hot-pressing and hiping is that an inert atmosphere, or for the preparation of the nitrides a nitrogen atmosphere, has to be applied to avoid oxidation. A relatively high temperature (2200-3000 K) and pressure is needed to prepare nearly compact materials by hot-pressing. Therefore, impurities are often included which change the material properties considerably. The STS technique produces materials with high porosity and should not be used in the preparation of nitrides. To obtain non-porous samples, diffusion annealing of transition metals in a nitrogen atmosphere can be used. However, the preparation is time consuming and only small specimens can be produced. Furthermore, the texture and the porosity in the center of the sample caused by the diffusion process must be considered.

2.6.2 Thin Films

2.6.2.1 Physical Vapor Deposition (PVD)

The preparation of thin films by using physical vapor deposition (PVD) is carried out by material transport between the target, which provides the material necessary for the layer preparation, and the substrate. The ejection of the source material is a results of the bombardment of the surface of the target with highly energetic gas ions (e.g. Ar^+), accelerated by high voltage. Atomic particles are expelled as results of the momentum transfer between the ion particles and the target. The ejected particles traverse the vacuum chamber and are subsequently deposited on a substrate as a thin film. During the last few years various techniques of physical vapor deposition methods such as magnetron and reactive sputtering have been developed, where thin film growth can occur at low temperature and pressure. A very versatile technique, which is the main tool for this research and will be described in the next chapter, is pulsed laser deposition (PLD), which can be done for a wide range of different deposition conditions [59]. A brief description of the most popular sputtering techniques follows:

a. **Diode Sputtering.** It is the simplest but requires an electrically conductive target. It has low energy efficiency and electron bombardment can cause significant damage of the substrate.
b. **Radio-Frequency (RF) Sputtering.** By using frequencies above 50 kHz it can sputter insulator materials but the process has low deposition rates.
c. **Triode Sputtering.** Uses an additional cathode to sustain the plasma but is more complicated and may cause contamination of the deposit.
d. **Magnetron Sputtering.** Uses a magnetically enhanced cathode (magnetron). This process has considerably expanded the potential of sputtering. The magnetron sends the electrons into spiral paths to increase collision frequency

and ionization. Deposition rates are high and the process does not cause radiation damage.

2.6.2.2 Chemical Vapor Deposition (CVD)

Chemical vapor deposition (CVD) is a deposition method of forming a desired compound by the nucleation of the compound or compounds from the gaseous phase onto a substrate. The compound bearing the species to be deposited is vaporized (if it is not already a gas), by either a pressure differential or the action of a carrier gas and is transported to the substrate. Generally speaking, the deposition process is either a thermal decomposition or a chemical reduction. Both thermal decomposition as well as chemical reduction involves metal-organic compounds, halides, or other simple inorganic compounds. CVD processes are dependent on the thermodynamics and the kinetics of the reaction. For the growth of CVD films, temperatures are in the region of 1200 – 2500 K. The applications of CVD are mainly in coatings that are not easily applied by PVD techniques. Some of the advantages of CVD are: (1) various kinds of coatings (carbides, nitrides, oxide, etc), (2) the crystal growth is controlled by the setting of the reactive gas concentrations, (3) high deposition rates are possible, (4) the coating is closer to a thermodynamic equilibrium than PVD deposition, and (5) the density is much closer to that of bulk material annealed at high temperature. However, with CVD thin films, there is an interaction between the layer and substrate which superimposes stresses into the hard phases; this influences their properties (hardness, Young's modulus). The disadvantages include: high temperature is needed to obtain certain compounds, low pressure restricts the types of substrate that can be coated, uniform heating of the substrate is quite difficult, and because of the reactor design, the uniform coating of complex sample shapes is difficult [59].

2.6.2.2.1 CVD of Titanium Nitride

CVD of titanium nitride is one of the most important nitride coatings from an application stand point. Titanium nitride can be obtained by reactive sputtering of titanium and CVD with titanium tetrachloride as the metal source and either nitrogen gas or ammonia as a source of nitrogen, as shown in the following equations,

Reaction 1: $TiCl_4 + \frac{1}{2}N_2 + 2H_2 \rightarrow TiN + 4HCl$ .....(2.2)

The range temperature for reaction 1 is 900-1200°C with the best results obtained at 1000°C, when using Argon as the diluent at pressures of up to 1 atm. This reaction is also obtained in high frequency plasma (13.56 MHz) at 150 Pa of pressure and a lower temperature of 500°C.

Reaction 2: $TiCl_4 + NH_3 + 0.5H_2 \rightarrow TiN + 4HCl$ .....(2.3)

This reaction takes place at much lower temperatures, between 480-700°C, and it is usually carried out at a pressure of ~1 kPa with excess hydrogen. The use of ammonia in this reaction generally results in higher deposition rates, which is due to the high reactivity of the monoatomic nitrogen released during the ammonia decomposition.

Reaction 3:

$Ti[N(CH_2CH_3)_2]_4$ + NH_3 → TiN + gaseous organics ....(2.4)

Reaction 4:

$Ti[N(CH_3)_2]_4$ + NH_3 → TiN + gaseous organics ....(2.5)

The availability of two metal-organic titanium compounds, tetrakis-diethylamino titanium (TDEAT) and tetrakis-dimethylamino titanium (TDMAT) makes possible the deposition of TiN at even lower temperatures, with reactions 3 and 4 both taking place at 320°C. These low temperature reactions are being developed for semiconductor applications to replace sputtering. It is important to note that reaction 3 is preferred because fewer impurities are present (such as C and O_2) [1].

2.6.2.2.2 CVD of TaN and HfN

The CVD of transition metal nitrides such as TaN and HfN is still in a development phase. A metal halide, usually a metal chloride, is reacted with nitrogen in an excess of hydrogen at a pressure of about 1 kPa. The typical reactions are:

Reaction 1: $TaCl_5 + \frac{1}{2}N_2 + 2.5H_2 \rightarrow TaN + 5HCl$ .....(2.6)

Tantalum nitride is formed from the reaction between the metal chloride and nitrogen at temperatures between 800-1500°C [15].

Reaction 2: $HfCl_4 + \frac{1}{2}N_2 + 2H_2 \rightarrow HfN + 4HCl$ .....(2.7)

Hafnium nitride (HfN) results from the reaction of hafnium chloride, with nitrogen and hydrogen at 900-1300°C or with ammonia as nitrogen source at 1100°C [1].

An example of how the preparation method affects the properties of the material is shown in Figure 2.13 for TiN. It can be seen that the preparation technique influences the elastic property measured for TiN. Values of Young’s modulus from bulk samples are generally lower than those of thin films samples. This might be due to the influence of the substrate, the interaction between substrate and coating, and the stresses occurring in the coating.

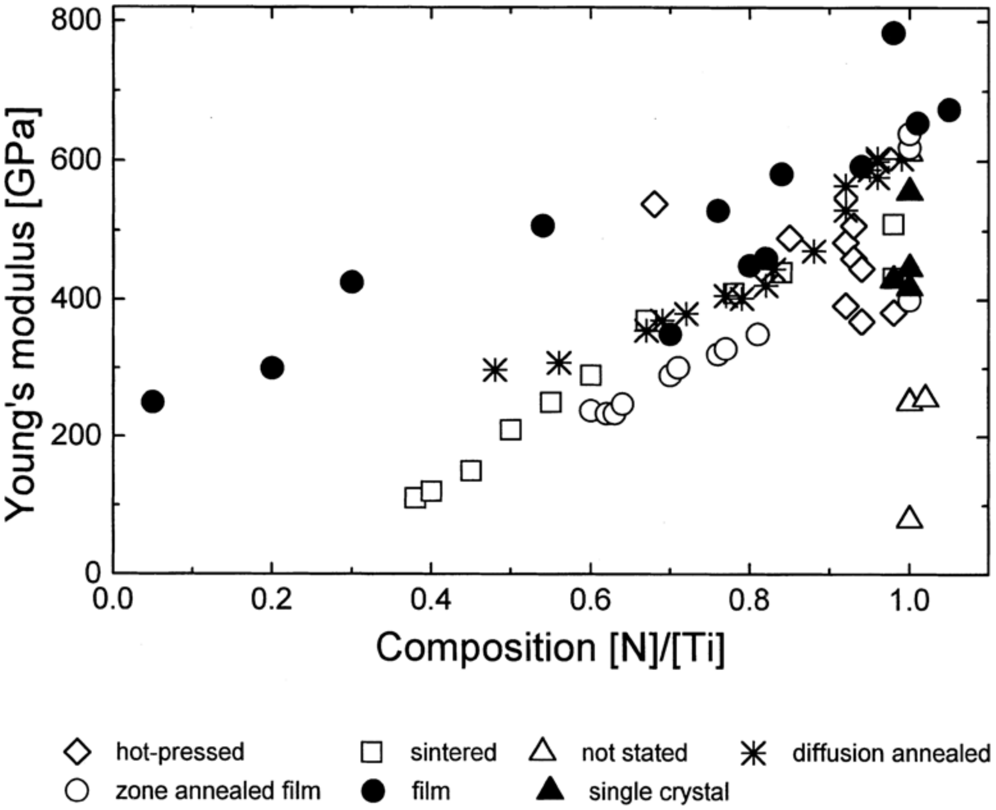

Figure 2.13. The Young's modulus of titanium nitride as a function of the nitrogen content is seen to change for various methods of preparation [59].

CHAPTER III

RESEARCH METHODOLOGY

3.1 Pulsed Laser Deposition: Principles, Advantages and Applications

Lasers are of great interest in many areas, for both scientific and industrial purposes because of their monochromatic, narrow and low divergence beam. The development of high beam energy lasers enabled new applications such as laser annealing of semiconductors, surface cleaning by desorption and ablation, improved surface hardening with laser-induced rapid quenching, and pulsed laser deposition for growing thin films. The last of those is the main technique for deposition of the metal nitrides studied in this thesis [60].

Immediately after the first high power lasers became available, many theoretical and experimental studies about the laser-target interaction (solid or gas) were made. The ease with which materials were vaporized suggested that the intense laser radiation could be used to deposit thin films. The first demonstration of the idea of depositing thin films was done in 1965 by Smith and Turner [61]. However, experimental work was fairly slow paced for the next two decades with fewer than 100 publications, and a low figure compared to work in other technologies. In the mid 70s, the development of the Q-switch made it possible to have extremely short pulses with very high pulse density. However, pulsed laser deposition had its major lift when the successful growth of high T_c superconducting films was reported in the late 80s [62].

The main advantage of using lasers for materials processing is given by the characteristics: monochromaticity, high energy density, and directionality. Monochromaticity permits the control of the depth of heat treatment or selectivity. The high energy of the laser and its directionality allow for a strongly localized heat and photo treatment of materials with a spatial resolution better than its wavelength. Additionally, other very important advantages of pulsed laser deposition are: reproduction of the target stoichiometry, little contamination, and in situ control of thin film properties. Pulsed laser deposition has been shown to be a very versatile technique. By choosing the appropriate laser wavelength, thin films of many materials can be deposited [63].

The Pulsed Laser Deposition (PLD) system is quite simple. Figure 3.1 shows a schematic of the experimental setup. It consists of a target holder and a substrate holder located in a high vacuum chamber maintained by a turbomolecular pump. The bulk target material is oriented at an angle of 45^o with respect to the incident laser beam. A high-power laser is used as the external energy source that vaporizes the target materials to deposit thin films. A set of optical components is used to focus and raster scan the laser beam over the target surface. The evaporated material is deposited onto a substrate placed parallel to the target surface at distance of 3-5 cm. The temperature of the substrate can be adjusted from room temperature to 800^oC. The deposited film quality depends on parameters such as substrate temperature, laser energy density, pulse repetition rate, pressure in the chamber, and substrate-target distance. The decoupling of the vacuum hardware and the evaporation power source makes this technique so flexible that it is easily adaptable to different operational modes without the constraints found in internally powered evaporation sources. Film growth can be carried out in a reactive environment containing any kind of gas with or without plasma excitation. It can also be operated with other types of evaporation sources in a hybrid like approach.

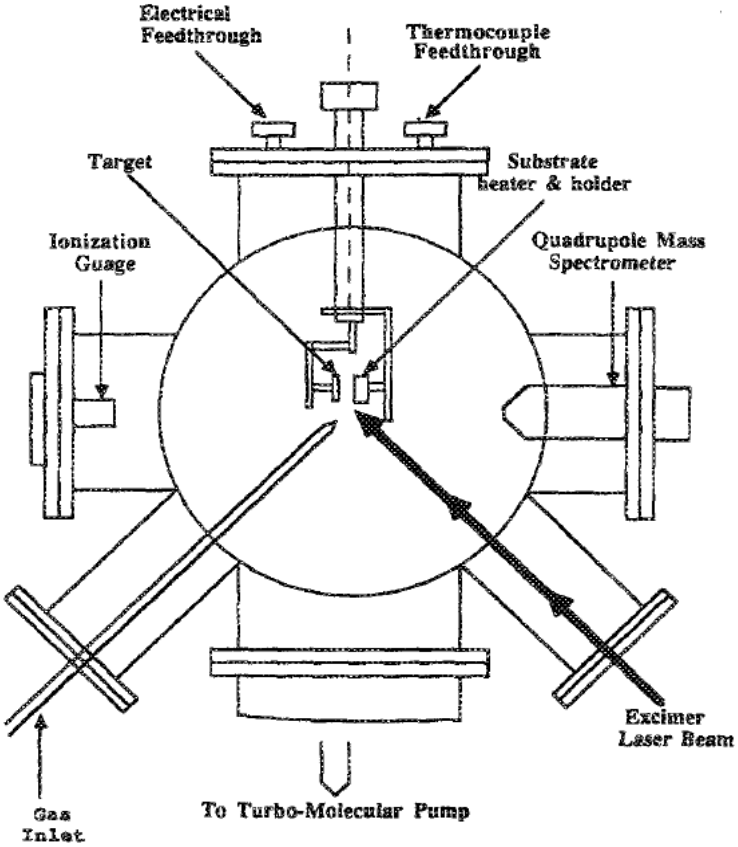

Figure 3.1. Schematic diagram of a single target pulsed laser deposition system [64].

Theoretically, the PLD technique is a very complex physical phenomenon. The theoretical descriptions come from multidisciplinary fields and combine for both equilibrium and non-equilibrium processes. Most important, the mechanism for laser ablation depends on the laser characteristics, as well as the physical, chemical, and thermodynamic properties of the target. When the laser radiation is absorbed by a solid surface, the electromagnetic energy is first converted into an electronic excitation and then into thermal, chemical, and mechanical energy to cause evaporation, ablation, excitation, plasma formation, and exfoliation. The evaporation causes a plume which consists of a mixture of energetic species including micro sized particles, molten globules, clusters, molecules, atoms, ions, and even electrons. A very short collision free path happens inside the plume. Immediately after the laser radiation, the plume expands from the target surface to form a jet nozzle with hydrodynamic flow characteristics.

The basic PLD physical principles described in the following subsections are adapted from Singh et al. [64, 65]. The physical stages for understanding PLD are the laser-target interactions during the pulse duration (about 25 ns duration) and after, which can be classified into three separate regimes. The three regimes are: (i) interaction of the laser beam with the target material resulting in the evaporation of the surface layers, (ii) interaction of the evaporated material with the incident laser beam resulting in an isothermal plasma formation and expansion, and (iii) anisotropic adiabatic expansion of the plasma leading to the characteristic nature of the laser deposition process. The first two initial regimes take place at the start and through the laser pulse duration, the third regime starts right after the laser pulse terminates. Figure 3.2 shows the stages during the short pulsed laser period associated with the first two regimes of the laser-target interaction.

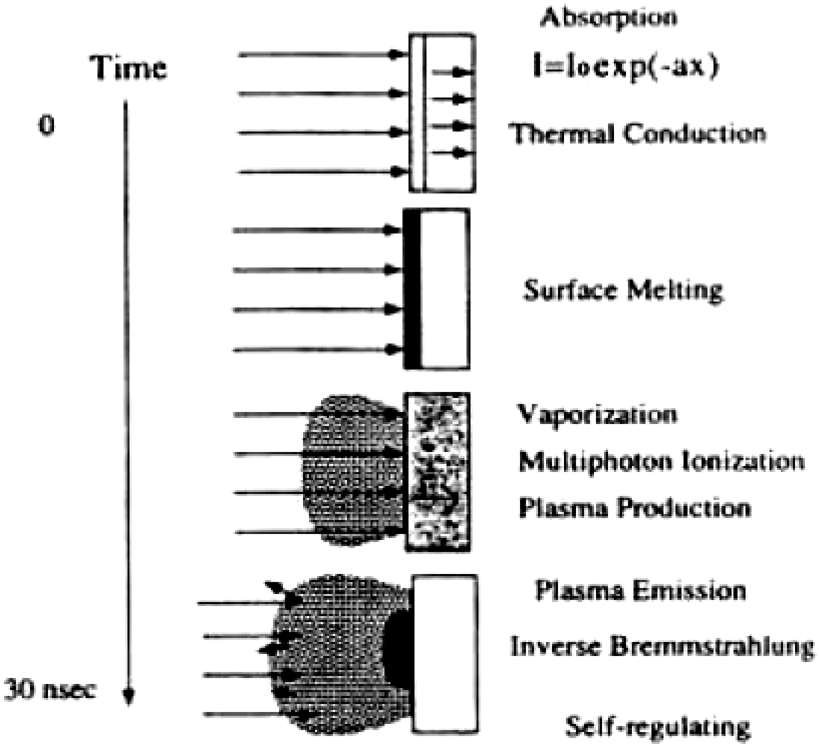

Figure 3.2. Representation of the laser target interaction stages during the short pulsed laser period [64].

3.1.1 Interaction of the Laser Beam with the Bulk Target Material

The removal or sputtering of the material from the target by laser irradiation depends on the interaction of the laser beam and the target. The intense heating of the surface layers by the high energy nanosecond laser pulses results in the melting and evaporation of the surface layers. The thermal history parameters such as heating rate, melting and evaporation depend on: (a) lasers parameters (pulse energy density *E*, pulse duration τ, shape of the laser pulse, and wavelength λ), and (b) materials properties (reflectivity, absorption coefficient, heat capacity, density, thermal conductivity, etc). The heating and melting process essentially involves the solution of a three-dimensional heat flow problem that can be approximated by a one-dimensional heat flow equation with the appropriate boundary conditions, taking the phase changes of the material into account. The approximation can be used because the laser beam size is much larger than the melt depth. The equation reduces to:

$$\rho_i(T)C_P(T)\frac{\partial T_i(x,t)}{\partial t} = \frac{\partial}{\partial t}\left(K_i(T)\frac{\partial T_i(x,t)}{\partial x}\right) + I_o(t)\{1 - R(T)\}e^{-a(T)x} \text{ ……...…………....(3.1)}$$

Where:

x : direction perpendicular to the sample

t : time

i : 1, 2 refers to the solid and liquid interface respectively

$\rho_i(T)$: Temperature dependent density

$C_P(T)$: Thermal heat capacity per unit mass of the target material

$R(T)$: Temperature dependent reflectivity

$a(T)$: Absorption coefficient at the laser wavelength

$I_o(t)$: Time dependent incident laser intensity

K_i : Thermal conductivities of solid and liquid phases at the interface

An accurate numerical solution of this equation by the finite difference method provides the evaporation characteristics of the pulsed laser irradiated material. However, simpler calculations based on energy balance considerations can be applied to determine the evaporation characteristics as function of the laser and material parameters. By using simple energy balance considerations, the amount of material evaporated per laser pulse is calculated. The energy deposited by the laser beam on the target is equal to the energy needed to vaporize the surface layers plus the losses due to thermal conduction of the substrate and absorption by the plasma. The vaporization energy is given by the energy threshold E_{th} that represents the minimum energy above which appreciable evaporation can be observed. Plasma and other losses vary with pulse energy density, and E_{th} may vary with energy density too. Then, the heat balance equation is given by:

$$\Delta x_i = \frac{(1-R)(E-E_{th})}{\Delta H + C_v \Delta T} \quad \ldots\ldots\ldots\ldots\ldots\ldots\ldots\ldots\ldots\ldots(3.2)$$

where:

Δx_i : thickness of evaporated material

R : reflectivity

ΔH : latent heat of vaporization

C_v : volumetric heat capacity

ΔT : maximum temperature rise

This equation is valid for conditions where the thermal diffusion distance $\sqrt{2D\tau}$ is larger than the absorption length of the laser beam in the target material, $1/\alpha_t$. The term D refers to the thermal diffusivity and τ refers to the laser pulse duration.

3.1.2 Interaction of the Laser Beam with the Evaporated Material

The high surface temperature (> 2000K) induced by the high power nanosecond pulse laser beam interacting with the target material, results in the emission of positive ions and electrons from the surface. The emission of electrons from a solid surface can be described by the Richardson's equation which shows an exponential increase in the electron emission as a function of temperature. The thermionic emission of positive ions can be calculated by the Langmuir-Saha equation, which also shows a similar relation to temperature as the electron emission. This equation is expressed as:

$$\frac{i_+}{i_o} = \left(\frac{g_+}{g_o}\right)\exp^{(\phi - I)/KT} \qquad \text{...(3.3)}$$

where i_+ and i_o are the positive and neutral ion fluxes leaving the surface at a temperature T, g_+ and g_o represent the statistical weight of the positive ionic and neutral states, ϕ is the electron work function, and I is the ionization potential of the material coming from the target surface. Since $I > \phi$, the fraction of the ionized species increases with increasing the temperature. The surface temperature at almost the boiling point of the target material (~ 3000K) with higher temperatures can be achieved in the evaporated plasma as a result of interaction with the laser. The penetration and absorption of the laser beam by the plasma depends on the electron-ion density, temperature, and the wavelength of the laser radiation. The penetration, absorption and reflection of the laser radiation depend on the plasma frequency v_p, which, to allow penetration and absorption, should be lower than the laser frequency. Otherwise all the radiation would be reflected by the plasma. As an example, an excimer laser (KrF) wavelength of λ=248 nm, has a laser frequency of 12.097×10^{14} s^{-1}. The relationship between frequency and electron density of the plasma can be expressed as:

$$v_p = 8.9 \times 10^3 n_e^{0.5} \qquad (3.4)$$

where n_e represents the electron concentration in the plasma. Using equation 3.4, the calculated critical electron density for reflection of the laser radiation by the plasma is found to be 1.35×10^{22} cm^{-3}. The value of the critical electron density is comparable to that of the concentration of atoms in a solid or liquid. The existence of a diffused plasma boundary and the gradual decrease in the plasma density away from the surface results in an even much lower density than the calculated value. Then, the energy losses caused by the reflection of the excimer laser from the plasma are assumed to be minimal.

The evaporated material out of the hot target surface is further heated by the absorption of the laser radiation. Although the laser evaporation for the deposition of thin films occurs at much lower power densities, where plasma temperatures are of the order of 10000 K, the heating mechanism and other physical phenomena are similar to the laser-generated high temperature plasma. The initial temperature of the evaporated material depends on the absorption of energy by the plasma. The primary mechanism of absorption for the ionized plasma is a result of the electron-ion collisions. The absorption occurs by an inverse Bremmstrahlung process, which refers to the absorption of a photon by a free electron. Nevertheless, at the very beginning of a laser pulse when very low electron and ion densities and a large number of neutral atoms are present, free-free transitions relating neutral atoms may be the cause of the primary absorption mechanism. A slight increase in ion density makes the free-free transitions involving ions take over and become the dominant mechanism for laser absorption. The absorption coefficient α_p (cm^{-1}) of the plasma for free-free transitions involving ions is given by the expression,

$$\alpha_p = 3.69\times 10^{8}\left(\frac{Z^3 n_i^2}{T^{0.5}v^3}\right)\left[1-e^{-hv/kT}\right]\text{......................................(3.5)}$$

where Z, n_i and T represent, the average charge, ion density, and plasma temperature, respectively; h, K, and v are the Planck constant, Boltzmann constant, and frequency of the laser radiation respectively. The laser energy is highly absorbed if ($\alpha_p X$) is large, with X being the perpendicular distance to the target of the expanding plasma. Then, equation 3.5 shows that the absorption coefficient of the plasma is proportional to n_i^2. Thus the plasma absorbs the laser at distances very close to the target where the density of the ionized species (electrons and ions) is high. The term $\left[1-e^{-hv/KT}\right]$, in equation 3.5, represents the losses related to stimulated emission and depends on the plasma temperature and also the laser wavelength. For a KrF excimer laser, $\lambda = 248$ nm, the exponential term becomes unity for $T << 60\ 000$ K and can be approximated by $h\nu/KT$ for $T >> 60\ 000$ K. The absorption term also shows a $T^{-3/2}$ temperature dependence at high temperatures (T >> 60 000 K) and $T^{-0.5}$ dependence at low temperatures (T >> 60 000 K). The frequency variation of the absorption coefficient changes from ν^2 to ν^3, depending on the value of $h\nu/kT$. The leading plasma edge high expansion velocities added to the very rapid decrease of electron and ion makes the plasma transparent to the laser beam at a large distance from the target surface. Due to the plasma being constantly augmented at the inner edge by the evaporated target material for the duration of the laser pulse, a high density of ions is produced near the surface of the target. The area in the proximities of the target surface is continuously absorbing the laser radiation through the duration of the laser pulse, while the outer edge of the plasma is transparent to the laser beam. Based on these observations, a diagram of the interaction between the laser beam, the plasma and the target material is shown in Figure 3.3. The diagram clearly shows that through the duration of the laser pulse, four separate regions can be distinguished: (A) unaffected bulk target, (B) evaporating target surface, (C) area near the surface absorbing the laser beam, and (D) rapidly expanding outer edge which is transparent to the laser.

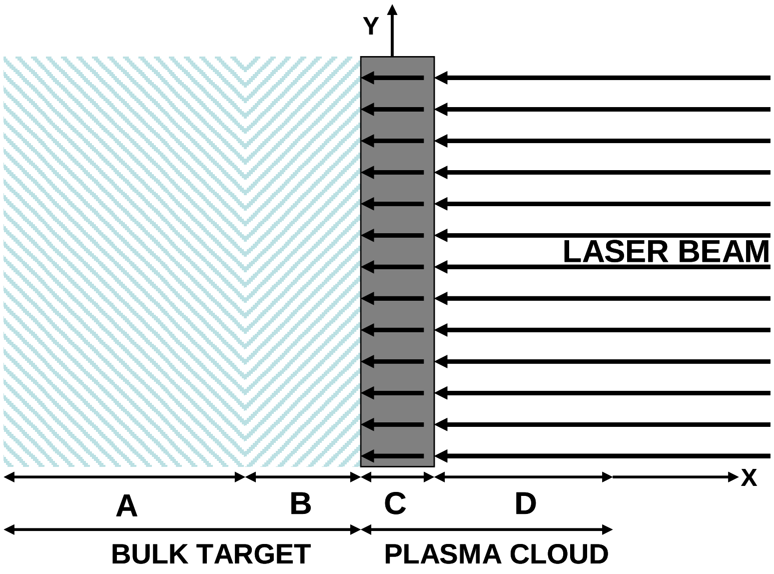

Figure 3.3. Schematic diagram showing the different phases present during laser irradiation on a target: (A) unaffected bulk target, (B) evaporating target material, (C) dense plasma area near the surface absorbing the laser radiation, and (D) expanding plasma outer edge transparent to the laser beam [64].

It is reasonable to assume that during the duration of the laser pulse a constant temperature is maintained near the surface of the target. A dynamic equilibrium exists between the plasma absorption and the rapid transformation of thermal energy into kinetic energy. These two mechanisms control the isothermal temperature of the plasma. The rapid expansion of the plasma in a vacuum is a result of large density gradients. The plasma, which is absorbing the laser energy, can be simulated as a high temperature-high pressure gas which is initially confined to very small dimensions and then suddenly allowed to expand in the vacuum. Because of the large pressure gradients initially present near the outer edge (vacuum), very high expansion velocities are induced at this edge. In the initial stages of the plasma expansion, when the particle density is of the order of 10^{19}-10^{20} cm^{-3}, the mean free path of the particles is short, and the plasma behaves as a continuum fluid. The equations of gas dynamics can be applied to simulate the expansion. The density, pressure and velocity profiles in the plasma are presented in Figure 3.4; the figure shows that at the inner edge of the plasma, the density is at a maximum, while the velocity is at a minimum. When the expansion velocities increase, the acceleration starts to diminish and ultimately becomes zero; this results in the characteristic elongated shape of the plasma.

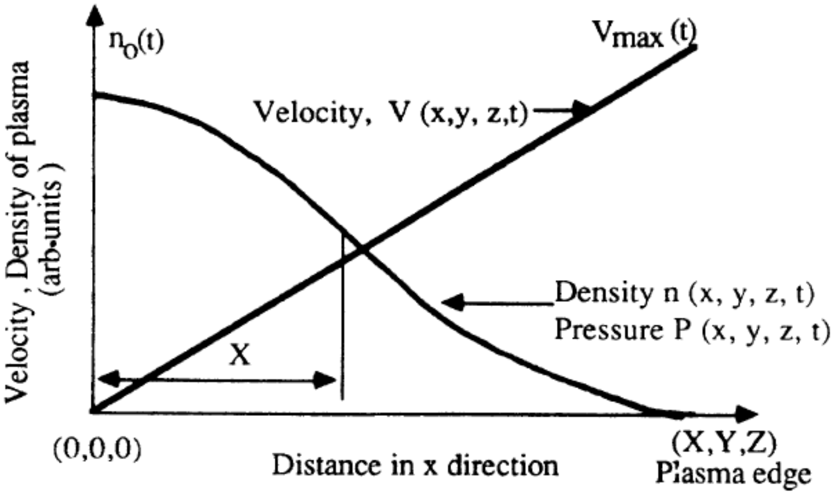

Figure 3.4. Curve profiles showing the density, pressure, and velocity gradients of the plasma in the x direction, perpendicular to the target surface. The density and plasma gradients are monotonically decreasing from the target surface with a linear increase in the velocity [64].

3.1.3 Adiabatic Plasma Expansion and Deposition of Thin Films

After the termination of the laser pulse, no particles are evaporated or injected into the inner edge of the plasma and laser energy absorption by the plasma is none. The following paragraph analyzes the adiabatic expansion of the plasma into vacuum after the termination of the laser pulse. The adiabatic expansion relates temperature and dimensions of the plasma by the adiabatic thermodynamic equation:

$$T\left[X(t)Y(t)Z(t)\right]^{\gamma-1} = const \qquad (3.6)$$

where γ is the ratio of the specific heat capacities at constant pressure and volume. The thermal energy is rapidly transformed into kinetic energy, with the plasma attaining extremely high expansion velocities. In the adiabatic expansion regime, the velocity of the plasma increases due to a decrease in thermal energy of the plasma. As there is no injection of particles in the inner edge of the plasma, the density and pressure gradients can be expressed in a similar form as when taking into account the injection of particles into the plasma. The equations of the gas dynamics which dictate the expansion of the plasma are the same as in the previous regime expect that the equation of energy and adiabatic equation of state also need to be solved. The adiabatic equation of state is given as,

$$\frac{1}{P}\left[\frac{\partial P}{\partial t} + \bar{v} \bullet \nabla P\right] - \frac{\gamma}{n}\left[\frac{\partial n}{\partial t} + \bar{v} \bullet \nabla n\right] = 0 \qquad (3.7)$$

and the equation of temperature is given by,

$$\frac{\partial T}{\partial t} + \bar{v} \bullet \nabla T = (1-\gamma)T.\nabla \bullet \bar{v} \text{ ....} (3.8)$$

We have assumed that there are no spatial variations in the plasma temperature, or $\nabla T = 0$. Therefore, the initial transverse dimension (Y or Z) are in the millimeters range while in the perpendicular dimension (X) the values are much smaller and in the micrometer range corresponding to the expansion length in the isothermal regime. As the velocities are dictated by these lengths, the highest velocities are in the direction of the smallest dimension giving rise to the characteristic elongated plasma shape outward from the target surface [64, 65].

3.2 Methods for Characterizing Thin Films

The characterization of the thin films studied in this thesis is performed by using experimental non-destructive and destructive techniques that allows the determination of their physical and chemical properties, crystal structures, defects and impurities presence, etc. The use of these techniques is important in order to measure, understand and optimize thin films properties such as mechanical, electronic, optic and magnetic properties.

The electrical, chemical, and structural properties of TiN, TaN and HfN thin films as Cu diffusion barriers for metallization and interconnects for the next generation of devices need to be studied in detail. The most extensively used techniques during the scope of this research are described in detail in the following pages.

3.3 X-ray Diffraction (XRD)

X-ray diffraction (XRD) is a very important non-destructive experimental technique used for characterizing materials in order to obtain information about their crystalline or amorphous structure. The early successful applications for structure determination were done by William Laurence Bragg and his father Sir William Henry Bragg in 1913; they later received the Nobel Prize in Physics (1915) for this work. The success of the technique has enabled scientists to determine the crystal structures of metal and alloys, minerals, polymers, organic and inorganic compounds. X-ray diffraction of thin films addresses important properties such as crystal structure, lattice constant, preferred orientation, defects, stress or strain, etc [66]. The following pages give a basic description of this technique which can be divided as: x-rays, lattice planes and Bragg's law and thin film x-ray diffraction.

3.3.1 X-rays

X-rays were discovered in 1895 by the German physicist Wilhelm C. Roentgen and were named as such because at that time the nature of it was unknown. X-rays are electromagnetic radiation with typical photon energies between 100 eV and 100 keV. For diffraction applications, only short wavelength x-rays (hard x-rays) in the range of 0.1 angstrom to a few angstroms (1 keV to 120 keV) are used. Because the wavelength of these hard x-rays is comparable to the size of atoms, they are ideally suited for probing the structural arrangement of atoms and molecules in a wide range of materials. The energetic x-rays can penetrate deep into the materials and provide information about their bulk structure.

X-rays are produced generally by either x-ray tubes or synchrotron radiation. In an x-ray tube a focused electron beam is accelerated across a high voltage field which bombards a stationary or rotating solid target. As electrons collide with atoms in the target and slow down, a continuous spectrum of x-rays is generated and emitted, which is termed as Bremmstrahlung radiation. The high energy electrons also eject inner shell electrons in atoms through the ionization process. When a free electron fills the shell, an x-ray photon with energy characteristic of the target material is emitted. Common targets used in x-ray tubes include Cu and Mo, which emit 8 keV and 14 keV, x-rays with corresponding wavelengths of 1.54 Å and 0.8 Å, respectively. In recent years synchrotron facilities have become widely used as preferred sources for x-ray diffraction measurements. Synchrotron radiation is emitted by electrons or positrons traveling at near light speed in a circular storage ring. These powerful sources, which are thousands to millions of times more intense than laboratory x-ray tubes, have become indispensable tools for a wide range of structural investigations and brought advances in numerous fields of science and technology [67].

3.3.2 Lattice Planes and Bragg's Law

X-rays primarily interact with electrons in atoms. When x-ray photons collide with electrons, some photons from the incident beam will be deflected away from the direction where they original travel, much like billiard balls bouncing off one another. If the wavelength of these scattered x-rays did not change (i.e. x-ray photons did not lose any energy), the process is called elastic scattering (Thompson Scattering) in that only momentum has been transferred in the scattering process. These are the x-rays that we measure in diffraction experiments, as the scattered x-rays carry information about the electron distribution in materials. On the other hand, in the inelastic scattering process (Compton Scattering), x-rays transfer some of their energy to the electrons and the scattered x-rays will have different wavelengths than the incident x-rays. Diffracted waves from different atoms can interfere with each other and the resultant intensity distribution is strongly modulated by this interaction. If the atoms are arranged in a periodic fashion, as in crystals, the diffracted waves will consist of sharp interference maxima (peaks) with the same symmetry as in the distribution of atoms. Measuring the diffraction pattern therefore allows us to determine the distribution of atoms in a material. The peaks in x-ray diffraction patterns are directly related to the atomic distances. For example consider an incident x-ray beam interacting with the atoms arranged in a periodic manner (2 dimensions) as shown in Figure 3.5. The atoms, represented as green spheres in the figure, can be viewed as forming different sets of planes in the crystal (colored lines in figure on top). For a given set of lattice plane with an inter-plane distance of *d*, the condition for a diffraction (peak) to occur can be simply written as:

$$2d\sin\theta = n\lambda \qquad (3.9)$$

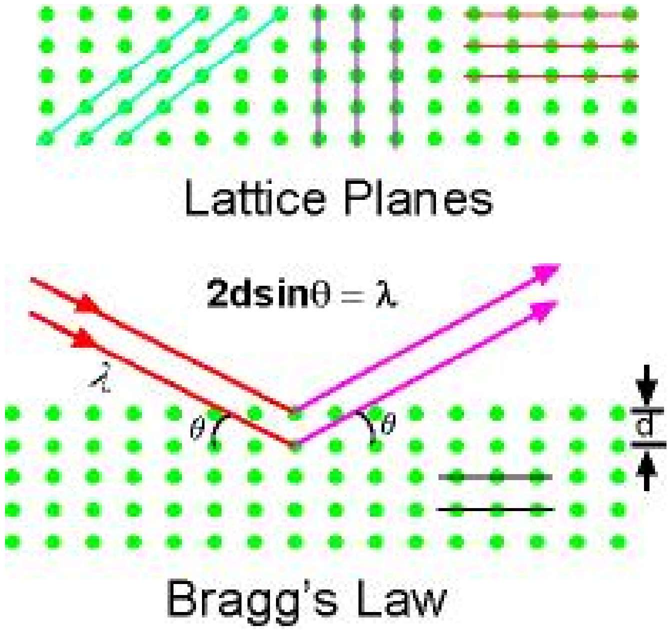

Figure 3.5. (a) A two dimensional periodic array of atoms that forms different planes in the crystal, (b) diffraction for a set of planes with inter-plane distance d which is conditioned to Bragg's Law [68].

Equation 3.9 is known as Bragg's law with variables such as: the wavelength of the x-ray (λ), the scattering angle (θ), and an integer number (n) representing the order of the diffraction peak. Bragg's Law is one of most important laws used for interpreting x-ray diffraction data.

It is important to point out that although we have used atoms as scattering points in this example, Bragg's Law applies to scattering centers consisting of any periodic distribution of electron density. In other words, the law holds true if the atoms are replaced by molecules or collections of molecules, such as colloids, polymers, proteins and virus particles.

3.3.3 Thin Film X-ray Diffraction

Thin film diffraction refers not to a specific technique but rather a collection of x-ray diffraction techniques used to characterize thin film samples grown on substrates. These materials have important technological applications in microelectronic and optoelectronic devices, where high quality epitaxial films are critical for device performance. Thin film diffraction methods are used as important process development and control tools, as hard X-rays can penetrate through the epitaxial layers and measure the properties of both the film and the substrate. There are several special considerations for using x-ray diffraction to characterize thin film samples. First, reflection geometry is used for these measurements as the substrates are generally too thick for transmission. Second, high angular resolution is required because the peaks from semiconductor materials are sharp due to very low defect densities in the material. Consequently, multiple bounce crystal monochromators are used to provide a highly collimated x-ray beam for these measurements. The basic x-ray diffraction measurements made on thin film samples include:

- Precise lattice constants measurements derived from 2θ - θ scans, which provide information about lattice mismatch between the film and the substrate. The lattice mismatch is indicative of strain and stress.
- Rocking curve measurements made by doing a θ scan at a fixed 2 θ angle, the width of which is inversely proportionally to the dislocation density in the film and is therefore used as a gauge of the quality of the film.
- Superlattice measurements in multilayered heteroepitaxial structures, the superlattices manifest themselves as satellite peaks surrounding the main diffraction peak from the film. Film thickness and quality can be deduced from the data.
- Glancing incidence X-ray reflectivity measurements, which can determine the thickness, roughness, and density of the film. This technique does not require a crystalline film and works even with amorphous materials.
- Texture measurements to determine the orientation of crystalline grains in a polycrystalline sample.

The essential features of an x-ray spectrometer are shown in Figure 3.6. It is important to note that the incident beam and the diffracted beam are always coplanar; and the angle between the diffracted beam and the transmitted beam is always 2θ. X-rays from the tube *T* are incident on a sample *C* which may be set at any desired angle to the incident beam by rotation about an axis through *O*, which is the center of the spectrometer circle. *D* is the detector that measures the intensity of the diffracted x-rays; the sample can be rotated about *O* and set at any desired angular position. Thus by measuring the peak positions, one can determine the shape and size of the unit cell, and by measuring the intensities of the diffracted beams one can determine the positions of atoms within the unit cell. Conversely, if the shape and size of the unit cell of the crystal are known, one can determine the positions of all the possible lines of the film [66-68].

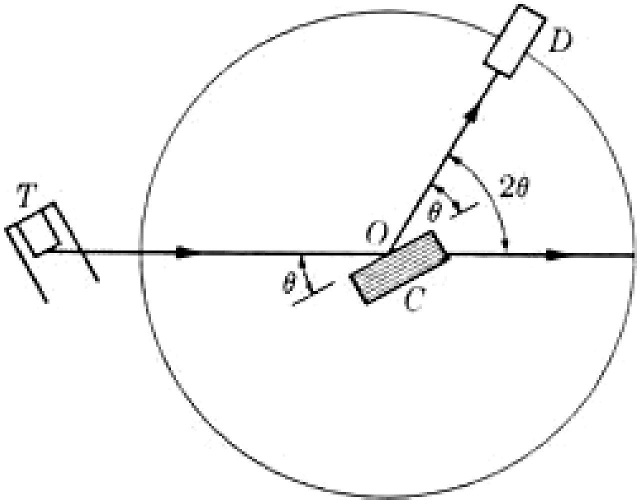

Figure 3.6. Schematic of an X-ray diffractometer [67].

3.4 Transmission Electron Microscopy (TEM)

A transmission electron microscope (TEM) has resolution and magnification capabilities that are over a thousand times beyond that offered by the light microscope.

Its basic operation is similar to the light microscope but uses electrons instead of light. What you can see with a light microscope is limited by the wavelength of the light. TEM use electrons as “light source” and their much lower wavelength make it possible to get higher resolution and magnification than light microscopes. TEM is a technique that has increasing application in materials science, semiconductor technology, biology, and other material or microstructure related fields. Recently, with the further pursuit of nanotechnology, TEM has become a must-use tool for characterization of nanometer features such as the geometry of patterned films, uniformity, thickness, coverage, surface morphology, topography and other related characteristics. A very well known use of the TEM is for the study of cross-sectional interface regions, interfacial reactions, device features and diffusion. In addition to the great capabilities of the TEM, its use in combination with other analytical techniques such as scanning TEM (STEM), electron energy loss spectroscopy (EELS), and energy dispersive x-ray spectroscopy (EDX) makes TEM a very powerful tool for imaging and chemical analysis down to the atomic domain. Finally, the current ongoing development of the in-situ TEM technique permits real time observations of the interplay between processing-property-microstructure relationships of materials. In this technique, some form of active stimulus is applied to a sample inside the electron microscope during simultaneous imaging. The in-situ TEM technique allows quantitative observations of the microstructural response and material properties to the changing conditions. The most common stimuli include thermal, mechanical, electrical, and magnetic, while some demonstrations of in-situ TEM include electromechanical, gaseous and liquid fluxes, and optical irradiation. In this part important parameters of TEM are listed as well as its diffraction and imaging techniques.

3.4.1 Resolution and Magnification

The resolving power of a microscope can be defined as the closest spacing of two points which can clearly be seen through the microscope to be distinguished as separate entities. It is important to distinguish that this is not the necessarily the same as the smallest point which can be seen with the microscope, which often is smaller than the resolution limit. Even if all the lenses of the microscope were perfect and introduced no distortions into the image, the resolution would nevertheless be limited by a diffraction effect. Inevitably, in any microscope, the light must pass through a series of restricted openings, the lenses themselves or the apertures. Whenever light passes through an aperture, diffraction occurs so that a parallel beam of light (seen as a spot) is transformed into a series of cones, which are seen as circles and are known as Airy rings. For light of a given wavelength, the diameter of the central spot is inversely proportional to the diameter of the aperture from which the diffraction is occurring. Consequently, the smaller the aperture, the larger is the central spot of the Airy disc. To have a clearly visible Airy disc, very small apertures are used, but the same effect occurs with relatively large apertures in light microscopes. The diffraction effect limits the resolution of a microscope because the light from a very small point in the object suffers diffraction, particularly by the objective aperture, and even an infinitesimally small point becomes a small Airy disc in the image. In order to make this disc as small as possible, the aperture must be as large as is feasible. Now let's consider the resolution of the microscope in more detail, starting with the Airy disc, Figure 3.7 shows the variation of the light intensity across the series of rings which make up the disc. The central spot is very much more intense than any other ring and in fact contains 84% of all the light intensity. Consequently for many purposes the rings can be ignored and we can assume that all the light falls in a spot of diameter d_1, where $d_1 \alpha$ 1/(aperture diameter). Consider how far apart two of these spots must be in the image before they are distinguishable as two separate spots; this distance is the resolution which was defined earlier. Rayleigh proposed a criterion which works well in most cases and has been used extensively ever since; when the maximum intensity of an Airy disc coincides with the first minimum of the second, then the two points can be distinguished. Figure 3.8 illustrates that the resolution limit is $d_1/2$. Microscopes apertures are normally referred to in terms of the semi-angle, α, which subtends the specimen. Then, it is possible to derive from diffraction theory an expression for the resolution,

$$r = \frac{0.61\lambda}{n \sin\alpha} \quad \text{..}(3.10)$$

where λ is the wavelength of the radiation, n is the refractive index of the medium between the object and the lenses, and α is the semi-angle of collection of the magnifying lens. The product, *nsin(α)*, is usually called the numerical aperture (NA).

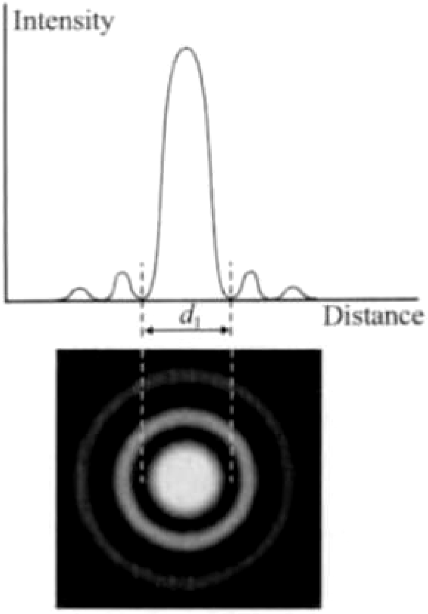

Figure 3.7. The variation of light intensity across a set of Airy rings. Most of the intensity (84%) lies within the first ring that is within a spot of diameter d_1 [69].

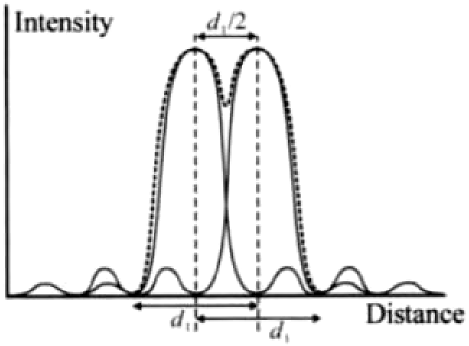

Figure 3.8. The intensity of the Airy rings from two neighboring pinholes. The intensity distributions from each of the pinholes separately are shown as solid lines; the combined profile from the two pinholes acting together is shown dotted. At the Rayleigh resolution limit, as shown here, the maximum intensity from one pinhole coincides with the first minimum from the other giving a resolution limit of $d_1/2$ [69].

Besides forming images with high resolution because of the short wavelength of an electron, the lenses of an electron microscope are able to further magnify these images. Magnification refers to the degree of enlargement of the diameter of a final image compared to the original. In practice, magnification equals a distance measured between two points on an image divided by the distance measured between these same two points on the original object, or

$$Mag = \frac{d(image)}{d(object)} \qquad (3.11)$$

Consequently, if the image distance between two points measures 25.5 mm while the distance between these same two points on the object measures 5 mm, then the magnification is 5.1.

There are at least three magnifying lenses in an electron microscope: the objective, intermediate, and projector lenses. The final magnification is calculated as the product of the individual magnifying powers of all of the lenses in the system [69].

3.4.2 Aberrations and Stigmatism

A number of imperfections in the lenses may reduce resolution. Astigmatism results when a lens field is not symmetrical in strength, but is stronger in one plane (north and south, for example) and weaker in another (east and west) so that only part of the image will be in focus at one time. A point would not be imaged as such, but would appear elliptical in shape, Figure 3.9; a cross would be imaged with either the vertical or horizontal arm, but not both, in focus at one time.

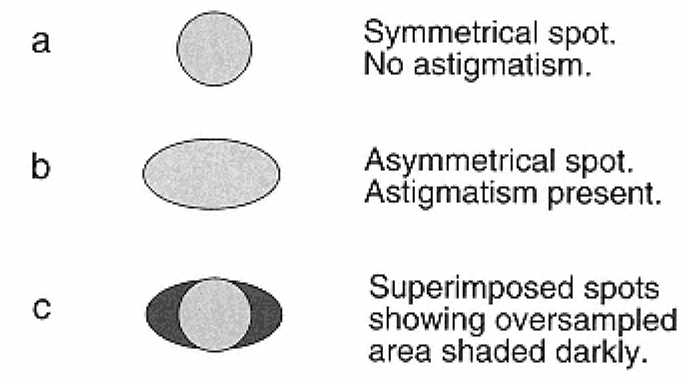

Figure 3.9. A spot suffering astigmatism that appears to be elliptical in shape [70].

Some causes of astigmatism are an imperfectly ground pole piece bore, no homogeneous blending of the pole piece metals, and dirt on parts of the column such as pole pieces, apertures, and specimen holders. Because it is impossible to fabricate and maintain a lens with a perfectly symmetrical lens field, it is necessary to correct astigmatism by applying a correcting field of the appropriate strength in the proper direction to counteract the asymmetry. Such a device is called a stigmator and can be found in the condenser, objective, and intermediate lenses of the electron microscope.

Chromatic aberration results when electromagnetic radiations of different energies converge at different focal planes. With a glass lens, shorter wavelength radiations are slowed down and refracted more than are longer wavelengths of light.

Effectively, the shorter, more energetic wavelengths of light (Violet) come to a shorter focal point than do the longer wavelengths (Red), Figure 3.10. In an electromagnetic lens, the reverse is true: shorter wavelength, more energetic electrons have a longer focal point than do the longer wavelength electrons. In both cases, however, chromatic aberration results in the enlargement of the focal point (similar to the Airy disc phenomenon caused by diffraction effects) with a consequential loss of resolution. Chromatic aberration can be corrected by using a monochromatic source of electromagnetic radiation. With glass lenses, one can use a monochromatic light (possibly by using a shorter wavelength blue filter). In an electromagnetic lens, one would insure that the electrons were of the same energy level by carefully stabilizing the accelerating voltage and having a good vacuum to minimize the energy loss of the electrons as they passed through the column. Thicker specimens give rise to a spectrum of electrons with varied energy levels and consequently worsen chromatic aberration. Thin specimens are therefore essential for high resolution studies.

Chromatic change in magnification occurs when thick specimens are viewed at low magnifications using a low accelerating voltage. The image appears to be sharp in the center, but becomes progressively out of focus as one move toward the periphery. This is because the lower energy electrons are imaged at a different plane than the higher energy electrons. The effect is maximal at the periphery of the image, since these electrons are closer to the lens coils and, thus, are more affected by the magnetic field. This problem may be minimized by using thinner specimens, higher accelerating voltages, higher magnifications, and by correcting any other distortions that may be present in the lens.

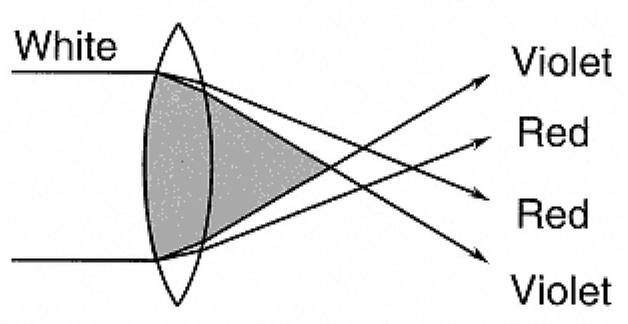

Figure 3.10. Chromatic aberration for a glass lens, shorter wavelengths (Violet) meet at a shorter focal point than of larger wavelengths (Red) at a larger focal point. The opposite case happens for an electromagnetic lens [70].

Spherical aberration is a result of the geometry of both glass and electromagnetic lenses, rays passing through the periphery of the lens are refracted more than rays passing along the axis. Unfortunately, the various rays do not come to a common focal point, resulting in an enlarged, unsharp point, Figure 3.11 (A). At some distance, however, one should encounter the sharpest possible point that would constitute the circle of minimum confusion (i.e., the smallest Airy disc) and the practical focal point of the lens. Spherical aberration may be reduced by using an aperture to eliminate some of the peripheral rays, Figure 3.11 (B). Although apertures must be used in the electron microscope to reduce spherical aberration as much as possible, they decrease the aperture angle and thereby prevent the electron microscope from achieving the ultimate resolving power specified in the equation for resolution (Equation 3.10).

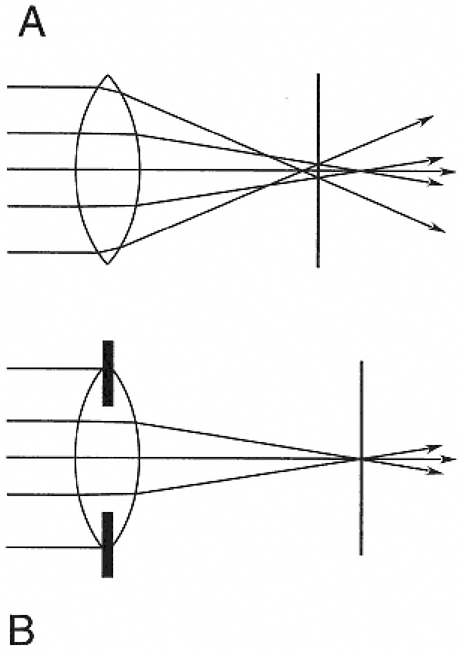

Figure 3.11. Spherical aberration in a lens. (A) Peripheral rays are refracted more than central rays, so that all rays do not converge to a common, small focal point. Instead, an enlarged, diffuse spot like the Airy disc will be generated. The vertical line indicates the one point where the point will be smallest (i.e., having the smallest circle of confusion). (B) Correction of spherical aberration with an aperture (here shown inside the lens) to cut out peripheral rays and thereby permit remaining rays to focus at a common small imaging point. Resolution will be improved since individual image points in the specimen will be smaller [70].

3.4.3 Depth of Field and Depth of Focus

The depth of field D_{fi}, shown in Figure 3.12, is the value of extreme specimen positions on both sides of the theoretical object plane of focus of the objective lens, without destroying the resolution. A specimen shift D/2 with respect to the object plane, results in a disc of radius $r=\alpha D/2$, where α is the objective angular aperture. In order to keep the resolution from diminishing, the diameter of this disk should be smaller than or equal to the resolution distance d, so that $\alpha D=d$. The larger the depth of field (D_{fi} ~500 Å), the better the probability that the specimen is focused on its whole thickness. The expression for the depth of field is given by,

$$D_{fi} = \frac{\lambda}{NA^2} \quad \text{..(3.12)}$$

Depth of focus D' is defined similarly in the final image plane as depth of field in the object plane. Now d'=dM and a'=a/M, where M is the final magnification. Thus depth of focus $D'=DM^2$. Magnification of the order of 10^5 would give depth of focus ~500 m, which means that the fluorescent screen position is not critical.

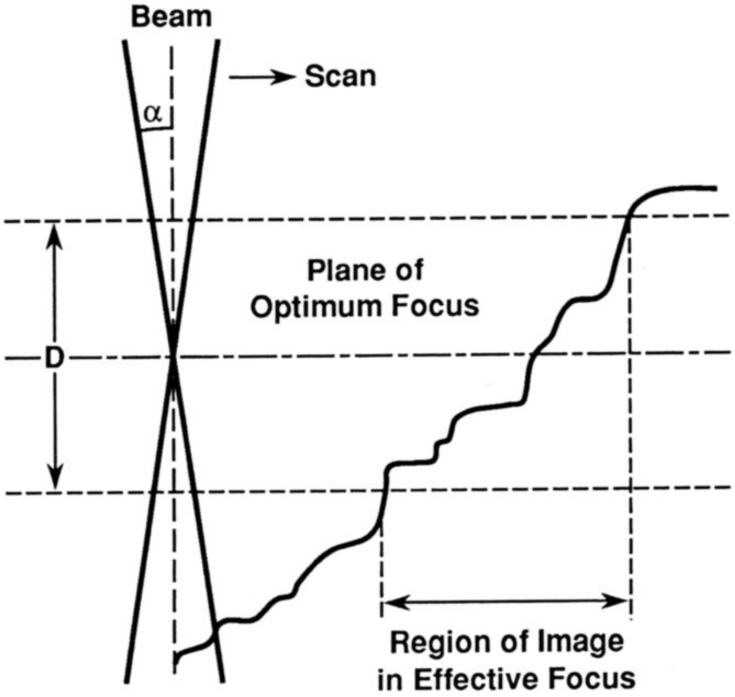

Figure 3.12. Schematic showing the depth of field D and its edges for optimal imaging [69].

3.4.4 Darkfield

In the normal operating mode of the transmission electron microscope, the unscattered rays of the beam are combined with some of the deflected electrons to form a brightfield image. As more of the deflected or scattered electrons are eliminated using smaller objective lens apertures, contrast will increase. If one moves the objective aperture off axis, as shown in Figure 3.13, left, the unscattered electrons are now eliminated while more of the scattered electrons enter the aperture. This is a crude form of darkfield illumination. Unfortunately, the off-axis electrons have more aberrations and the image is of poor quality.

Higher resolution darkfield images may be obtained by tilting the illumination system so that the beam strikes the specimen at an angle. If the objective aperture is left normally centered, it will now accept only the scattered, on-axis electrons and the image will be of high quality (Figure 3.13, right). Most microscopes now have a dual set of beam tilt controls that will permit one to adjust the tilt for either brightfield or darkfield operation. After alignment of the tilt for brightfield followed by a darkfield alignment, one may rapidly shift from one mode to the other with the flip of a switch. Both sets of controls also provide for separate stigmation controls to correct for any astigmatism introduced by the tilting of the beam to large angles.

The darkfield mode can be used to enhance contrast in certain types of unstained specimens (thin frozen sections) or in negatively stained specimens.

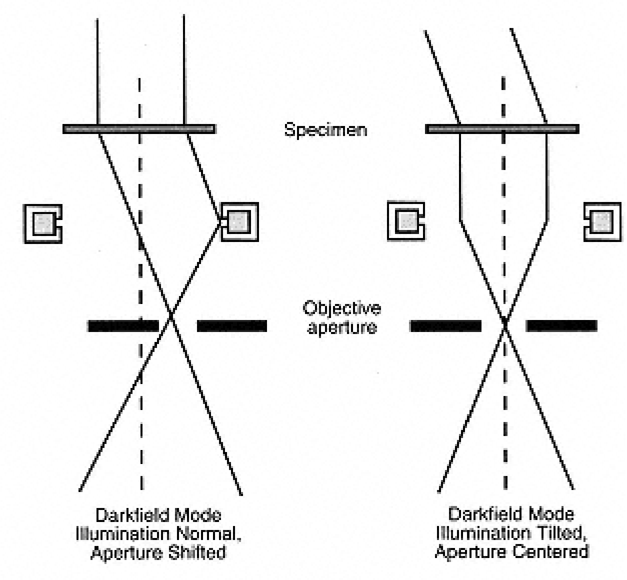

Figure 3.13. Schematic diagram showing two ways of setting up microscope for darkfield imaging: (left) displacement of objective aperture off-axis; (right) tilt of illumination system into on-axis objective aperture [70].

3.4.5 High Resolution

Most of the conditions used to achieve high resolution in the electron microscope are the opposite to the conditions discussed above for the high contrast mode. Since contrast will be lacking in these specimens, efforts should be made to boost contrast using appropriate specimen preparation and darkroom techniques, as described in the previous section. The following describes some considerations for obtaining high Resolution images:

- The objective lens should be adjusted to give the shortest possible focal length and the proper specimen holders used. In some systems, this is simply a matter of pressing a single button; however, in certain microscopes several lens currents must be changed concomitantly. Perhaps it may even be necessary to insert a different polepiece in the objective lens.
- Adjustments to the gun, such as the use of higher accelerating voltages, will result in higher resolution for the reasons already mentioned in the discussion on high contrast. Chromatic aberration may be further lessened by using field emission guns since the energy spread of electrons generated from such guns is considerably narrower. (The energy spread for tungsten = 2 eV while field emission = 0.2–0.5 eV.) In an electron microscope equipped with a conventional gun, a pointed tungsten filament will generate a more coherent, point source of electrons with better resolution capabilities.
- Use apertures of appropriate size. For most specimens, larger objective lens apertures should be used to minimize diffraction effects. If contrast is too low due to the larger objective aperture, smaller apertures may be used but resolution will be diminished. In addition, they must be kept clean since dirt will have a more pronounced effect on astigmatism. Small condenser lens apertures will diminish spherical aberration, but this will be at the expense of overall illumination. The illumination levels may be improved by altering the bias to effect greater gun emissions; however, this may thermally damage the specimen.

- Specimen preparation techniques may also enhance the resolution capability. Extremely thin sections, for instance, will diminish chromatic aberration. Whenever possible, no supporting substrates should be used on the grid. To achieve adequate support, this may require the use of holey films with a larger than normal number of holes. The areas viewed are limited to those over the holes.
- Conditions such as shorter viewing and exposure times will minimize contamination, drift, and specimen damage, and help to preserve fine structural details. Some of the newest microscopes have special accessories for minimal electron dose observation of the specimen and may even utilize electronic image intensifiers to enhance the brightness and contrast of the image. Anticontaminators over the diffusion pumps and specimen area will diminish contamination and resolution loss. High magnifications will be necessary, so careful adjustment of the illuminating system is important. It may take nearly an hour for the eyes to totally adapt to the low light levels, and this adaption will be lost if one must leave the microscope room. Alignment must be well done and stigmation must be checked periodically during the viewing session. The circuitry of the microscope should be stabilized by allowing the lens currents and high voltage to warm up for 1 to 2 hours before use. Bent specimen grids should be avoided since they may place the specimen in an improper focal plane for optimum resolution. In addition, they prevent accurate magnification

determination and are more prone to drift since the support films are often detached.

3.4.6 Electron Diffraction

A TEM can generate a diffraction pattern from a specimen. This is because the diffraction pattern is always present in the back focal plane of the objective lens. From the ray diagram shown in Figure 3.14, it is apparent that the forward scattered diffracted electrons come to a focal point (this is the back focal plane of the objective lens) but are excluded by the objective aperture. As will be shown, one of the operational requirements to obtain diffraction patterns may involve removal of the objective aperture or the use of a larger aperture. Although diffraction patterns are generated by all specimens, some patterns have more information about the nature of the specimen than do others. For instance, specimens with randomly or none periodically oriented atoms generate a diffuse electron diffraction pattern that simply confirms that the atoms of the specimen are not arranged in a repeating or periodic manner. By contrast, whenever the specimen or parts of the specimen consist of molecules or atoms with a repeating periodicity (as in a crystalline lattice), then a diffraction pattern is formed that may be useful in the identification of the crystal or molecule. Electron diffraction may give the spacing of the crystalline lattice and (since various crystals have unique lattice spacings and diffraction patterns) the chemical identity of the crystal. On the other hand, electron diffraction cannot be used to determine the quantity of a particular chemical that has been identified.

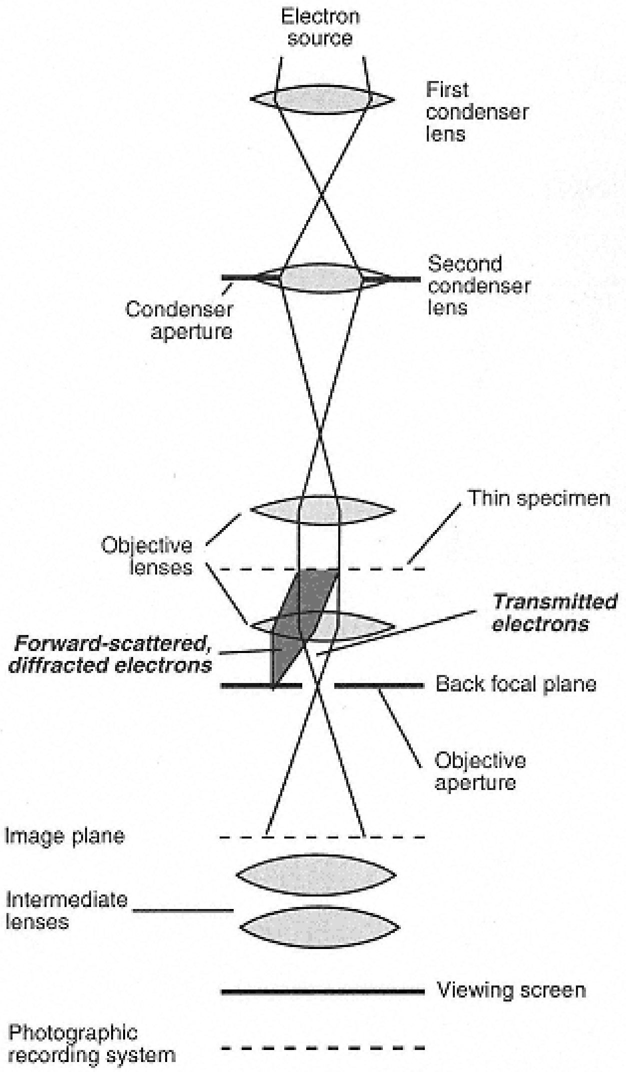

Figure 3.14. Schematic of lenses in a transmission electron microscope. Note the dashed line indicating one group of diffracted electrons that converge in the back focal plane of the objective lens [70].

If a beam of electrons strikes a crystalline structure at an appropriate angle (so-called Bragg angle) the electrons will be diffracted or "reflected" from the lattice planes. The reflection follows Bragg's law of diffraction. Some of the electrons that enter the lattice at the proper angle will be reflected by the various lattice planes in the same direction and at the same angle to come to focus in the back focal plane. This generates the diffraction pattern. In the case of an amorphous specimen, the electron beam that enters the specimen is diffracted in multiple directions and at various angles so that the electrons are unable to converge into a discrete spot and form a diffuse ring pattern instead. With a crystalline specimen, in order to obtain the proper Bragg angle, it is necessary to orient the specimen very precisely by tilting and rotating it relative to the electron beam until the diffraction pattern is obtained.

3.4.7 Single Crystal and Polycrystalline Patterns

A single crystal will generate a diffraction pattern consisting of spots, Figure 3.15 (left), with the layout of the spots depending on the type of crystal lattice (14 different types exist) being illuminated and the orientation of the crystal to the beam. In practice, one photographs the diffraction pattern and, in a properly calibrated microscope, measures the distances and angles between the spots to determine the distance "d" between lattice planes. Since the d spacings are unique for each crystal, one may look up the d spacings in a reference book or computer database and obtain an identification of the crystal. The derived expression from Bragg’s Law and the electron microscope camera length used for calculating the d spacings is given by,

$$d = \frac{\lambda L}{R} \qquad (3.13)$$

where d represents the lattice spacing, R the distance from the central bright spot to one of the spots or rings, L the camera length, and λ is the wavelength of the electron.

In a polycrystalline specimen, Figure 3.15 (right), many crystals are present all of which are generating spot patterns, so that the individual spots merge into rings surrounding a bright central spot (the undiffracted electrons). As in the previous example, the radius of the rings is related to lattice d spacings and can be calculate by using Equation 3.13.

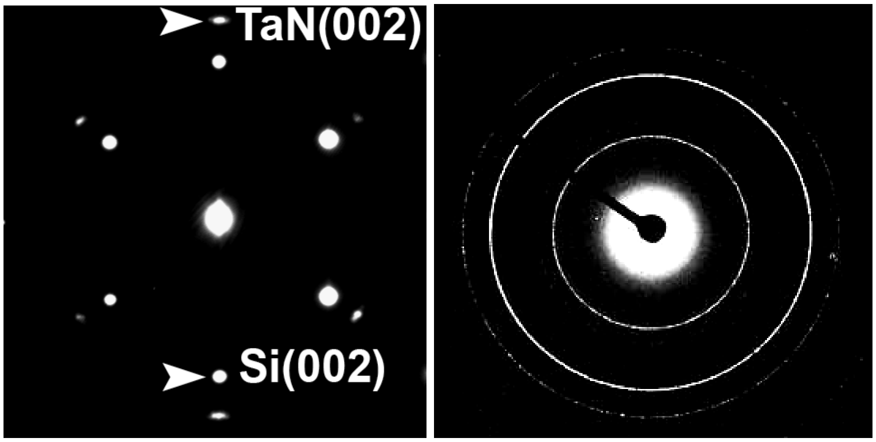

Figure 3.15. Electron diffraction pattern for a crystalline (left) TaN/TiN thin film on Si substrate deposited by PLD [18], and a polycrystalline (right) thin film of gold deposited onto a plastic film by evaporating the molten metal in a vacuum evaporator [70].

3.5 Four Point Probe (Resistivity)

The electrical resistivity of thin films is measured by the four-point probe (FPP) technique. The four-point probe technique is a good method for measuring thin films resistivity and its main advantage is producing an absolute measurement without recourse to calibrated standards. Moreover, it's simpler compared to an easy to do two point probe measurement where the interpretation of the data is far more difficult. The explanation of such a difficulty is because in a two point probe arrangement, each probe serves as a current and a voltage probe. Then a total resistance R_T between the probes is given by Equation 3.14 and also shown in Figure 3.16 with its major contributors R_p, R_c, R_{sp} and R_f , where R_c and R_{sp} are assumed to be identical for the two contacts. The contact resistance (R_c) is the results from the mechanical metal probe contacting the thin film; the spreading resistance (R_{sp}) is the resistance encountered by the current when it flows from the small probe to the thin film and thin film to the probe. The value of R_p can be measured by shorting the two probes but the values of R_c and R_{sp} can't be measured or calculated for a mechanical probe, so the resistivity can't be extracted from the total resistance obtained by two point probe measurements.

$$R_T = \frac{V}{I} = 2R_p + 2R_c + 2R_{sp} + R_f \quad \text{.......................................(3.14)}$$

R_p: probe resistance

R_c: contact resistance at metal probe/thin film contact

R_{sp}: spreading resistance under each probe

R_f: the thin film resistance

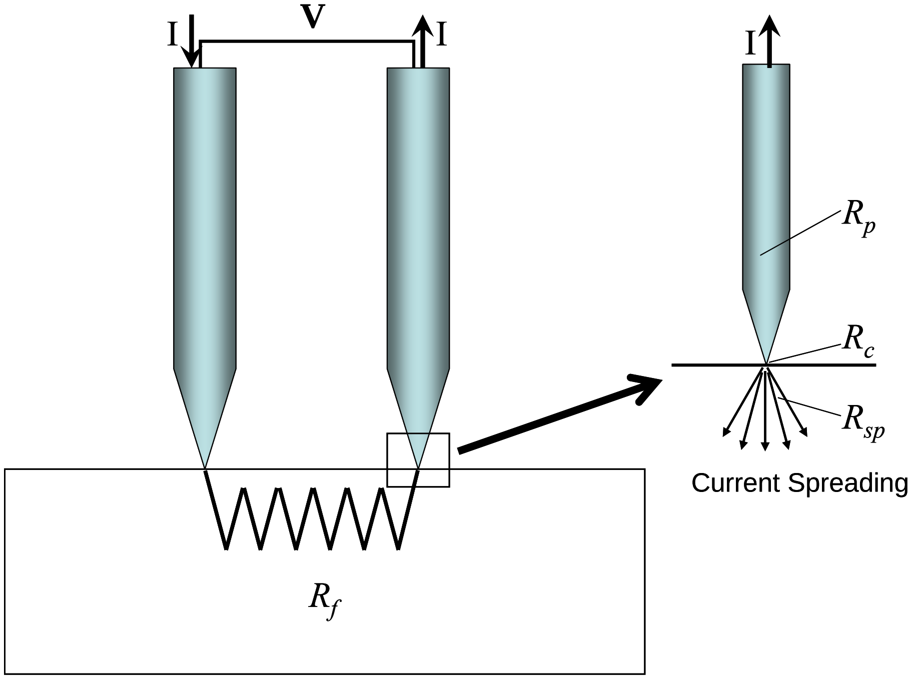

Figure 3.16. Schematic of a two point probe arrangement shows the probe resistance R_p, the contact resistance R_c, the spreading resistance R_{sp}, and the thin film resistance R_f.

The four-point probe technique is the alternative for measuring resistivity. Two probes carry the electrical current and the other two probes measure the voltage difference between them. This technique was originally proposed by Wenner in 1916 to measure the resistivity of the earth and is known as the *Wenner's method* by the geophysicist community. The four-point probe technique was originally adapted for the semiconductor industry in 1954 by Valdes [71]. The probes generally are collinear, in line, and with equal space between probes as shown in Figure 3.17, but other alternative configurations are possible. The use of four probes presents an important advantage over two probe measurements. Even though the two probes carrying current still have contact and spreading resistance, the same is not true for the other two probes which draws no current at all or have high impedance that results in very little current draw. The parasitic resistances R_p, R_c, and R_{sp} in the two voltage probes are negligibly small because of the very small current flowing through them. These four-point contact measurement techniques are usually known as the *Kelvin techniques*.

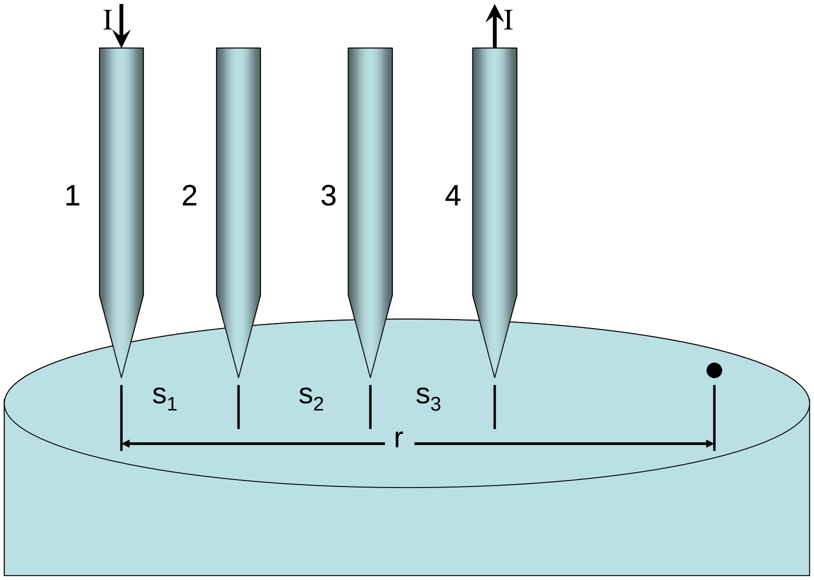

Figure 3.17. A collinear four point probe array.

In order to derive the four-point probe resistivity expression the following considerations are taking into account: (a) a current I is entering through probe 1 and leaving through probe 4 as shown in Figure 3.17, (b) the potential V at a distance r from an electrode carrying a current I in a material of resistivity is given by the relationship $V = \frac{\rho I}{2\pi r}$.

For probes resting in a semi-infinite medium as in Figure 3.17 with current entering through probe 1 and leaving probe 4, the voltage V_0 measured with respect to a zero reference potential is,

$$V_0 = \frac{\rho I}{2\pi}\left(\frac{1}{r_1} - \frac{1}{r_2}\right) \text{...} (3.15)$$

where r_1 and r_4 are the distances from probes 1 and 4, respectively. The minus sign accounts for the current leaving probe 4. For most four-point probes the spacing s_1, s_2 and s_3 are equal and the voltage between probes 2 and 3 is given by the expression:

$$V = V_2 - V_3 = \frac{\rho I}{2\pi s} \text{...} (3.16)$$

and the resistivity given by,

$$\rho = 2\pi s\left(\frac{V}{I}\right) \text{...} (3.17)$$

Thin films samples are not semi-infinite in either of the lateral or vertical dimensions, therefore the mentioned resistivity equation must be corrected for finite geometries with a factor F. The factor F must account for correcting the location of the probe near samples edges, sample thickness, sample diameter, probe placement and sample temperature. The correction factor is usually a product of several independent correction factors, as shown in the next section.

3.5.1 Correction Factors

The correction factors are calculated by the methods of images, complex variable theory, the method of Corbino sources, Poisson's equation, Green's functions, and conformal mapping. The following correction factors are for collinear (in-line) probes with an equal probe spacing and the correction factor F is a given as a product of three correction factors F_1, F_2 and F_3. F_1 corrects for the sample thickness, F_2 corrects for the lateral sample dimensions, and F_3 corrects for placement of the probes relative to the edge of the sample.

For the sample thickness correction factor, the thin film is conductive in nature but deposited on an insulating substrate. The thickness of the thin film, t, is usually smaller in value than the probes spacing *s*. Then the expression for the thickness correction factor is:

$$F_{11} = \frac{t/s}{2\ln\{[\sinh(t/s)]/[\sinh(t/2s)]\}} \quad \text{......................................(3.18)}$$

Additionally, for other conductive thin films on conductive substrates, the correction factor becomes:

$$F_{12} = \frac{t/s}{2\ln\{[\cosh(t/s)]/[\cosh(t/2s)]\}} \quad \text{.....................................(3.19)}$$

As mentioned before, most four-point probe measurements are made on insulating bottom surfaces or substrates. Then, for thin film samples (t<s/2), the F_{11} reduces to:

$$F_{11} = \frac{t/s}{2\ln(2)} \quad \text{..(3.20)}$$

And for very thin samples, that satisfy the conditions for F_2 and F_3 to be approximately unity, the resistivity becomes

$$\rho = \frac{\pi t}{\ln(2)}\frac{V}{I} = 4.532t\frac{V}{I} \quad \text{..(3.21)}$$

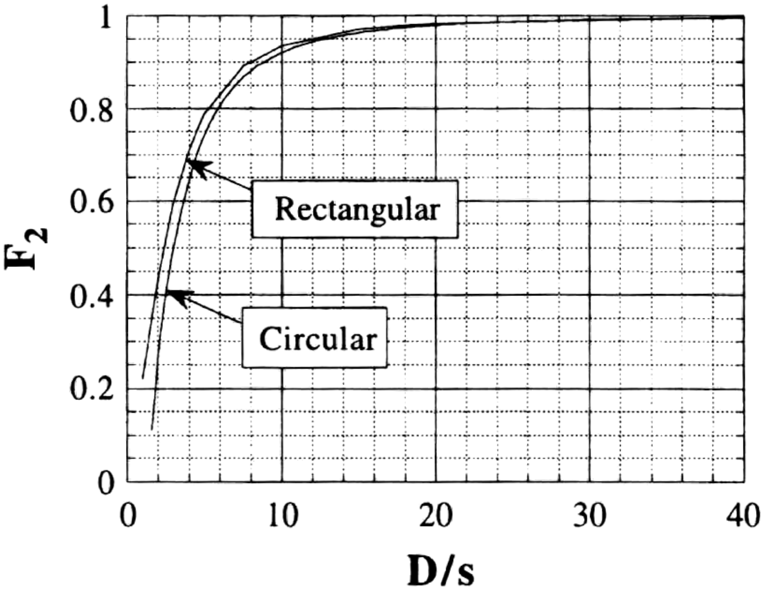

Figure 3.18. Wafer diameter correction factors versus normalized wafer diameter. For circular wafers D = wafer diameter; for rectangular samples D = sample width [72].

The other correction factor F_2 deals with the size of the sample and it is presented in Figure 3.18 where factors for a circular and rectangular sample are shown. The expression for this factor is given by

$$F_2 = \frac{\ln(2)}{\ln(2) + \ln\left\{\left[(D/s)^2 + 3\right] / \left[(D/s)^2 - 3\right]\right\}} \qquad (3.22)$$

The last correction factor, F_3, deals with the orientation of the collinear probes to the sample boundaries or edges as indicated in Figure 3.19 for conductive and non-conductive boundaries taken either perpendicular or parallel to the sample boundary [72].

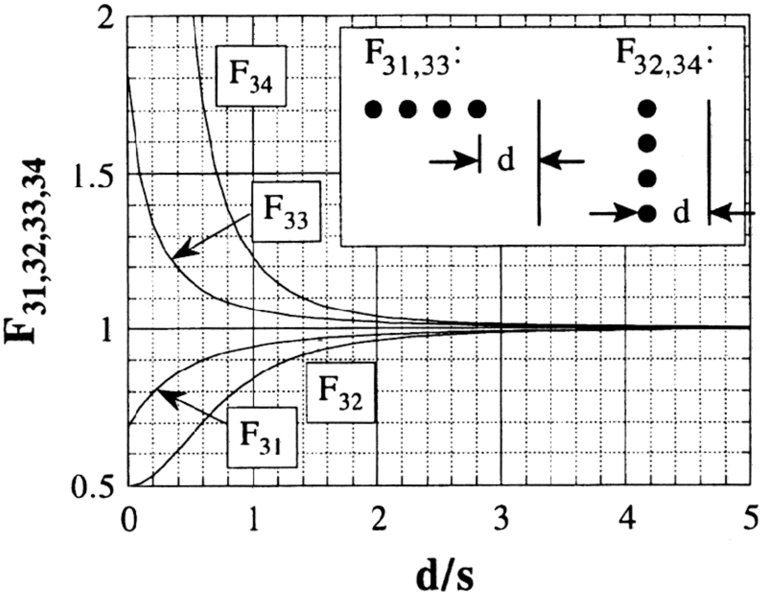

Figure 3.19. Boundary proximity correction factors versus normalized distance d from the boundary. F_{31} and F_{32} are for non conducting boundaries; F_{33} and F_{34} are for conducting boundaries [72].

CHAPTER IV

CUBIC TAN DIFFUSION BARRIERS FOR CU INTERCONNECTS USING AN ULTRA-THIN TIN SEED LAYER*

4.1 Overview

Epitaxial metastable cubic TaN (B1-NaCl) thin films were grown on Si (001) substrates using an ultra-thin TiN (B1-NaCl) seed layer, as thin as ~1 nm. The TiN/TaN stacks were deposited by pulsed laser deposition and kept below 25 nm, with the TiN thickness systematically reduced from 15 nm to ~1 nm. Detailed microstructural studies including X-ray diffraction, transmission electron microscopy (TEM) and high resolution TEM, and, preliminary Cu diffusion experiments all suggest that, the TiN seed layer thickness (~1 nm - 15 nm) has little or no obvious effects on the overall microstructure and the diffusion barrier properties of the TaN/TiN stacks.

---

*Reprinted from “TaN diffusion barrier for Cu interconnects using an ultra-thin TiN seed layer” by R.A. Araujo, J. Yoon, X. Zhang, H. Wang, Thin Solid Films 516/15 (2008), 5103. Copyright (2008), with permission from Elsevier.

4.2 Introduction

TaN has been demonstrated to be one of the most promising diffusion barrier materials for Cu interconnects, because of its high thermal stability, dense interstitial structure, thickness advantages and low resistivity [73-77]. It has a variety of compositions and crystalline phases, including tetragonal phases (Ta_3N_5 and Ta_4N_5), hexagonal phases (Ta_5N_6, ε-TaN, δ-TaN and γ-Ta_2N close packed), body centered cubic ($TaN_{\sim 0.005}$), [49] and face centered cubic TaN (B1-NaCl) [50]. Among them, the most efficient diffusion barrier with the lowest resistivity is the one with a Ta/N ratio of 1:1 with B1-NaCl structure (a=0.4330 nm) [4]. However it is a metastable phase, and TaN films directly grown on Si are typically the stable hexagonal phases. Although recent work has shown the possibility of depositing cubic TaN (B1-NaCl) on silicon directly by chemical vapor deposition, [15] the use of expensive reactants and the production of toxic wastes make the approach difficult to be implemented. Recently we have demonstrated that epitaxial cubic TaN can be stabilized on Si substrates using a TiN (B1-NaCl, a = 0.424 nm) buffer layer [16, 17] and this configuration has excellent Cu diffusion-barrier properties and lower resistivity compared with most of the polycrystalline TaN reported in the literature. The TiN buffer layer was chosen because of its low resistivity, good lattice match with cubic TaN (~1.8%), reasonably good diffusion barrier property, and most importantly, easy processing by various deposition techniques. However the total thickness of the TaN/TiN stacks reported was in the range of 100 nm or more. This is far beyond the desired diffusion barrier thickness (~8 nm) for the next generation ultra-large scale integration devices as stated in the last update of the International Technology Roadmap for Semiconductor [78].

In this paper, we report that a TiN buffer layer as thin as ~1 nm (1~5 monolayers) serves as an effective seed layer and stabilizes the cubic metastable TaN phase. This work enables the growth of cubic TaN diffusion barrier using any of the deposition techniques currently available for TiN growth in the semiconductor industry. It is commonly accepted that buffer layers play a very important role in the overall quality of thin films, and a minimum buffer thickness of 5-10 nm is usually required to ensure a high quality growth [79-82]. However, we found that the buffer layer thickness (~1 nm - 15 nm) has very little or no obvious effect on the overall growth of epitaxial TaN. The microstructures, growth and nucleation mechanisms, diffusion barrier properties and electrical properties of the bilayer stacks were explored as a function of the thickness of the TiN seed layer.

4.3 Experimental Details

The TiN and the TaN layers were deposited in a multitarget pulsed laser deposition (PLD) system with a KrF excimer laser (Lambda Physik Compex Pro 205, λ= 248 nm, 10 Hz). The laser beam is focused to obtain an energy density of approximately 4 J cm^{-2} at a 45° angle of incidence. The hot-pressed stoichiometric cubic TiN and hexagonal ε-TaN targets were obtained from CERAC Inc. Cleaning of the Si substrates was performed in two steps. The first step involved removing the organic impurities by using a piranha solution with a 3:1 concentration ratio (sulfuric acid (98%)/hydrogen peroxide (30%)). The final step used a buffer oxide etching solution in order to remove the native oxide present on the silicon surface. The substrates were then kept in an inert N_2 atmosphere before being loaded into a vacuum chamber. All the depositions were processed at a base pressure of about 1.0×10^{-5} Pa and a substrate temperature of $700 \pm 10\ ^{\circ}C$. Deposition rates for TiN and TaN were 0.6 Å/s and 0.4 Å/s, respectively. The microstructure of the as-deposited films was characterized by x-ray diffraction (XRD) (BRUKER D8 powder X-ray diffractometer, CuK_{α} radiation operating at 40 kV and 40 mA) and transmission electron microscopy (TEM) (JEOL 2010 analytical microscope, operating at 200 kV with a point-to-point resolution of 0.23 nm). All the TEM samples were prepared by a standard cross-section sample preparation: grinding, polishing and ion milling steps (PIPS 691 precision ion polishing system, 3.5 keV). To study Cu diffusion characteristics in TiN/TaN bilayer stacks, a thin layer of Cu was deposited on top of the bilayers at room temperature by PLD, followed by vacuum annealing (1×10^{-5} Pa) at $500^{o}C$ for 30 minutes. The Cu diffusion characteristics in these TiN/TaN films were studied by cross-sectional TEM. The resistivity of as-deposited bilayer stacks was measured by a four-point probe technique with a Veeco FPP-100 system.

4.4 Results and Discussion

Table 4.1 lists the information about film thickness and the XRD and TEM results for all the samples. The TiN seed layer was varied from 15 nm to 1 nm while keeping the total thickness of the stack below 25 nm. XRD θ~2θ scans of the epitaxial TaN/TiN stacks with TiN thicknesses of 15, 5, 1 and 0 nm are shown in Figure 4.1a. The first scan from the bottom is of a single TaN layer grown directly on Si (001) without the TiN seed layer. Note that the scale for the XRD of TaN without TiN seed layer is much smaller than that of the other samples with TiN seed layer. This is to show the small peaks from the polycrystalline TaN film. The scan only contains the major Si (004) peak and several small peaks from the hexagonal ε-TaN phase. The other three scans are from samples with different TiN thicknesses. For the sample with 15 nm-thick TiN, the diffraction patterns from cubic TiN (002) and TaN (002) are clearly distinguishable, indicating that cubic TaN has grown in a highly textured manner along the <00l> direction. The TiN (002) diffraction peak is centered at $2\theta = 42.88^{o}$. In the other two samples with a 5 nm and a 1 nm of TiN seed layer, only one diffraction peak, with 2θ values corresponding to the cubic TaN (002), is observed. These experiments indicate that cubic TaN, which grows highly textured along the TaN *<00l>* direction on the Si substrate, can be stabilized by a very thin (as thin as 1 nm) TiN seed layer. Furthermore, TaN (002) peaks shift to smaller angles as the TiN thickness decreases as shown in Figure 4.1b. The lattice parameter of cubic TaN calculated from the (002) peak positions is 0.4299 nm, 0.4301 nm and 0.4311 nm, for specimens with a TiN seed layer of 15 nm, 5 nm and 1 nm, respectively. Compared to the bulk lattice parameter for cubic TaN (*a* = 0.4330 nm), the cubic TaN films stabilized by TiN are all in tensile stress in the in-plane direction. However, interestingly, the lattice parameter of the TiN seed layer is *a* = 0.424 nm, which is smaller than that of cubic TaN. Such a difference should lead to a compressive stress in the TaN, and correspondingly, a tensile stress in the TiN seed layer. Possibly the TaN film and the underlying Si substrate play an important role in the TaN stress evolution than the thin TiN buffer layer.

Table 4.1. List of the samples prepared; their respective thicknesses and the characterization technique used for the analysis.

Sample	A	B	C	D	E	F
TaN	~30 nm	8 nm	12 nm	15 nm	18 nm	18 nm
TiN	0 nm	15 nm	10 nm	5 nm	3 nm	1 nm
XRD	1a	1ab		1ab		1ab
TEM		2a		2b		2c

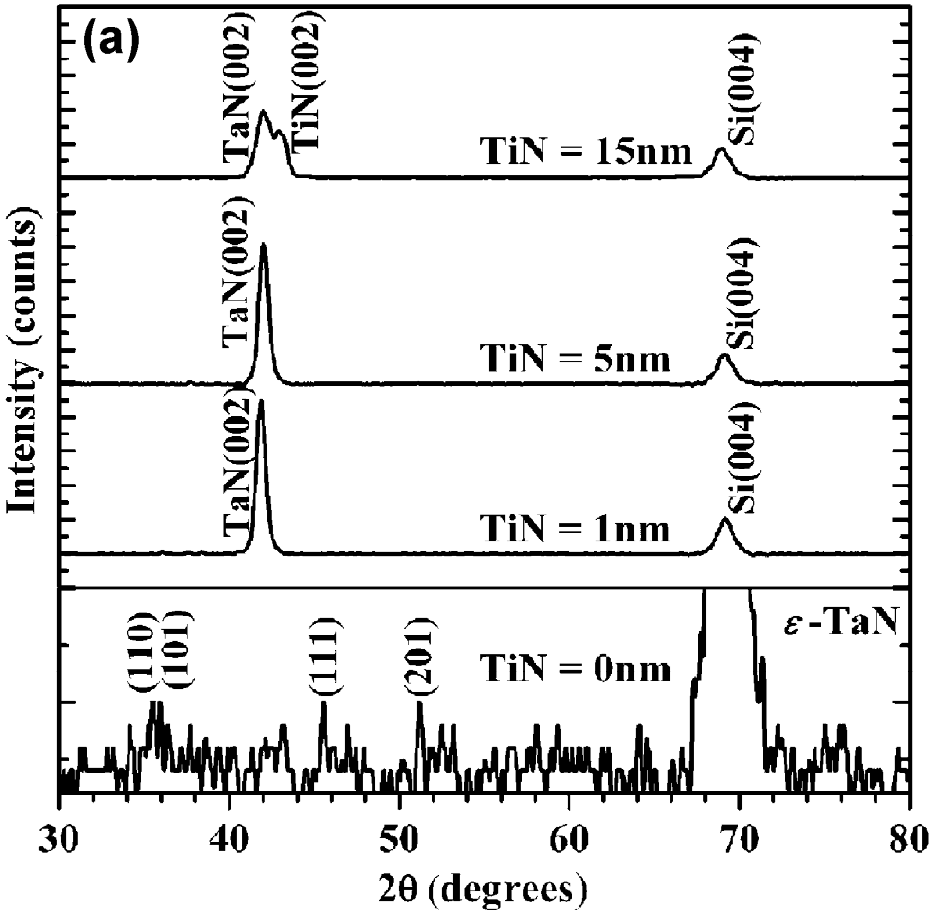

Figure 4.1. XRD θ~2θ scans (intensity vs. 2θ). (a) Full range XRD of the TaN/TiN stacks. Top to bottom: diffraction patterns of the bilayer stacks with TiN seed layer of thicknesses of 15 nm, 5 nm, 1 nm and 0 nm (no seed layer). Note that the scale for the pure TaN sample is smaller than the other TaN films with TiN seed layer. (b) Localized XRD diffraction pattern showing the evolution of the TaN (002) peak and weakening of the TiN (002) peak when the buffer thickness decreases. TaN and TiN are growing highly textured along <*00l*> on Si (001) substrate.

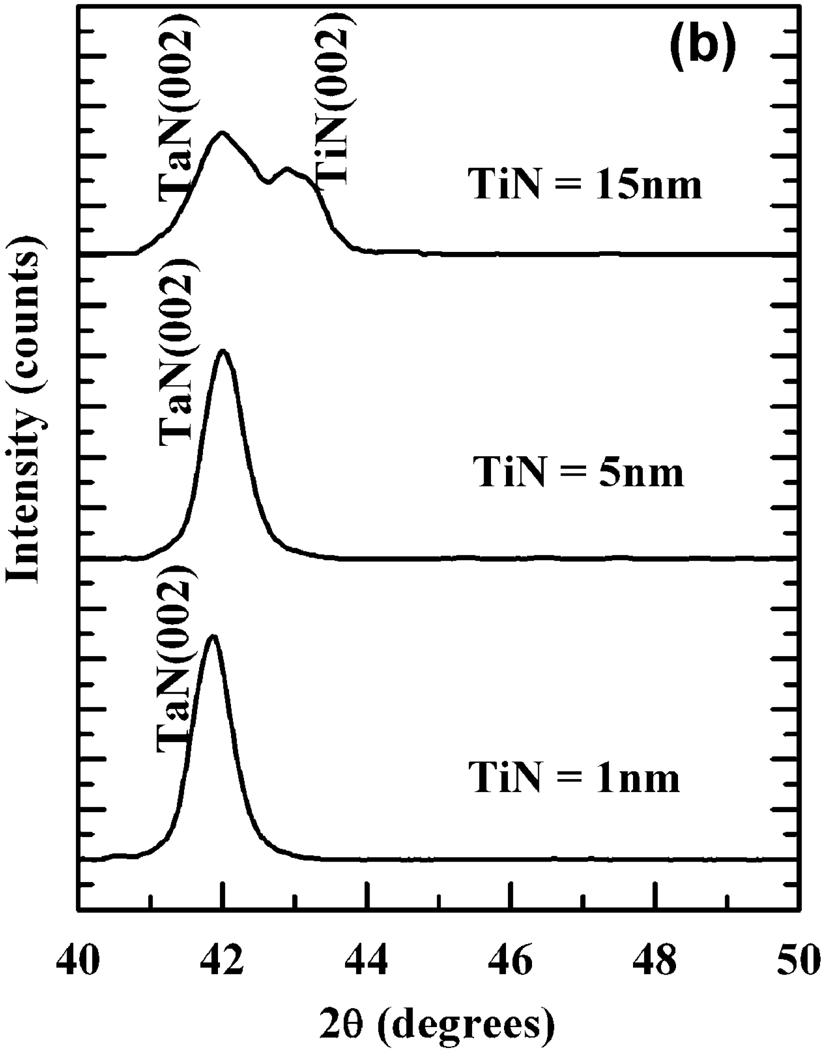

Figure 4.1. Continued.

Low magnification cross-section TEM images of epitaxial TaN/TiN thin stacks on a Si (001) substrate are shown in Figure 4.2a-c. The zone axis for all cases is along Si<110>. For each case, the thickness of TaN was about 9-18 nm while the thickness of the TiN seed layer is approximately 15 nm (2a), 5 nm (2b), and 1 nm (2c). In all cases, the total film thickness (TaN + TiN) is less than 25 nm. TEM micrographs indicate that TiN and TaN have grown uniformly over a large area in all specimens. The TiN/Si and TaN/TiN interfaces are clear and free of intermixing. The corresponding selected-area-diffraction (SAD) pattern for each specimen is shown as an insert in each TEM micrograph. TaN/TiN has single-crystal-like diffraction patterns showing the <110> diffraction zone in all three cases. It is difficult to distinguish between the diffractions from TiN (002) and TaN (002) due to their small lattice mismatch (mismatch <1.8%). It is conceivable that, for the specimen TaN(18 nm)/TiN(~1 nm), the majority of the (002) diffraction intensity is contributed by TaN. The epitaxial TaN/TiN thin stacks were grown on Si through the mechanisms of domain matching epitaxy between TiN and Si (mismatch of 24%) [83] and lattice matching epitaxy between TaN and TiN. The epitaxial relations are determined to be TaN <110> // TiN <110> // Si <110> and TaN (002) // TiN (002) // Si (004) with a cube-on-cube orientation relationship.

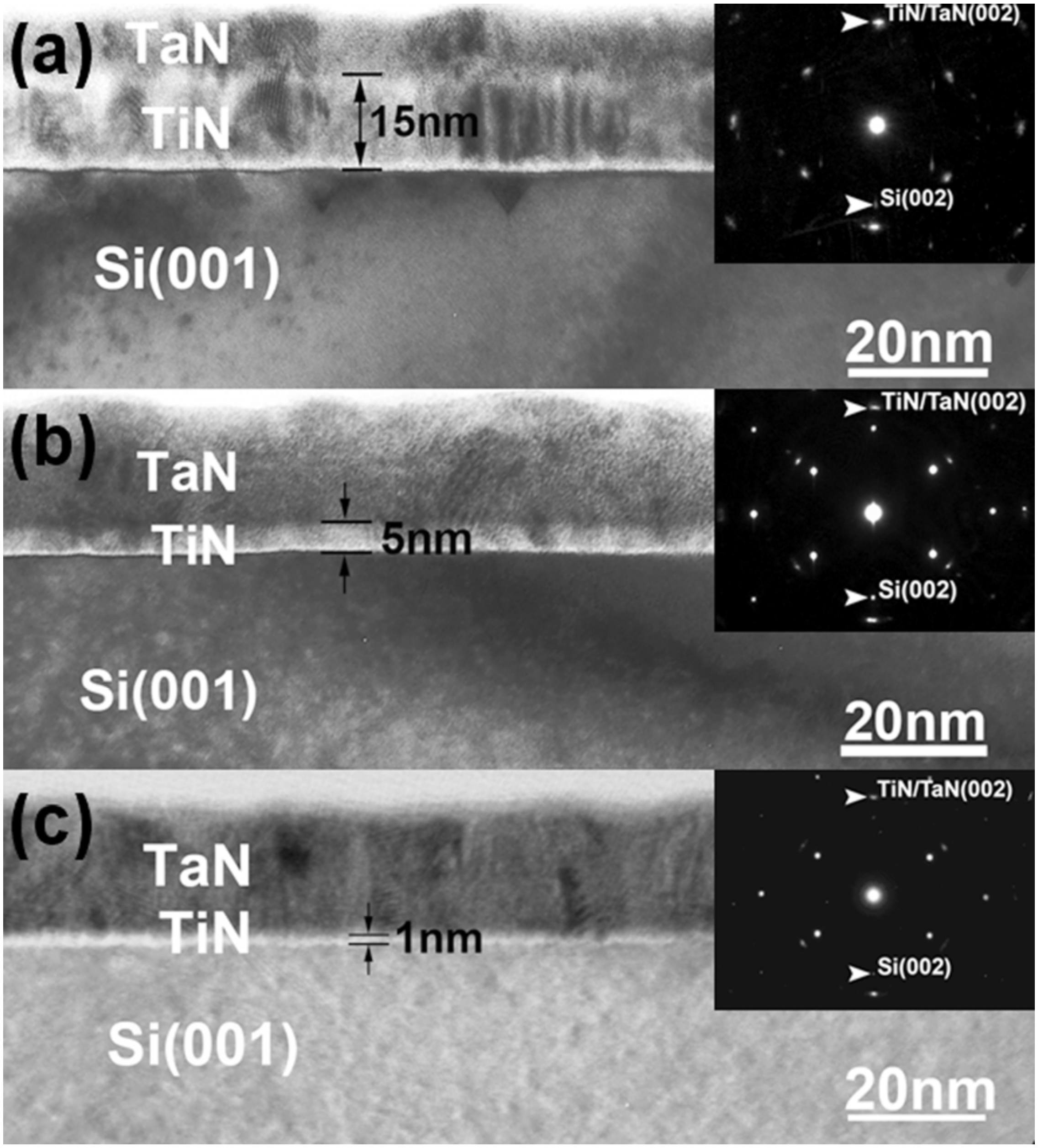

Figure 4.2. Low magnification cross-section TEM images of the TaN/TiN stacks deposited on Si(100) with (a) 15 nm, (b) 5 nm, and (c) 1 nm TiN seed layer. The images show that uniform layers structures have formed without any interlayer mixing for all cases. The corresponding SAD patterns for a-c clearly show the epitaxial growth of TaN/TiN stacks on Si (100).

In order to reveal the nature of the TaN/TiN interface of the specimen TaN(18 nm)/TiN(~1 nm), cross-section high resolution TEM was conducted and the image is shown in Figure 4.3. Instead of a continuous layer, the TiN seed layer is observed to be non-uniform with the film thickness ranging from 0 to about 2 nm (marked as dashed line). The average TiN film thickness over a large view area is less than 1 nm. On top of the non-uniform TiN seed layer, the epitaxial growth of cubic metastable phase of TaN is clearly observed from the well aligned {111} lattice planes. It is surprising that a TiN layer with 1-5 monolayers is sufficient to serve as a template for the subsequent growth of cubic metastable TaN. The buffer layer approach has been widely used to process semiconductor thin films, such as an AlN buffer layer for InN and GaN grown on sapphire and Si substrates, [80, 81] a SiC buffer layer for GaN growth on Si substrate, [82] and a Si buffer layer for GaAs grown on a Si substrate [79]. In most cases, a flat and continuous buffer film is needed to ensure complete surface coverage and high overall film quality [79-82]. However our observation suggests that a uniform surface coverage might not be necessary if sufficient nucleation sites have been provided for the nucleation of the metastable cubic TaN phase. Further experiments will be carried out at the authors' laboratory to study the growth mode of the TiN and TaN layers (i.e., 2D, 3D or 2D+3D). This ultra-thin seed layer approach can be applied to grow cubic metastable TaN (B1-NaCl) using any currently available deposition techniques for TiN growth in

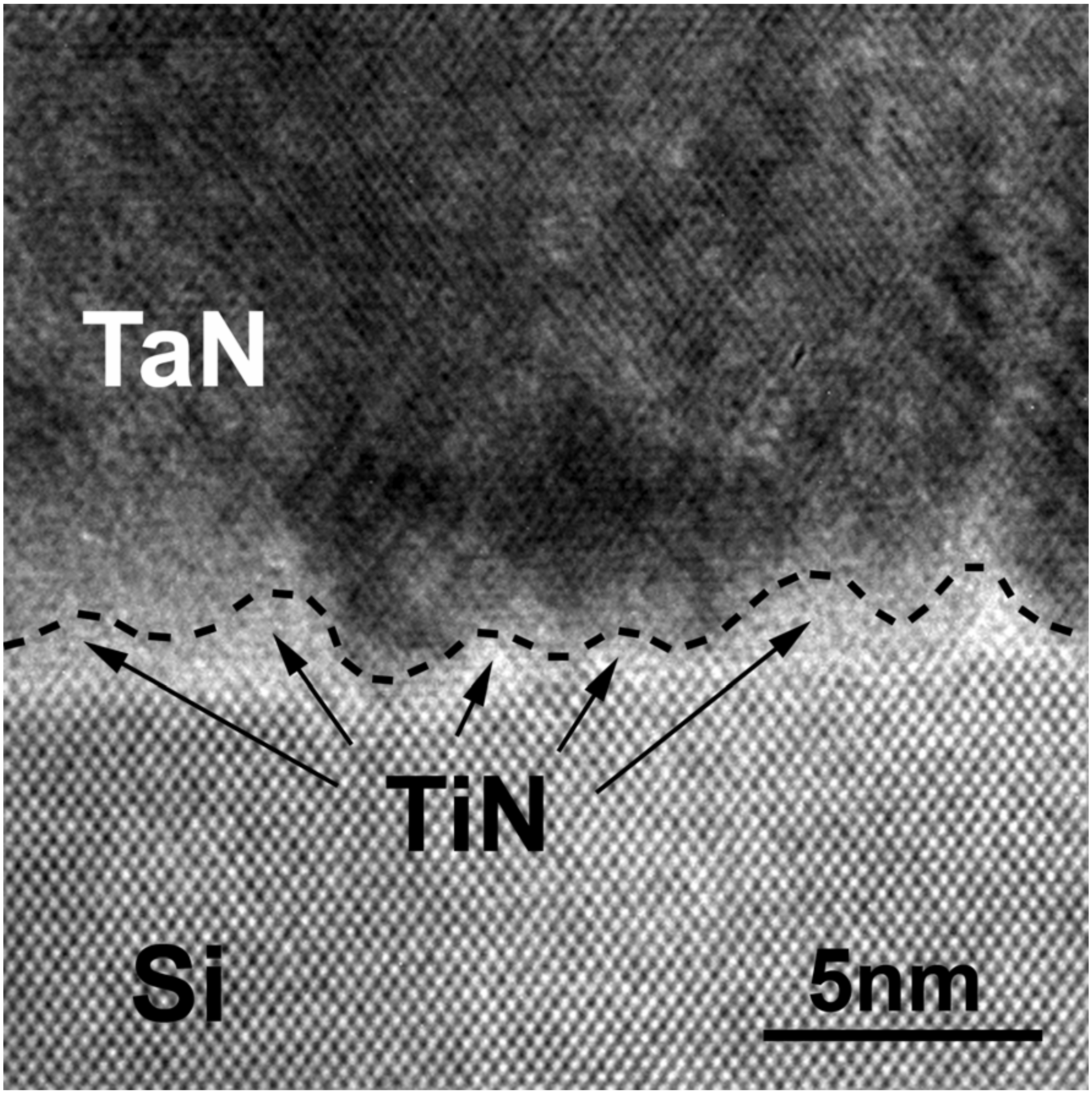

Figure 4.3. High resolution cross-section TEM image of the TaN(18 nm)/TiN(~1 nm) stack shows a non-uniform TiN seed layer which provides enough nucleation sites for the growth of high quality epitaxial cubic metastable TaN. The seed layer marked using dashed lines has a thickness ranging from 1 monolayer to 5 monolayers.

the semiconductor industry. The proposed concept could also be applicable to other systems where the film thickness limitation is an important consideration.

Preliminary Cu diffusion barrier studies were carried out on all TiN/TaN bilayers. Figure 4.4 shows the low magnification cross-section TEM images of the Cu/TaN(18 nm)/TiN(~1 nm), as-deposited (4a) and vacuum annealed at 500°C for 30mins (4b). No obvious Cu diffusion is observed in the cubic TaN thin layer (Figure 4.4b). The cube-on-cube epitaxial relationship between TaN and Si is essentially unchanged after annealing by comparing the SAD patterns in 4a and 4b. These studies suggest that the metastable cubic TaN phase stabilized by the ultra-thin TiN seed layers exhibits excellent thermal stability upon annealing at temperatures up to 500°C. Finally, the electrical resistivity for all TiN/TaN (cubic) thin stacks is ~ 400 μΩ-cm which is much lower than that of TaN alone (hexagonal phase grown directly on Si), ~ 1300 μΩ-cm.

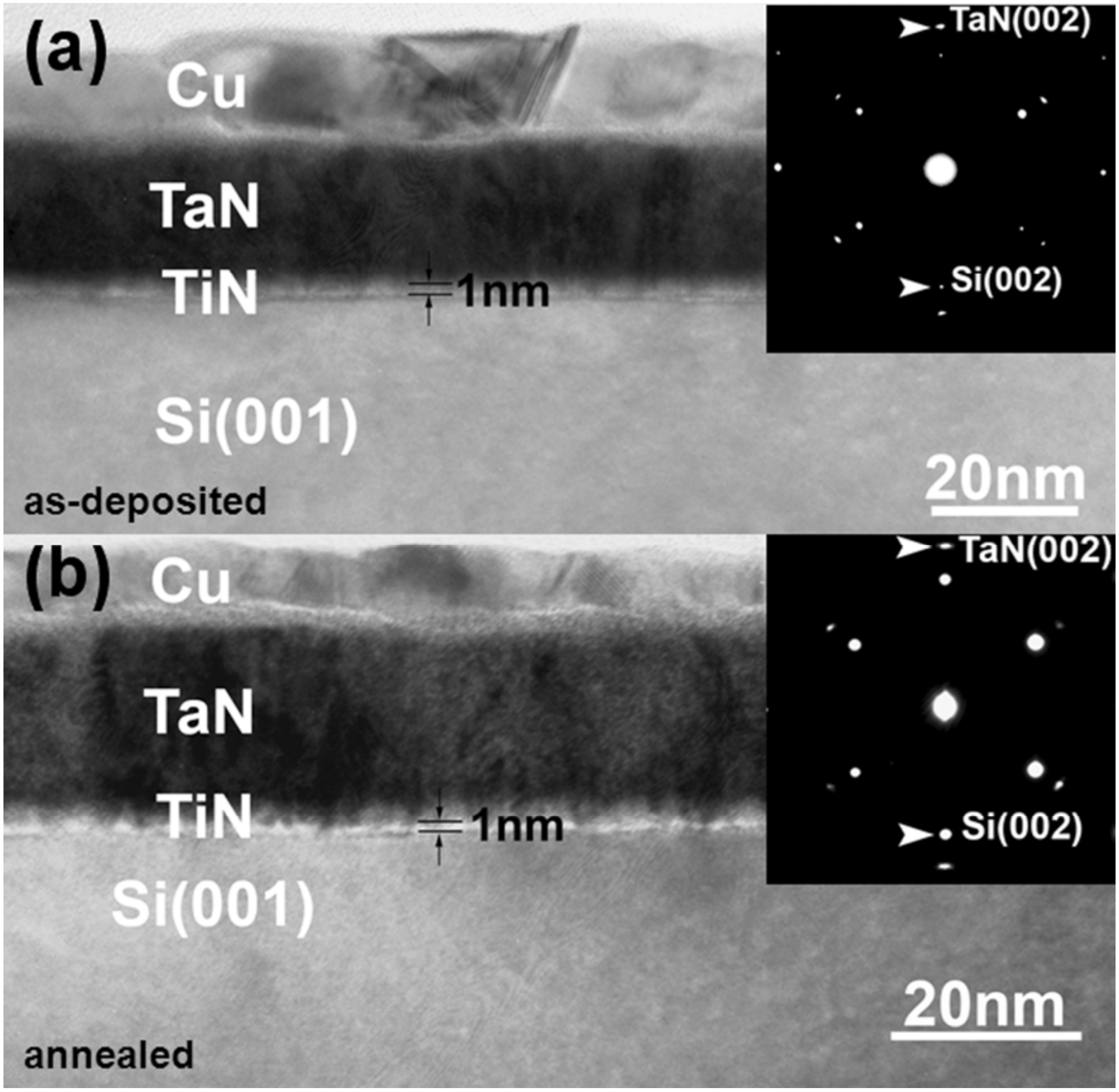

Figure 4.4. Cross section TEM images of the stack of Cu/TaN(18 nm)/TiN(1 nm)/Si(001) (a) as-deposited and (b) post-annealed at 500^{o}C for 30 minutes. The corresponding SAD pattern inserted in (b) shows that the cube-on-cube structure is maintained and no obvious Cu diffusion is observed in the TaN layer after annealing.

4.5 Summary

We have demonstrated that an ultra-thin TiN seed layer, as thin as ~1 nm, can stabilize the epitaxial metastable cubic TaN films. Both XRD and cross-section TEM characterizations clearly show that cubic TaN with preferred (*00l*) orientation on Si (001) substrates has been established by TiN seed layers with thickness ranging from 15nm to 1 nm. The high quality epitaxial growth, low resistivity, good thermal stability and excellent Cu diffusion barrier property of the TaN/TiN bilayers demonstrate a strong potential for their application as diffusion barriers for Cu interconnects.

CHAPTER V

CUBIC HFN THIN FILMS WITH LOW RESISTIVITY ON SI (001) AND MGO (001) SUBSTRATES*

5.1 Overview

We have deposited epitaxial and highly textured cubic HfN (B1-NaCl) thin films on single crystal MgO (001) and Si (001) substrates, respectively, using a pulsed laser deposition technique. The HfN thin films are around 100 nm thick. Detailed microstructural characterizations include X-ray diffraction, transmission electron microscopy (TEM) and high resolution TEM. Low resistivity as low as 40 μΩ-cm were observed by standard four point probe measurements. Its low resistivity and good diffusion barrier property demonstrated by our preliminary Cu-diffusion tests for HfN on Si suggest that HfN could be a promising candidate for diffusion barrier for Cu interconnects.

---

*Reprinted from "Cubic HfN Thin Films with Low Resistivity on Si (001) and MgO (001) Substrates" by R.A. Araujo, X. Zhang, H. Wang, J. Electron. Mater., (2008), in press. Copyright (2008), with kind permission of Springer Science and Business Media.

5.2 Introduction

Next generation of ultra-large scale integration (ULSI) devices requires high efficiency diffusion barrier materials for copper interconnects with outstanding physical properties, which include: low resistivity, high thermal stability, relatively dense interstitial structure, process compatibility with the IC industry and thickness fulfillment as stated by the International Technology Roadmap for Semiconductor (ITRS) [19]. The materials that meet those requirements have been so far TiN, TaN [15, 17, 84] or their alloys, [18, 85] plus few other candidates from the same family known as transition metal nitrides [1, 4]. Within the transition metal nitrides, HfN has attracted research interests worldwide, because of its known outstanding physical and chemical properties, such as high thermal stability (T_m = 3380 °C) and relatively low bulk resistivity (ρ = ~33 μΩ-cm) [1]. Processing efforts of HfN thin films have been mostly reported as polycrystalline quality by reactive sputtering, chemical vapor deposition, and atomic layer deposition [51-53, 86]. It has been reported that, generally, epitaxial thin film barriers show better Cu diffusion barrier properties and lower resistivity than their polycrystalline counterparts due to less defective regions (e.g., grain boundaries) in their structures [4]. In addition, based on previous literature reports, the material properties of HfN vary dramatically as its stoichiometry changes. The reported resistivity of stoichiometric HfN thin films (1:1 ratio) is mostly greater than 100 μΩ-cm, while the non-stoichiometric, HfN_x ($x>1$), can be an insulator [51] or semiconductor [87, 88]. Further more, the lattice parameter, processing condition and diffusion barrier properties also vary as the stoichiometry of the thin film changes. Therefore it is important to process stoichiometric HfN thin films with epitaxial quality as model systems to explore the electrical, growth, and diffusion barrier characteristics of HfN.

In this paper, we report our recent effort on the growth of high quality epitaxial and highly textured cubic HfN (B1-NaCl structure) on single crystal MgO substrates and Si substrates, respectively, all deposited by pulsed laser deposition (PLD). The advantage of PLD is that the target stoichiometry can be reproduced in the deposited film with no or very little contamination. In our work, a 1:1 ratio HfN target was used. Low resistivity (~40 μΩ-cm) HfN deposited on Si substrates, comparable to that reported by Shinkai et al. [89] and much lower than other reports (>100 μΩ-cm) [51-54, 86, 90] is presented in this paper.

5.3 Experimental Details

The depositions of HfN were performed in a multitarget chamber with a KrF excimer laser (Lambda Physik Compex Pro 205, λ= 248 nm, 10 Hz). The laser beam was focused to obtain an energy density of approximately 10 $J\cdot cm^{-2}$ at 45° angle of incidence. The target is a hot-pressed stoichiometric polycrystalline HfN obtained from Plasmaterials, Inc.. Single crystal MgO (001) (insulator) and silicon (001) substrates with relatively high electrical resistivity (10 Ω-cm) were used in this work. Preparation of the silicon substrate surface was performed in two steps. The first step involved removing the organic impurities by using an oxidating piranha solution with a 3:1 concentration ratio (sulfuric acid (98%)/hydrogen peroxide (30%)). The final step used a buffer oxide etching (BOE) solution in order to remove the native oxide present on the silicon surface. The substrates were then kept in an inert N_2 atmosphere before being loaded into a vacuum chamber. The MgO substrates were directly loaded for deposition without surface cleaning. All of the depositions were carried out at a base pressure of about 1×10^{-5} Pa and at a substrate temperature of 700 ± 10 ^{o}C. The deposition rate of HfN was of about 5 Å/s. The microstructure of the as-deposited films was characterized by X-ray diffraction (XRD, BRUKER D8 powder X-ray diffractometer) and transmission electron microscopy (TEM) (JEOL 2010 analytical microscope with a point-to-point resolution of 0.23 nm). The resistivity of the as-deposited HfN films was measured using a four-point probe system (FPP) (Veeco FPP-100).

5.4 Results and Discussion

Initial XRD scans (θ~2θ) of HfN thin films on MgO (001) and Si (001) are shown in Figure 5.1(a) and (b), respectively. For the stack of HfN/MgO (001) (Fig. 1(a)), the strong peaks are centered at 39.48° and 42.92°, indexed as HfN (002) and MgO (002), respectively. The HfN (002) peak is aligned to the MgO (002) and no other orientations were observed. It suggests that the HfN film has grown on MgO highly textured along (00*l*). The calculated *d*-spacing for the substrate MgO (002) and HfN (002) is 0.2105 nm and 0.2281 nm, respectively. The calculated lattice parameters for the substrate MgO and the HfN film are 0.421 nm and 0.456 nm, respectively, which gives a lattice mismatch of about 8.025%. The θ~2θ scan of the HfN/Si (001) stack in Fig. 1(b) shows the indexed peaks of HfN (111), HfN (002) and Si (004), centered at 34.12°, 39.58° and 69.16°, respectively. Based on the peak intensity, it is clear that the majority of the HfN film on Si has a preferred (00*l*) growth orientation and only a small percentage of grains aligned in the (111) orientation. The calculated *d*-spacing for HfN (111), HfN (002) and Si (004) is 0.2625 nm, 0.2274 nm and 0.1357 nm, respectively. The calculated lattice parameter for the HfN thin film is 0.4546 nm, which is slightly smaller than that of HfN films on MgO substrates. According to these results the lattice mismatch between the HfN film and Si substrate is calculated to be about 17.7%.

Low magnification cross-section TEM images of the stacks of HfN/MgO (001) (from MgO <010> zone) and HfN/Si (001) (from Si <110> zone) are shown in Figure 5.2(a) and (b), respectively. Both images cover a large area of the samples. The thickness of the HfN thin film on MgO (001) and on Si (001) is about 150 nm and 130 nm, respectively. The corresponding selected-area-electron-diffraction (SAED) patterns from the view areas of both samples are shown as inserts in Figure 5.2. For the HfN on MgO (001) (Fig. 2(a)), the single-crystal-like diffractions from the HfN film are well aligned with the diffractions from MgO, which suggests a typical cube-on-cube growth for HfN on MgO. The epitaxial relationships are determined to be HfN <010> // MgO <010>, HfN (002) // MgO (002) and HfN (200) // MgO (200). The diffraction spots of HfN (002) and MgO (002) are well separated and easy to distinguish because of the relatively large lattice mismatch of ~ 8%. The lattice parameter of HfN on MgO (001) is

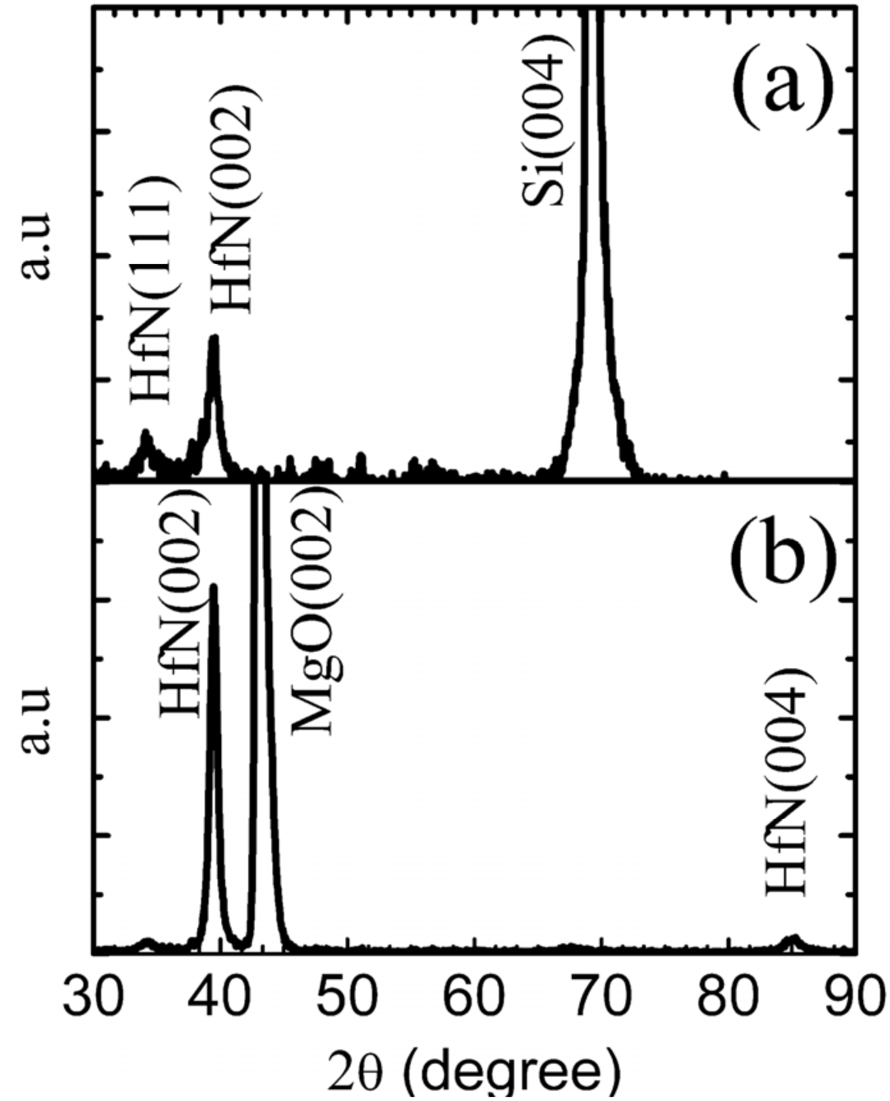

Figure 5.1. X-ray diffraction pattern (θ~2θ scan) for (a) HfN on MgO (001) substrate showing the peak HfN (002) and (b) HfN on Si (001) substrate with a predominant HfN (002) peak and a small HfN (111) peak.

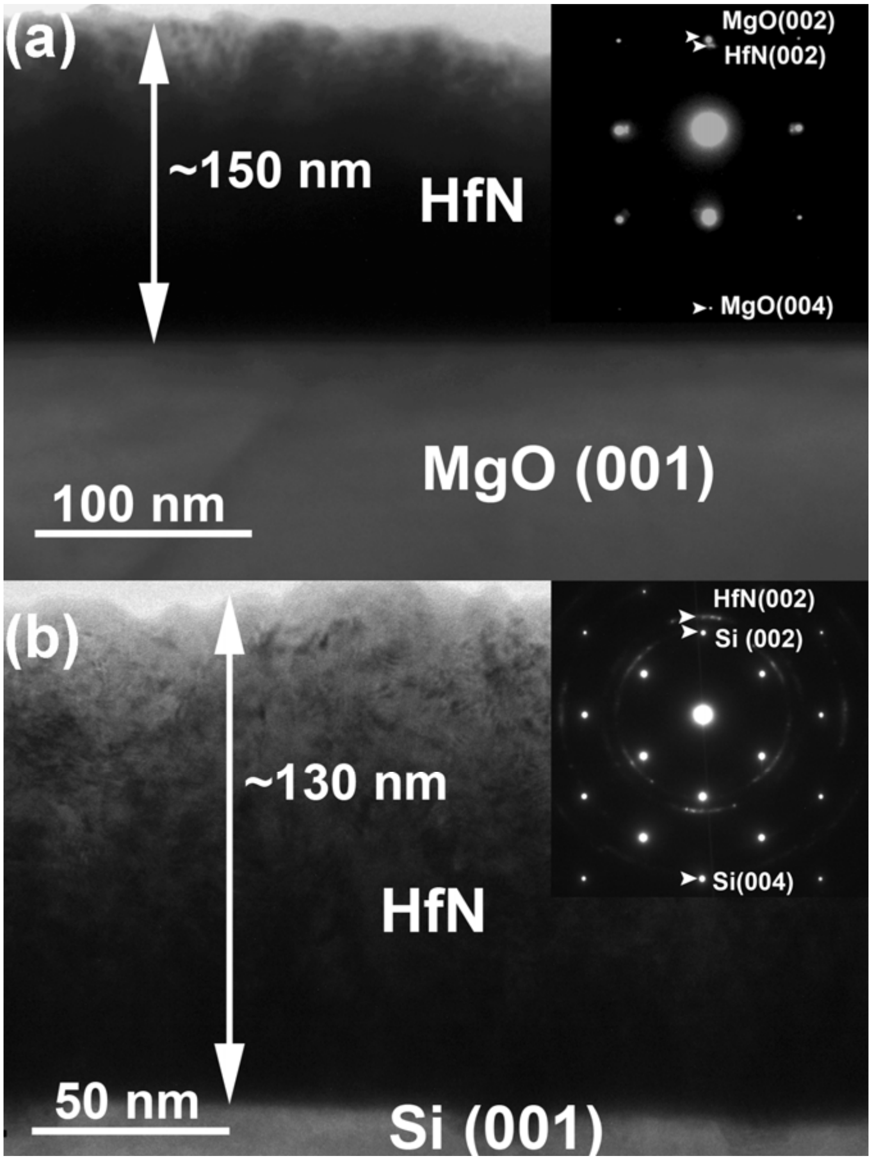

Figure 5.2. (a) Low magnification cross-section TEM image of HfN on MgO (001) substrate from the <010> zone. The insert is the corresponding SAED pattern. A clear cube-on-cube growth orientation is observed from the SAED pattern. (b) Low magnification cross-section TEM image of HfN on Si (001) substrate from the <110> zone. The insert is the corresponding SAED pattern.

determined to be 0.455 nm based on the SAED pattern, which is very close to the value calculated from XRD data. Similarly, the HfN on Si (001) (Fig. 2(b)) shows single-crystal-like diffractions with some small arc. In this view area, no diffraction from HfN (111) oriented grains was observed. It suggests that the majority of the HfN film on Si has grown as cube-on-cube, similar to the case of HfN on MgO. However the epitaxial quality of the HfN on Si is not as high as that of HfN on MgO. This is mainly due to the large lattice mismatch between the HfN and Si substrate (~17.7%). The large lattice mismatch between HfN and Si might be the main reason for the nucleation of the (111) oriented grains which can probably relieve some of the mismatch strain.

A high resolution cross-section TEM image of the interface between HfN and Si (001) from the Si<110> zone is shown in Figure 5.3. At this typical interface area, it clearly shows the epitaxial growth of the HfN film on Si (001) with a clean interface. The {111} lattice planes of HfN and Si are marked by straight lines. Over the major part of the interface area, the {111} lattice planes of HfN and Si aligns very well with each other. In one of the small HfN grain, the HfN {111} planes are slightly tilted, 7° in the view area, with respect to the Si {111} planes (marked in Figure 5.3). The small-angle tilt between the HfN grains might be another way for relieving the large mismatch strain between HfN and Si.

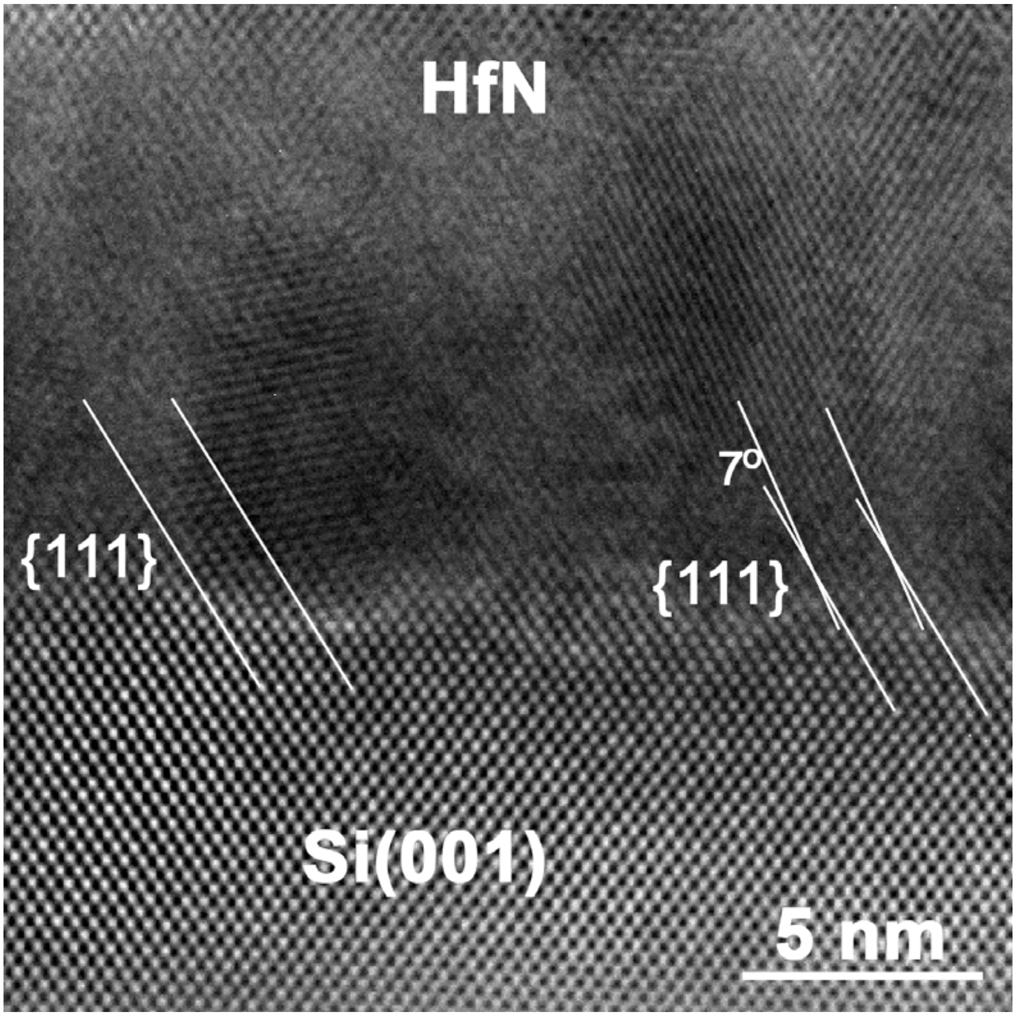

Figure 5.3. High resolution TEM image of the <110> cross-section sample at the interface HfN/Si (001). A small part of the HfN thin layer has a slightly misaligned {111} planes with respect to the Si {111} planes.

The successful growth of epitaxial and highly textured HfN thin films on Si can be attributed to the deposition technique, PLD, as well as the deposition conditions. The main advantage of the PLD technique is that it reproduces the target stoichiometry with very little contamination, and deposits species with high kinetic energy [83]. Another important consideration is the lattice matching between the film and the substrate. Further studies on improving the epitaxial quality of HfN deposited on silicon substrates is on going in our research lab. An effective approach that we have recently demonstrated is to apply a thin buffer layer before the HfN deposition [91].

The electrical resistivity of the HfN films, measured by FPP technique, ranges from 38 to 52 μΩ-cm, with an average value of about 45 μΩ-cm (Figure 5.4). This low resistivity is comparable to the results reported by Shinkai *et al.* [89] and much lower than other reported values (> 100 μΩ-cm) [52, 53, 90]. We also conducted a preliminary Cu diffusion test in these samples by depositing a thin layer of Cu on top of the HfN at room temperature by PLD, followed by a vacuum annealing (1×10^{-5} Pa) at 500°C for 30 minutes. After the annealing, there was no obvious Cu diffusion observed at the Cu/HfN interface, within the HfN film and in the underlying Si substrate.

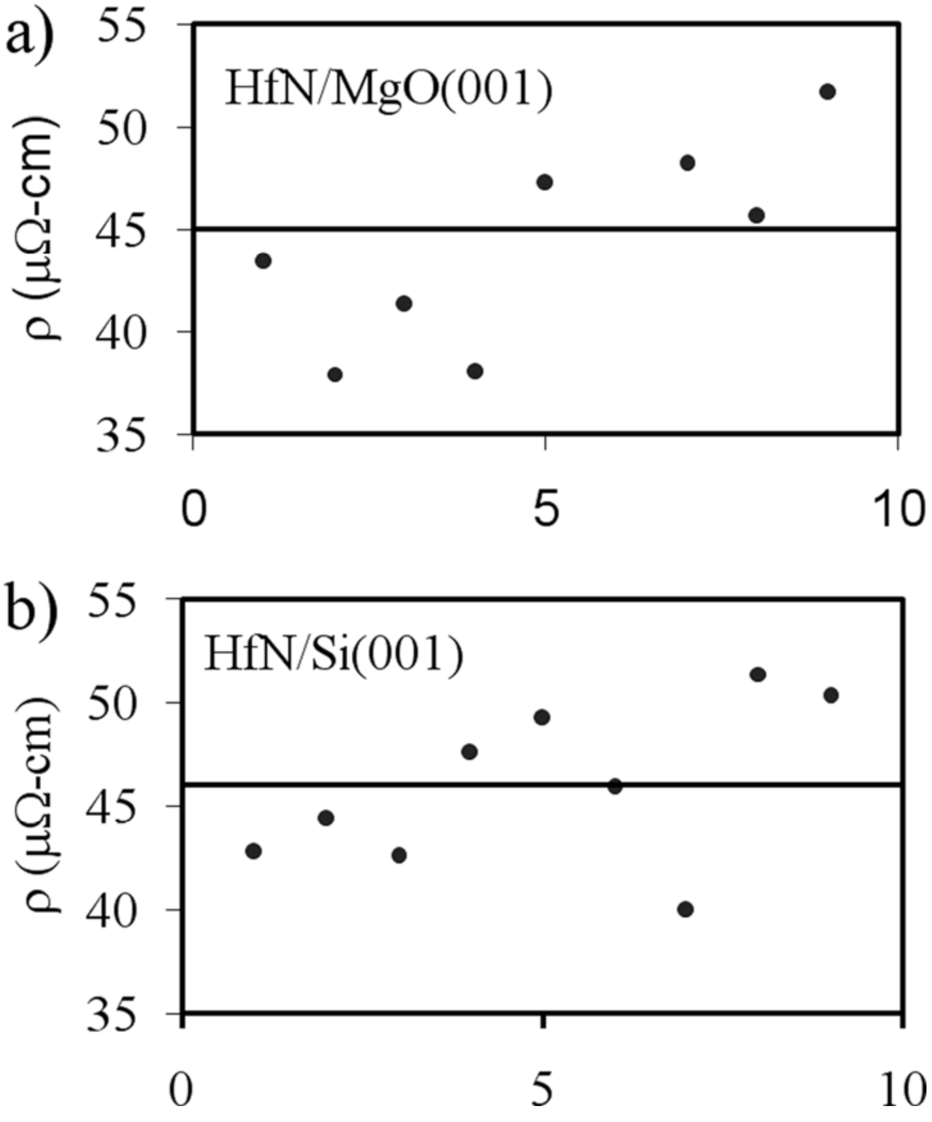

Figure 5.4. Electrical resistivity measurements of samples (a) HfN deposited on MgO (001) and (b) HfN deposited on Si (001) substrates.

5.5 Summary

High quality epitaxial and highly textured HfN films have been deposited on MgO and Si substrates, respectively, by PLD. Both XRD and TEM results suggest that HfN has grown on both MgO and Si substrates with a cube-on-cube orientation relationship. The epitaxial quality of HfN on MgO is much higher than that of HfN on Si, which is mainly due to that the large lattice mismatch between HfN and Si (~17.7%) and the relatively small mismatch of HfN on MgO (~8%). The HfN films on both MgO and Si substrates show low electrical resistivity (~ 45 μΩ-cm) and good diffusion barrier properties based on preliminary annealing experiments. These results suggest that HfN is a promising candidate as diffusion barriers for Cu interconnects.

CHAPTER VI

EPITAXIAL CUBIC HFN DIFFUSION BARRIERS FOR COPPER INTERCONNECTS USING A TIN BUFFER LAYER*

6.1 Overview

Cubic HfN (B1-NaCl) thin films were grown epitaxially on Si(001) substrates by using a TiN (B1-NaCl) buffer layer as thin as ~10 nm. The HfN/TiN stacks were deposited by pulsed laser deposition with an overall thickness below 60 nm. Detailed microstructural characterizations include X-ray diffraction, transmission electron microscopy (TEM), and high resolution TEM. Additionally, the electrical resistivity measured by four point probe is as low as 70 μΩ-cm at room temperature. The preliminary Cu diffusion tests show a good diffusion barrier property with a diffusion depth ($2\sqrt{D\tau}$) of 2~3 nm after annealing at 500°C for 30 minutes in vacuum.

---

*Reprinted with permission from "Epitaxial cubic HfN diffusion barriers deposited on Si (001) by using a TiN buffer layer" by R.A. Araujo, X. Zhang, H. Wang, J. Vac. Sci. Technol. B, (2008), in press. Copyright 2008, American Vacuum Society.

6.2 Introduction

HfN is a promising candidate as diffusion barriers for copper metallization, because of its outstanding physical properties such as high thermal stability (melting temperature = 3380 ºC), relatively dense structure, high hardness, and low electrical resistivity [1, 52-54, 86, 92]. Therefore the use of HfN as the diffusion barrier in the next generation Ultra-large scale integrated (ULSI) devices by satisfying the International technology Roadmap for Semiconductor is a possibility [19]. One of the major advantages of HfN over the extensively reported TaN [15, 17, 18, 85] is its low bulk resistivity of ~33 μΩ-cm [1] compared to that of TaN of ~200 μΩ-cm for bulk and thin films [1, 15, 17, 18], which is an important requirement for next generation diffusion barrier materials. Additionally, HfN presents a stable cubic B1-NaCl phase while the TaN cubic B1-NaCl structure is metastable [1, 49]. Recently, it has been reported that HfN grows on silicon substrates mainly as polycrystalline thin films by reactive sputtering and atomic layer deposition [51, 54, 87, 88], while its epitaxial thin film form was reported to be grown on MgO substrates [92]. Epitaxial thin film barriers usually present better Cu diffusion barrier properties and lower resistivity than their polycrystalline counterparts due to fewer defects (especially grain boundaries) in their structures [4, 84]. It is worth to note that, the physical properties of HfN vary significantly as the stoichiometry of HfN changes. For example, the reported resistivity of stoichiometric HfN (1:1 ratio) thin films growth on silicon substrates is greater than 100 μΩ-cm, while a non-stoichiometric HfN_x (x>1) could be an insulator [51] or semiconductor [52-54, 87, 88]. Besides its electrical property, the lattice parameter, processing conditions and diffusion barrier properties also vary as the stoichiometry changes, since more content of N creates more defects [90]. Therefore it is important to process stoichiometric HfN thin films with high epitaxial quality as model systems to explore the electrical, growth, and diffusion barrier characteristics of HfN.

In this paper, we report our effort on the growth and characterization of epitaxial cubic HfN (B1-NaCl structure) on Si(001) substrates by the means of using a thin TiN buffer layer, 10 ~ 40 nm. The reasons of selecting TiN as the buffer layer, include, (1) TiN (a=0.424 nm) can grow epitaxially on Si substrate through domain matching epitaxy and has reasonably good lattice match with cubic HfN (a=0.452 nm), (2) TiN is also tested to be an efficient diffusion barrier, and (3) TiN has low resistivity (~25 μΩ-cm) [1, 83]. Our results suggest that the thin TiN buffer layer not only facilitates the growth of cubic HfN but also prevents the potential interface interaction between the HfN film and the underlying Si substrate.

6.3 Experimental Details

The depositions of the TiN and the HfN layers were performed in a multitarget pulsed laser deposition (PLD) system with a KrF excimer laser (Lambda Physik Compex Pro 205, λ= 248 nm, 10 Hz). The laser beam was focused to obtain an energy density of approximately 10 $J\cdot cm^{-2}$ at a 45° angle of incidence. The hot-pressed stoichiometric TiN and HfN targets were obtained from CERAC Inc. and Plasmaterials Inc., respectively.

The substrates used were Si(001) with a resistivity value in the range of 10-20 Ω-cm. The substrate surface preparation involved a two-step cleaning; the first step is removing the organic impurities and oxidation of the Si surface by using a piranha solution with a 3:1 concentration ratio (sulfuric acid (98%)/hydrogen peroxide (30%)), and the final step used a buffer oxide etching solution in order to remove the native oxide present on the silicon surface. The substrates were then kept in an inert N_2 atmosphere before being loaded into a vacuum chamber. All the depositions were processed at a base pressure of about 1×10^{-7} torr and a substrate temperature of $700 \pm 10\ ^{o}C$. Deposition rates for TiN and HfN were of 4 Å/s and 3 Å/s, respectively. The microstructure of the as-deposited films was characterized by X-ray diffraction (XRD) (BRUKER D8 powder X-ray diffractometer, CuK_{α} radiation operating at 40 kV and 40 mA), and transmission electron microscopy (TEM) (JEOL 2010 analytical microscope with a point-to-point resolution of 0.23 nm). TEM samples were prepared through a standard cross-section preparation procedure: grinding, polishing and ion milling (precision ion polishing system (PIPS691), 3.5 keV). To study the Cu diffusion characteristics in the HfN/TiN stacks, a thin layer of Cu (~60 nm) was deposited on top of the bilayers at room temperature by PLD, followed by vacuum annealing (1×10^{-7} torr) at $500^{o}C$ for 30 minutes. The Cu diffusion characteristics in these HfN/TiN films were studied by cross-sectional TEM. The resistivity of as-deposited bilayer stacks was measured by a four-point probe using a Veeco FPP-100 system.

6.4 Results and Discussion

The HfN/TiN stacks were processed by systematically reducing the deposition time of the TiN buffer layer while keeping the deposition time of the HfN layer constant; i.e. systematically reducing the thickness of the TiN layer and keeping the thickness of the HfN layer constant. The bilayer stacks prepared are listed in Table 6.1 and are: sample A - HfN(20 nm)/TiN(40 nm), B - HfN(20 nm)/TiN(20 nm), C - HfN(20 nm)/TiN(10 nm) and D - single layer HfN (20 nm). Figure 6.1 corresponds to local XRD θ~2θ scans (intensity vs. 2θ) of the HfN/TiN stacks on Si(001) substrates (A-C) and the single HfN layer on Si substrate (D). The two peaks identified in A-C are TiN(002) and HfN(002). The XRD scans, top to bottom, corresponds to the samples A, B, C and D with thicknesses of the TiN buffer layer 40 nm , 20 nm, 10 nm, and 0 nm respectively; while the thickness of the HfN film is kept constant around 20 nm for all cases. For the first sample, A - HfN(20 nm)/TiN(40 nm), the scan clearly shows the peaks for TiN(002) and HfN(002), indicating that cubic HfN has growth on a highly textured fashion along the <00l> direction. As the TiN thickness decreases from sample A to C, the TiN(002) peak intensity decreases due to its thickness reduction. Nevertheless the HfN(002) peak intensity is about the same through A-C suggesting that the HfN films on TiN buffered Si substrates are highly textured along (00*l*). However the pure HfN, sample D, shows clearly two preferred orientations (002) and (111), which suggests a polycrystalline nature of the thin film. The corresponding 2θ angles of the TiN(002) and HfN(002) peaks for samples A-C are listed in Table 6.1. The calculated lattice parameters, in-plane

($a_{//}$) and out-of-plane ($a_{\perp}$) lattice parameters are also listed. For the TiN seed layer, as its thickness decreases from sample A to C, the out-of-plane ($a_{\perp}$) lattice parameter increases and the in-plane lattice parameter ($a_{//}$) decreases. The in-plane lattice parameter ($a_{//}$) for all stacks is smaller than the bulk lattice parameter of TiN (4.24 Å). It suggests that the films are under a compressive stress in the in-plane direction. On the other hand the HfN calculated lattice parameter varies with constant film thickness (~20 nm), which could be mainly due to the effect of the underlying TiN seed layer and the Si(001) substrate. Initially the in-plane lattice parameter ($a_{//}$) reduces from 4.492 Å to 4.486 Å for samples A - HfN(20 nm)/TiN(40 nm) and B - HfN(20 nm)/TiN(20 nm), and then increases to 4.489 Å for sample C – HfN(20 nm)/TiN(10 nm). This suggests that the compressive strain introduced by the underlying TiN film is getting weaker when the TiN layer is about 10 nm and the tensile strain from Si substrate becomes more dominant.

Low magnification <110> cross-section TEM images of the thin film bilayer stacks HfN/TiN deposited on Si(001) substrates are shown in Figure 6.2 for samples A - HfN(20 nm)/TiN(40 nm) and C - HfN(20 nm)/TiN(10 nm). The bilayer stacks shows a total thickness below 60 nm, while the thickness of the TiN seed layer is approximately 40 nm, and 10 nm. It is very clear that the interfaces of HfN/TiN and TiN/Si are sharp and uniform without any obvious interlayer mixing over a large area. This indicates that the thin TiN layer effectively prevent the intermixing between the HfN and Si layer that was observed in our previous work on pure HfN directly grown on Si substrate. The epitaxial quality of the thin films deposited on the Si(001) substrate can be identified from the corresponding selected-area-diffraction (SAD) pattern of each specimen shown

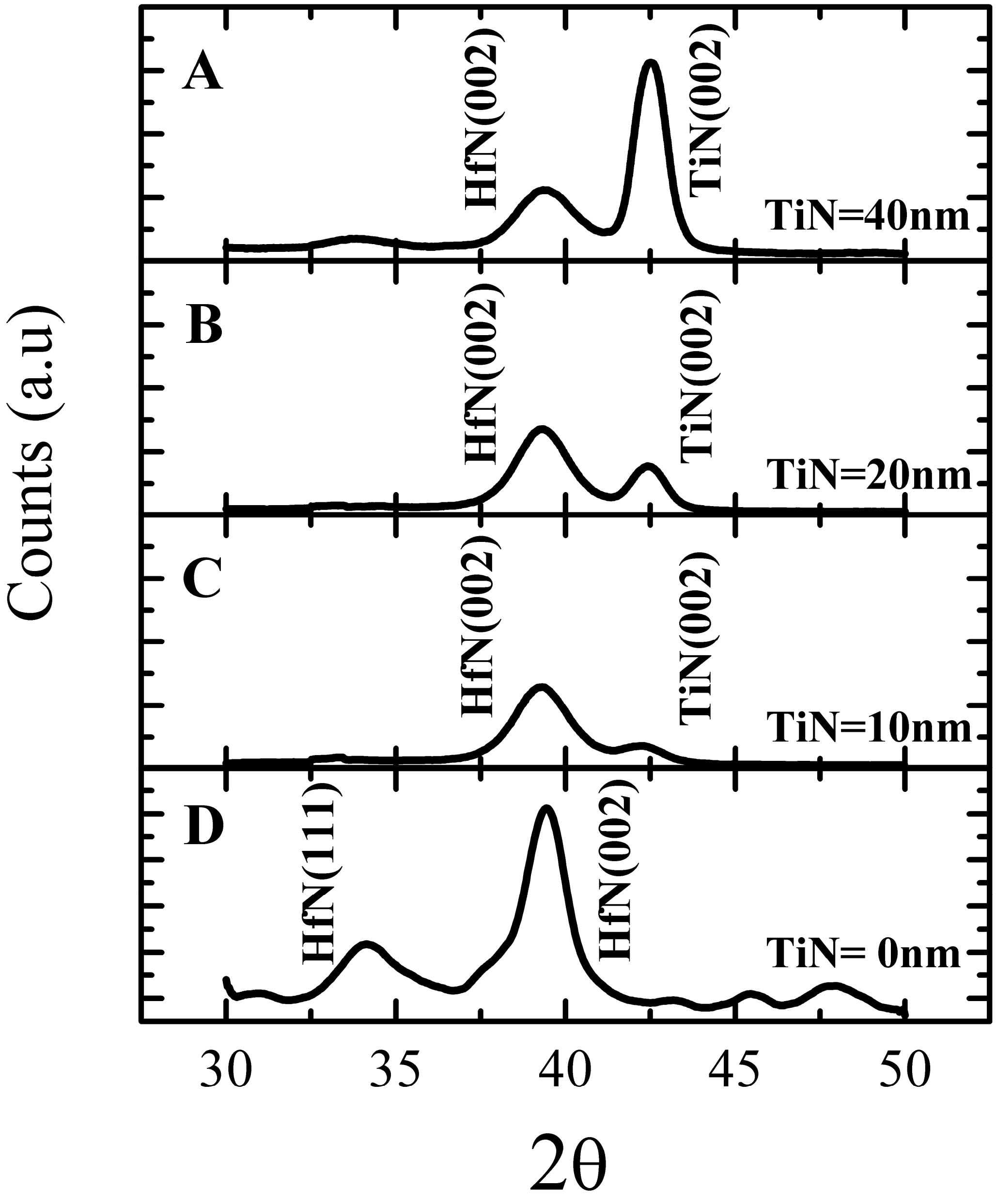

Figure 6.1. Localized X-ray diffraction pattern shows the HfN(002) peak and the weakening of the TiN(002) as the thickness of the TiN buffer layer is decreased. Both HfN and TiN are growing highly textured along the <00l> orientation on Si(001) substrate.

Table 6.1. X-ray diffraction peak positions of TiN(002) and HfN(002) for samples A - HfN(20 nm)/TiN(40 nm), B - HfN(20 nm)/TiN(20 nm) and C - HfN(20 nm)/TiN(10 nm). Their respective calculated out-of-plane ($a_{\perp}$) and in-plane lattice ($a_{//}$) constants are listed for reference. The peak positions HfN(111) and HfN(002) of sample D – HfN/Si(001) as well as their calculated out-of-plane ($a_{\perp}$) and in-plane ($a_{//}$) lattice are also listed.

Diffraction Peak		**TiN (002)**			**HfN (002)**		
Sample	**Thickness (nm) HfN/TiN**	2θ	$a_{\perp}$(Å)	$a_{//}$(Å)	2θ	$a_{\perp}$(Å)	$a_{//}$(Å)
A	20/40	42.50	4.251	4.235	39.34	4.577	4.492
B	20/20	42.38	4.262	4.229	39.24	4.588	4.486
C	20/10	42.28	4.272	4.224	39.28	4.584	4.489
		HfN (111)			**HfN (002)**		
D	80/0	34.12	4.548	4.506	39.44	4.566	4.497

as inserts. The diffraction patterns were taken from the <110> diffraction zone for all the samples. The diffraction dots from the single-crystal-like TiN, the highly epitaxial HfN and single crystalline Si substrate are indexed in all SAD patterns. It shows a clear cube-on-cube epitaxial quality of HfN/TiN/Si(001) for all cases. It is also interesting to note that the epitaxial growth quality of HfN on TiN(10 nm) is the best among all bilayer stacks indicating by the sharpness of the diffraction dots from HfN films. It suggests that, as long as a thin layer of TiN is introduced to initiate the epitaxial growth of the

HfN layer, the TiN thickness does not play an important role in the overall HfN epitaxial quality.

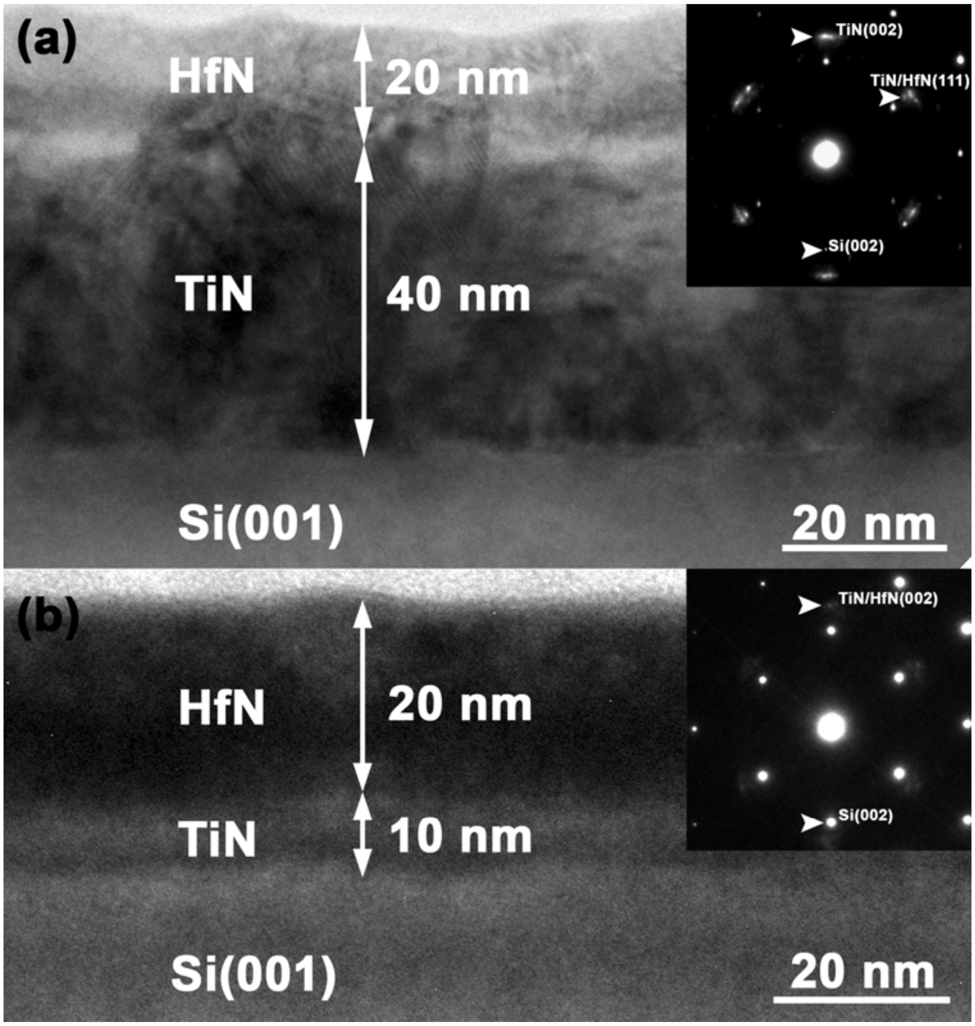

Figure 6.2. Low magnification cross-section TEM images show the as-deposited stacks (a) A - HfN(20 nm)/TiN(40 nm), and (b) C - HfN(20 nm)/TiN(10 nm). The corresponding SAD patterns indicate the epitaxial growth of the HfN/TiN stacks on Si(001).

Preliminary Cu diffusion barrier tests were performed for all the HfN/TiN stacks. Figure 6.3 shows low magnification TEM images of the Cu/HfN/TiN stacks after annealing at 500°C for 30 minutes. Inserts in Figure 3 show the corresponding SAD patterns. The SAD patterns show that the overall quality of the annealed layers HfN and TiN to be similar as that of the as-deposited stacks, inserts in Figure 6.2. The thickness of the Cu layers is of about 60 nm. After annealing, an ultra-thin layer between the Cu and HfN interface can be identified. The ultra-thin layer is caused by Cu diffusing into the HfN layer. The thickness of this ultra-thin layer can be estimated as the diffusion depth ($2\sqrt{D\tau}$) of Cu into the HfN layer. High resolution TEM images over the interface between the Cu and HfN layers are shown in Figure 6.4a and b. The ultra-thin layer is clearly observed and marked by the dotted lines. The diffusion depth ($2\sqrt{D\tau}$) is estimated to be about 2 nm in its thinnest part and up to 3 nm in the thickest part. Moreover, the electrical resistivity measured for all the HfN/TiN stacks on Si(001) is between 70 and 120 μΩ-cm, which makes them more attractive in comparison to pure TaN diffusion barriers (>200 μΩ-cm). The resistivity of the HfN/TiN bilayer stacks is slightly higher than the HfN bulk value, which might be due to the additional interface resistivity introduced in the thin film stack.

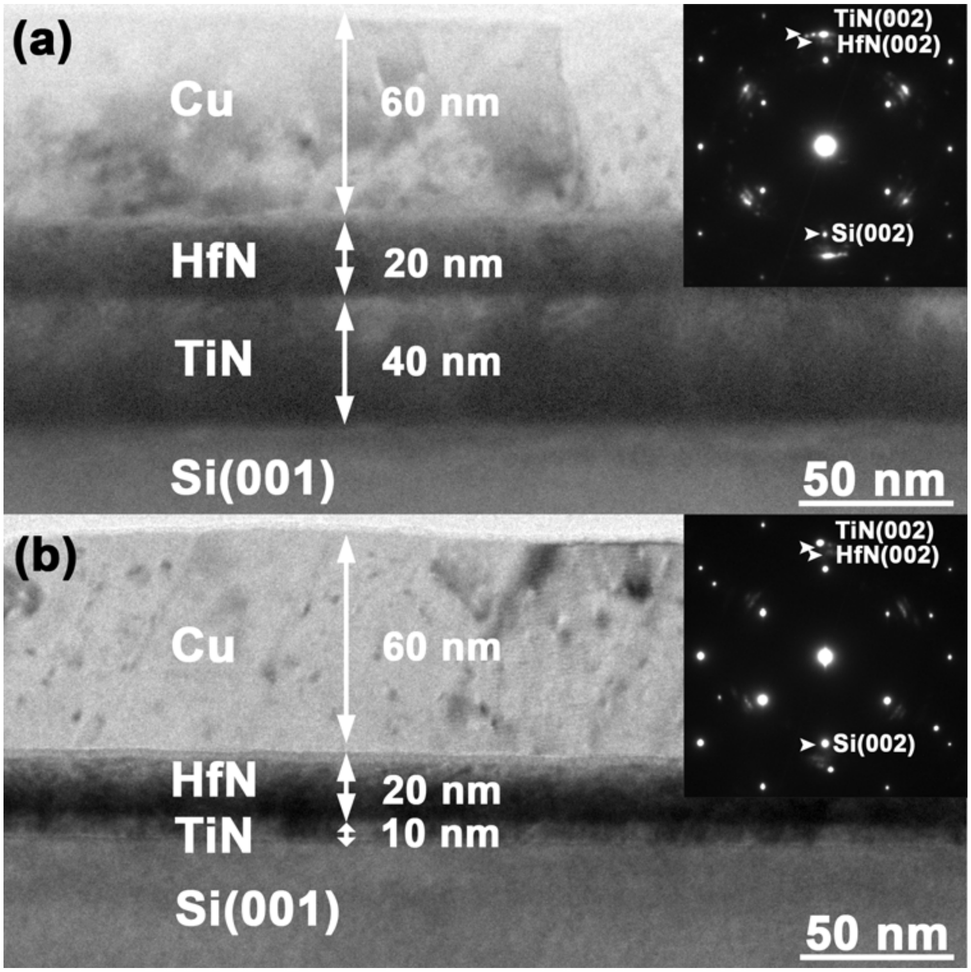

Figure 6.3. Low magnification TEM images of the annealed Cu/HfN/TiN samples. The Cu layer is about 60 nm thick and an ultra-thin diffusion layer can be seen at the interface of Cu/HfN. Inserts show the corresponding SAD pattern of the HfN/TiN stacks with no obvious change in the crystallinity of the film stack after annealing.

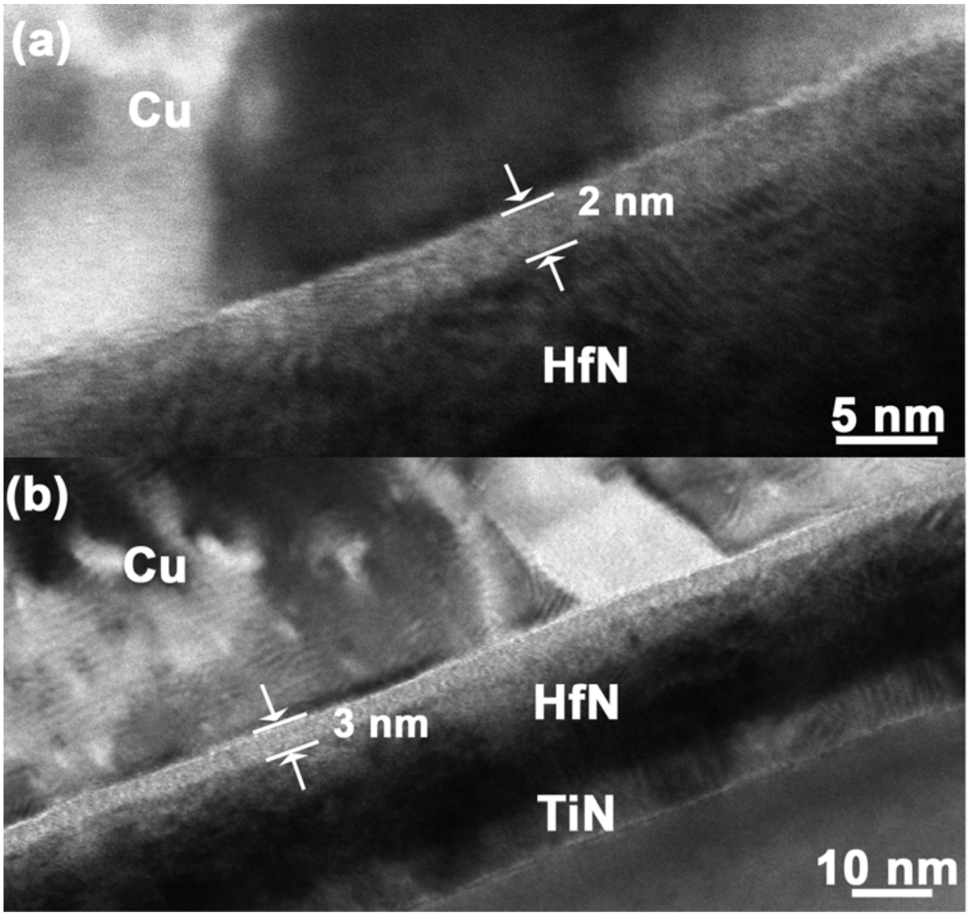

Figure 6.4. High resolution TEM images of the Cu/HfN interface for stacks (a) A - HfN(20 nm)/TiN(40 nm), and (b) C - HfN(20 nm)/TiN(10nm). The Cu diffusion distance is identified from the thin amorphous layer at the Cu/HfN interface with estimated distance about 2~3 nm over a large area after annealing at 500°C for 30 minutes.

6.5 Summary

In conclusion, we have deposited epitaxial cubic HfN (B1-NaCl structure) on Si(001) substrates by using a thin TiN buffer layer. The XRD results show that the lattice parameter of the highly textured cubic HfN (B1-NaCl structure) has strong correlation with the TiN buffer layer thickness. Low magnification TEM images for all the stacks show that the HfN and TiN layers are uniform and free of intermixing at both HfN/TiN and TiN/Si interfaces. The diffusion barrier property of the HfN/TiN stacks was studied by high resolution TEM, showing a Cu diffusion distance of 2 ~ 3 nm for vacuum annealing at 500°C for 30 minutes. The high crystallinity, low resistivity, good thermal stability and excellent Cu diffusion barrier property of the cubic HfN/TiN stacks prove their potential application as next generation diffusion barrier for Cu metallization.

CHAPTER VII

COPPER DIFFUSION CHARACTERISTICS IN EPITAXIAL HFN DIFFUSION BARRIERS

7.1 Overview

We explored the diffusivity of copper in epitaxial cubic HfN (B1-NaCl) thin films on Si(001) substrates deposited by a pulsed-laser-deposition technique. The epitaxial cubic HfN thin films were grown by using a thin TiN as a seed layer. The samples with a Cu layer deposited on top were annealed at 500°C, 600°C and 650°C for 30 minutes in vacuum, in order to study the diffusion properties of copper. The Cu diffusion into HfN was studied using high resolution TEM. The experimental diffusion depths, $2\sqrt{Dt}$, are estimated to be around 3, 4 and 5 nm for 500°C, 600°C and 650°C respectively. The diffusivity of Cu into epitaxial HfN follows the Arrhenius expression $D = D_0 \exp(-Q/kT)\,\text{cm}^2\text{s}^{-1}$ with $D_0 = 2.4\text{x}10^{-14}\ \text{cm}^2\text{s}^{-1}$ and $Q = 0.52$ eV.

7.2 Introduction

The continuous advance in the ultra large scale integration (ULSI) device technology requires new manufacturing techniques and new materials with improved performance. The use of copper as the interconnect material in the semiconductor industry requires high efficiency barriers to prevent copper diffusion into silicon. Recently HfN has been demonstrated as one of the diffusion barrier materials for copper metallization [91, 93]. HfN presents outstanding physical and chemical properties such as high thermal stability (T_m = 3380 ºC), relatively dense structure (ρ = 13.8 g/cm^3), high hardness (~21 GPa), and low bulk electrical resistivity (~33 μΩ-cm) [1]. A clear advantage of HfN in contrast to the extensively studied TaN is its lower bulk resistivity of ~33 μΩ-cm compared to ~200 μΩ-cm for TaN [15, 17, 18, 84]. Another advantage of HfN is that it presents a stable cubic B1-NaCl phase while the cubic TaN (B1-NaCl) is a metastable phase [1, 86]. The growth of HfN on silicon substrates has been mainly reported to be of polycrystalline quality and processed by reactive sputtering and atomic layer deposition [51, 54, 87, 94]. We have recently reported that epitaxial cubic HfN (B1-NaCl) can be deposited on Si(001) by using a thin TiN buffer layer, by using pulsed layer deposition (PLD) [93]. Epitaxial thin films have shown better Cu diffusion barrier properties, and usually have much lower resistivity than their polycrystalline phase due to fewer defects in their structures [4, 52, 89]. Up to the date, no data on the diffusivity of copper in HfN (B1-NaCl) barriers has been reported in the literature.

In this paper, in order to study the diffusivity of copper in epitaxial cubic HfN (B1-NaCl), we deposited a thin Cu layer (~60 nm) on top of the HfN/TiN/Si(001) samples at room temperature by PLD. Subsequent annealing of the samples is performed at 500, 600 and 650°C in vacuum for a period of 30 minutes. Finally, the diffusion depth of Cu into the epitaxial cubic HfN films was estimated by using high resolution TEM and the diffusion activation energy was evaluated by approximations to an Arrhenius equation.

7.3 Experimental Details

The deposition of Cu, HfN and TiN layers were performed in a multitarget pulsed laser deposition (PLD) system with a KrF excimer laser (Lambda Physik Compex Pro 205, λ= 248 nm, 10 Hz). The laser beam was focused to obtain an energy density of approximately 10 J·cm^{-2} at a 45° angle of incidence. The hot-pressed stoichiometric TiN and HfN targets were obtained from CERAC Inc. and Plasmaterials Inc., respectively. The substrates used were Si(001) with a resistivity value in the range of 10-20 Ω-cm. The substrate surface preparation consisted of a two-step cleaning; the first step is the removal of organic impurities and oxidation of the Si surface by using a piranha solution with 3:1 concentration ratio (sulfuric acid (98%)/hydrogen peroxide (30%)), and the final step used a buffer oxide etching solution (diluted HF) in order to remove the native silicon oxide present on the surface of the silicon substrate. The substrates were kept in an inert N_2 atmosphere until being loaded into a vacuum chamber. The vacuum chamber base pressure is of about 1 x 10^{-7} torr. The deposition of TiN and HfN were processed at and a substrate temperature of 700 ± 10 ^{o}C and the Cu film deposited onto the multilayer HfN/TiN was at room temperature. The microstructure of the as-deposited films was characterized by X-ray diffraction (XRD) (BRUKER D8 powder X-ray diffractometer, CuK_{α} radiation operating at 40 kV and 40 mA), and transmission electron microscopy (TEM) (JEOL 2010 analytical microscope with a point-to-point resolution of 0.23 nm). TEM samples were prepared through a standard cross-section preparation procedure: grinding, polishing and ion milling (precision ion polishing system (PIPS691), 3.5 KeV). To study the Cu diffusion characteristics in the HfN/TiN stacks, the stacks Cu/HfN/TiN were annealed in vacuum (1×10^{-7} torr) at 500^{o}C, 600 ^{o}C and 650 ^{o}C for 30 minutes. The Cu diffusion characteristics in these HfN/TiN films were studied by cross-sectional high resolution TEM.

7.4 Results and Discussion

Two sets of samples were studied in this paper. Both sets of samples have the same bilayer configuration with HfN deposited on a thin TiN buffer layer on Si(001) substrates. The HfN/TiN stacks have a total thickness of ~30 nm and ~65 nm, with the TiN buffer layer thicknesses being ~8 nm and ~42 nm respectively. X-ray diffraction pattern (intensity vs. 2θ) of the epitaxial multilayer HfN/TiN (~65 nm) as deposited on Si(100) is shown in Figure 7.1. Two major peaks, centered at 39.34° and 42.5° are indexed as HfN(002) and TiN(002), respectively. Both of these peaks are well aligned with that of silicon (004), which shows that HfN and TiN have grown on Si(001) substrate highly textured along the <00*l*> direction. A small peak is indexed to be HfN(111), suggesting that a small percentage of HfN grains are oriented along the <111> direction.

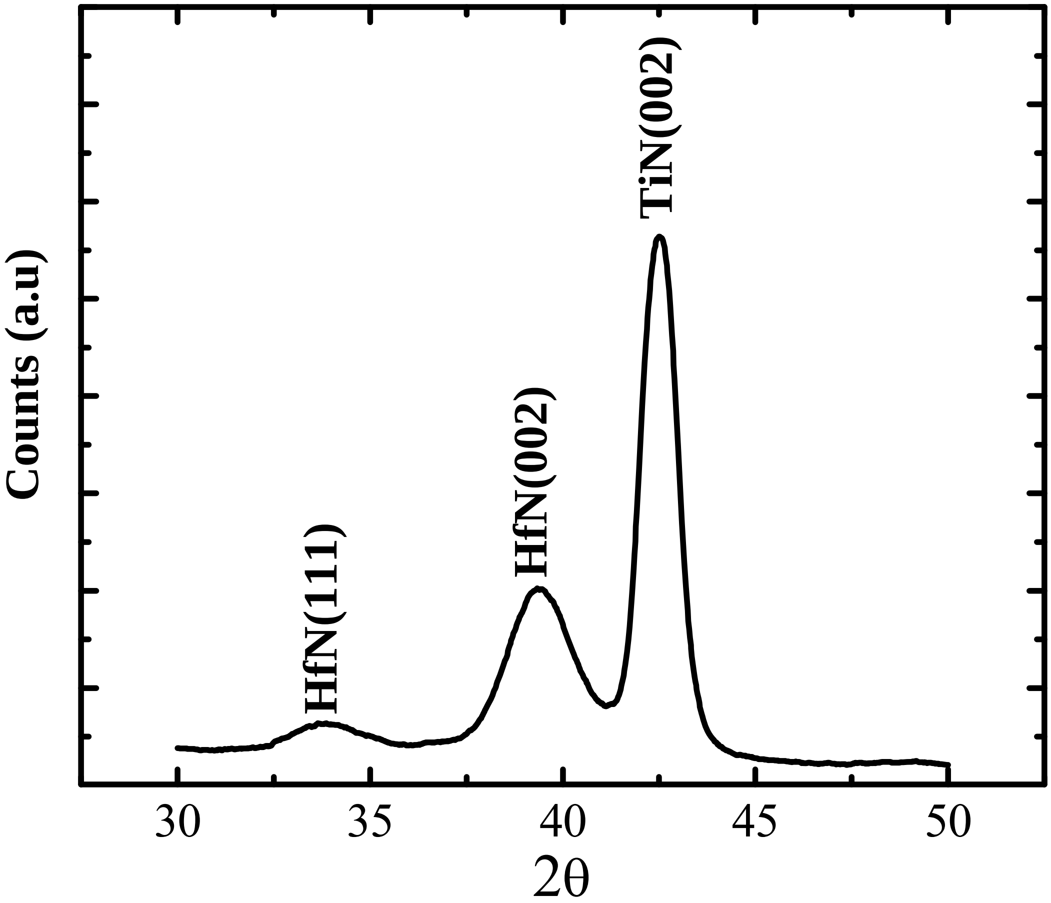

Figure 7.1. XRD pattern (intensity vs. 2θ) showing (002) peaks from TiN, and HfN deposited on Si(100) substrate. A very small peak HfN(111) can also be observed.

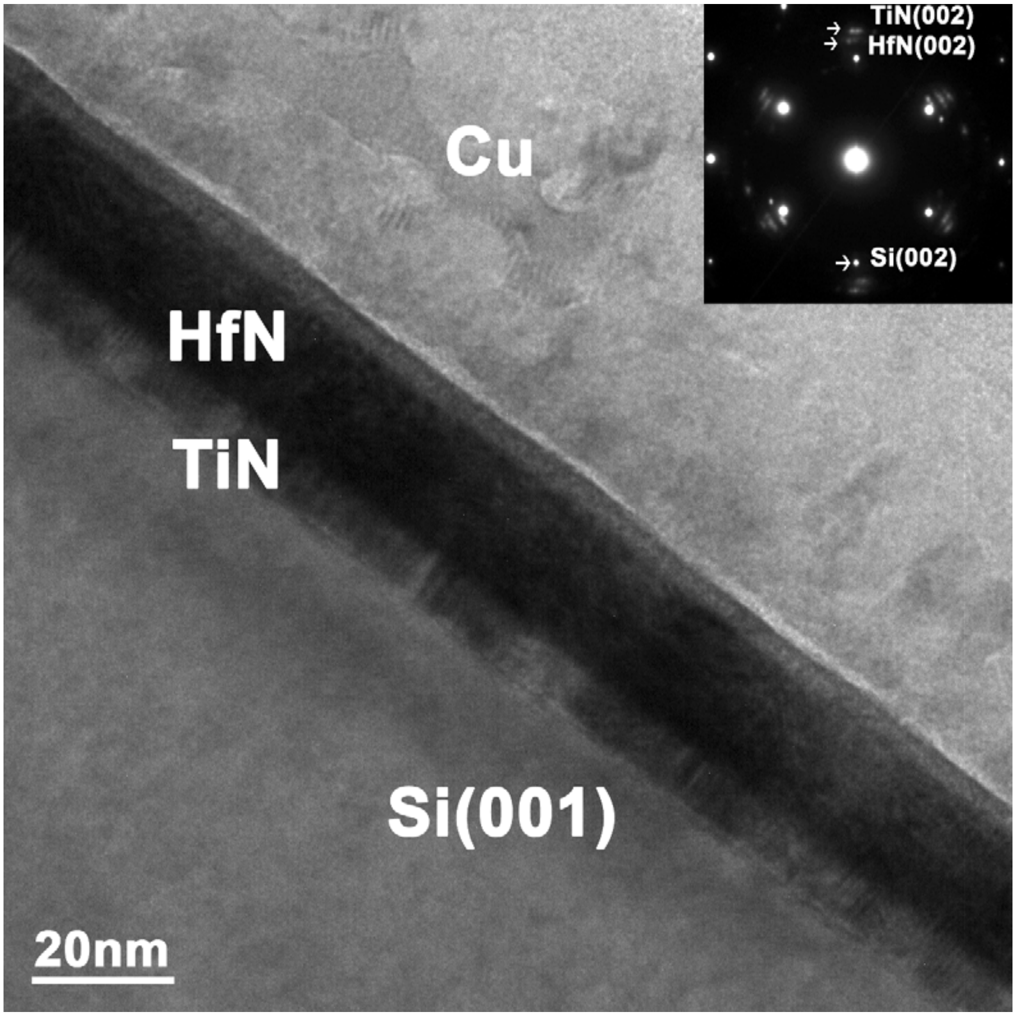

Figure 7.2. Low magnification cross-section TEM image shows the stack Cu/HfN/TiN/Si(001) annealed at 600°C for 30 minutes. The HfN/TiN bilayer thickness is around 30 nm. The corresponding SAD patterns indicate the epitaxial growth of the HfN/TiN stacks on Si(001).

A low magnification cross-section TEM image of the stack Cu/HfN(~22 nm)/TiN(~8 nm)/Si(001) annealed at 600°C for 30 minutes is shown in Figure 7.2. The sample corresponds to the one with a total thickness of ~30 nm for the bilayer HfN/TiN. The thickness of the copper layer is ~60 nm. The interfaces HfN/TiN and TiN/Si(001) are uniform with no obvious intermixing over a large area of the sample. The epitaxial quality of the sample can be identified from the corresponding selected-area-diffraction (SAD) pattern shown as an insert. The diffraction pattern was taken from the Si <110> zone. The diffraction dots from the epitaxial TiN, the epitaxial HfN and the single crystalline Si substrate are indexed in the insert. The SAD pattern shows a clear cube-on-cube epitaxial relation between HfN, TiN and Si substrate. At the interface between Cu and HfN, an ultra thin interlayer can be observed and identified as Cu diffusion into HfN.

To identify the nature of the Cu diffusion layer and the Cu diffusion depth as a function of the annealing temperature, we conducted a detailed high resolution TEM study on both sets of HfN/TiN/Si(001) stacks annealed at three different temperatures, i.e., 500^{o}C, 600^{o}C, and 650^{o}C. High resolution cross-section TEM images of the annealed samples are shown in Figure 7.3 and 7.4. Figure 7.3 a, b and c correspond to the HfN/TiN (~30 nm) deposited on Si and annealed at 500^{o}C, 600^{o}C, and 650^{o}C in vacuum during 30 minutes, respectively. Similarly, Figure 7.4 a, b, and c correspond to the HfN/TiN (~65 nm) deposited on Si and annealing temperatures of 500^{o}C, 600^{o}C, and 650^{o}C, respectively. The diffusion depths were determined by the contrast difference observed from at the HRTEM images. For all 6 cases, several HRTEM images were taken from different areas along the Cu/HfN interface to estimate the average diffusion depths.

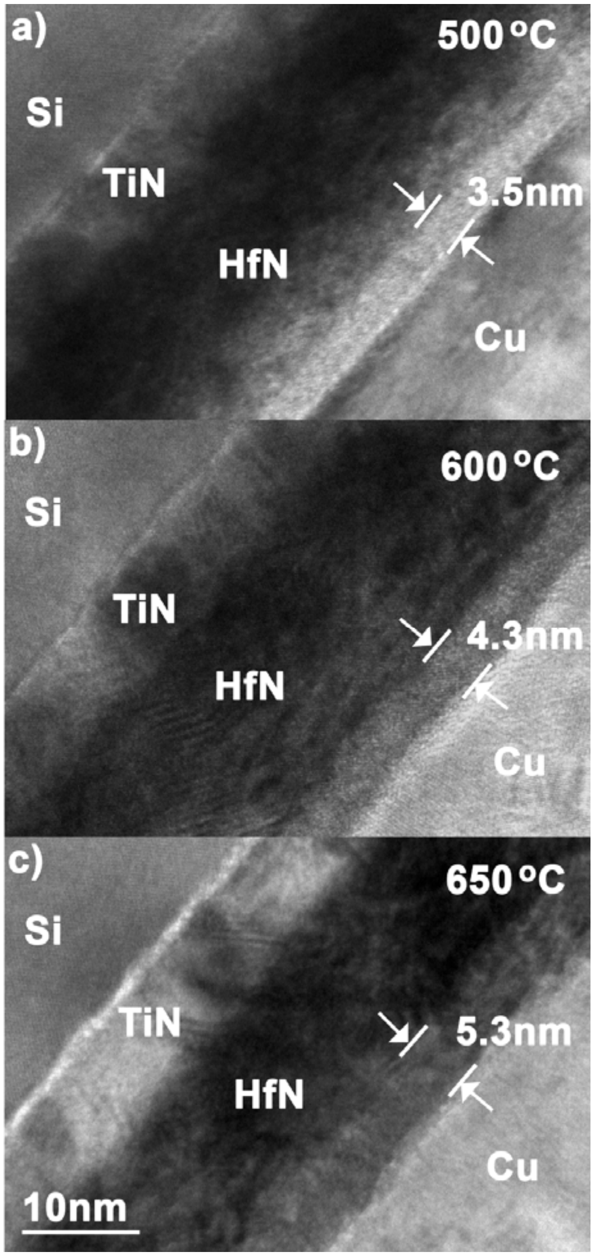

Figure 7.3. High resolution <110> cross-section TEM images at the interface between Cu and the epitaxial HfN/TiN (~30 nm) diffusion barrier after annealing for 30 minutes at (a) 500°C, (b) 600°C and (c) 650°C. The diffusion layer is estimated to be ~3.5 nm, ~4.3 nm and ~5.3 nm.

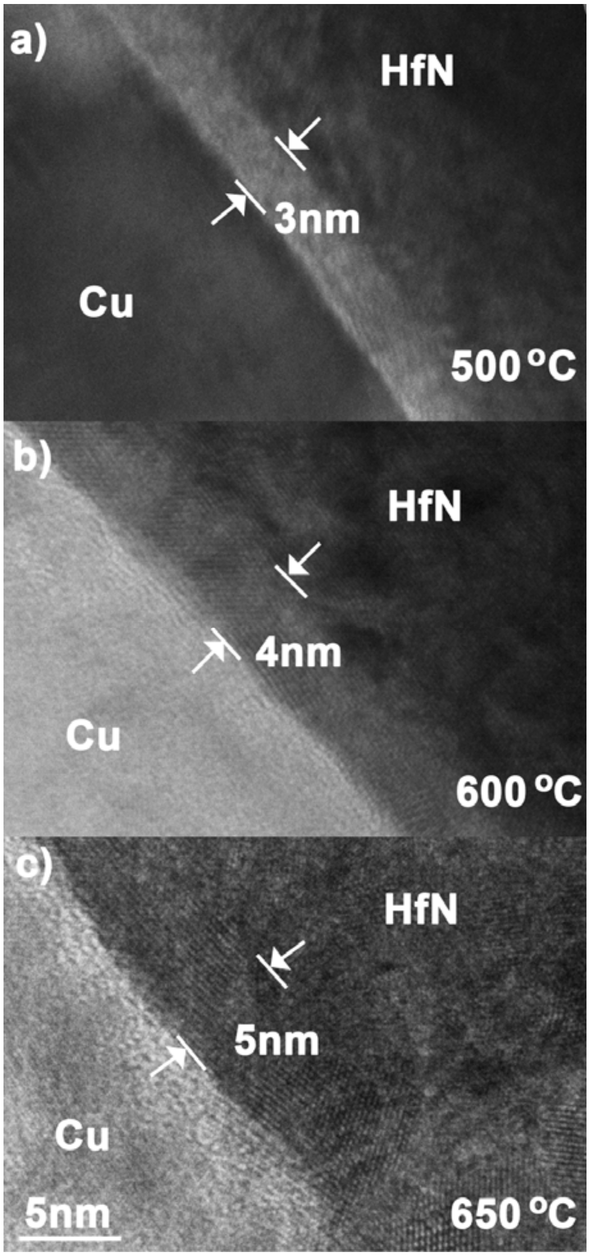

Figure 7.4. High resolution <110> cross-section TEM images at the interface between Cu and the epitaxial HfN/TiN (~60 nm) diffusion barrier after annealing for 30 minutes at (a) 500°C, (b) 600°C and (c) 650°C. The diffusion layer is estimated to be ~3 nm, ~4 nm and ~5 nm.

The Cu diffusion layer is uniform along the interface of HfN and Cu in all cases. The average Cu diffusion depths found for the HfN/TiN (~30 nm) on Si are ~3.5 nm, ~4.3 nm, and ~5.3 nm after annealing at 500°C, 600°C, and 650°C for 30min, respectively (Figure 7.3). For the HfN/TiN (~65 nm) on Si, the Cu diffusion depths found are ~3 nm, ~4, and ~5 nm after annealing at 500°C, 600°C, and 650°C for 30min, respectively (Figure 7.4). The diffusion depth of the stack with the thinnest TiN seed layer is slightly greater than of the stack with a thickest TiN layer. The better diffusion barrier of the stack with a relative thick TiN seed layer suggests that the epitaxial quality of HfN improves as the thickness of the seed layer increases.

The diffusion coefficient of Cu through the HfN epitaxial layer was calculated based on Fick's first and second law with an infinite-source diffusion. The solution of Fick's law under this approximation is given by equation 7.1:

$$C(x,t) = Cs \cdot erfc\left[\frac{x}{2\sqrt{D\tau}}\right] \text{...(7.1)}$$

with *Cs* as the surface concentration, *erfc* as the complementary error function, *x* is the diffusion depth, *D* is the diffusion coefficient at certain temperature, and τ is the time for diffusion. By making the argument of the *erfc* equal to unity results in an *erfc* value of 0.157 and therefore the concentration drops at 15.7% of its surface value. Since the diffusion mechanism is governed by Fick's laws, an estimation of the diffusion coefficient can be made by equating the *erfc* argument to unity and using the observed experimental diffusion depths at different temperatures. Then, the diffusion depth (*x*) of copper is approximated by $x = 2\sqrt{D\tau}$ and the diffusion coefficient (*D*) corresponds to the expression $D = {x^2}/{4\tau}$. The calculated D value for both samples annealed at 500°C, 600°C, and 650°C were calculated and found to be in the range 10^{-17} – 10^{-18} cm^2/s as shown in Figure 7.5. By using the Arrhenius equation, the diffusion is expressed as:

$$D = D_0 \exp(-Q_0 / k_B T) \text{ ....(7.2)}$$

where D_0 is the pre-exponential factor (cm^2/s), Q_0 is the activation energy (eV), k_B is the Boltzmann constant (8.6173×10^{-5} eV/K) and *T* is the temperature (K). After the evaluation of the diffusivity using the measured diffusion depth values from Figure 7.3 and 7.4, a general expression for Cu diffusion into epitaxial the HfN barrier layer is derived to be $D = (2.4 \pm 0.6) \times 10^{-14} \exp[-(0.52 \pm 0.3)eV / k_B T] cm^2 s^{-1}$. The activation energy is determined, for the first time, to be 0.52 eV for Cu diffusion into HfN. It is higher than that of Cu in TiN, 0.29 eV [29] and lower than that of Cu in TaN, 3.27 eV [17]. Even though the diffusion activation energy of Cu in HfN is relatively lower compared with that of TaN, HfN is still considered to be an effective diffusion barrier and even a better diffusion barrier than TaN for Cu diffusion in the temperature range of 500-650°C by comparing their diffusion depths at this temperature regime.

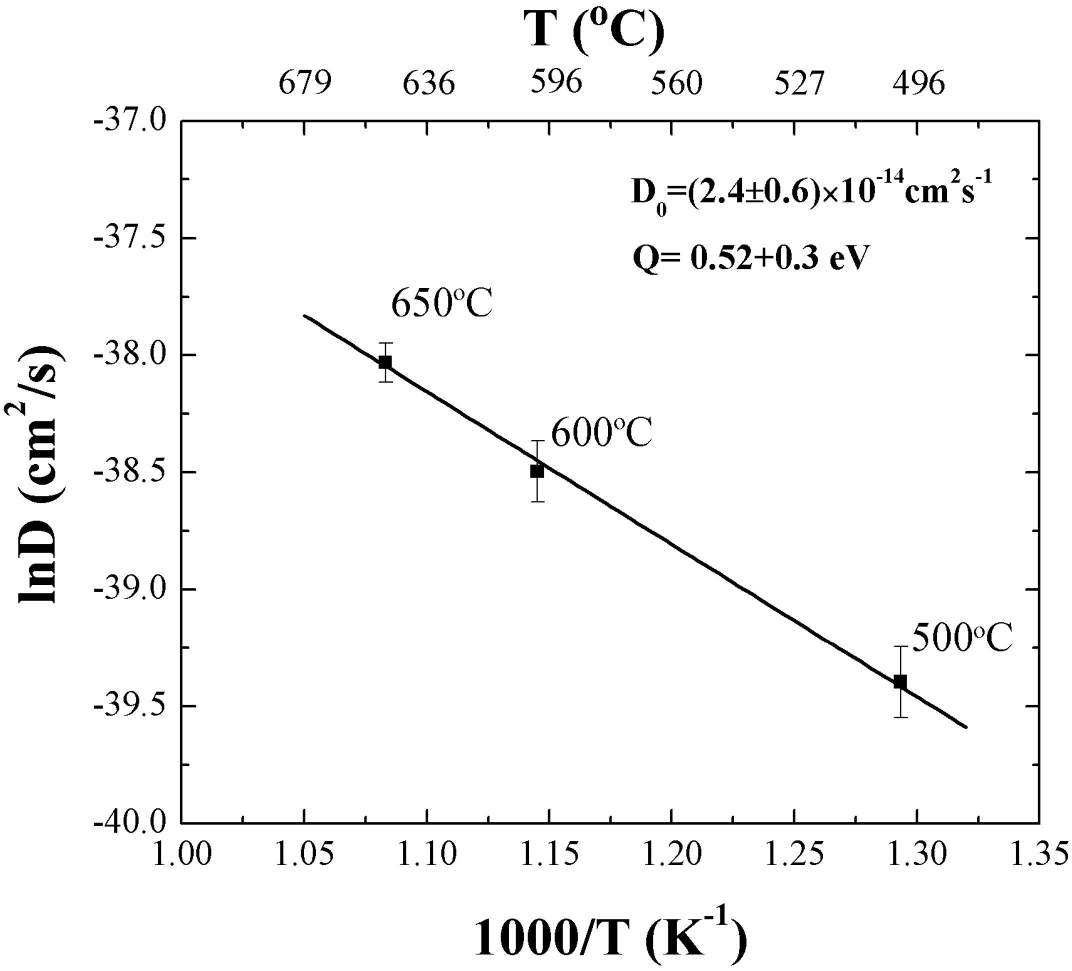

Figure 7.5. Arrhenius plot showing the Cu diffusion coefficients in epitaxial cubic HfN barrier layer for a temperature range from 500 to 650°C.

7.5 Summary

The Cu diffusion into epitaxial cubic HfN thin films was studied by high resolution TEM and the results were fitted to an Arrhenius equation based on the diffusion coefficients calculated at different annealing temperatures. HRTEM study demonstrates a good Cu diffusion barrier property for HfN with the Cu diffusion depth up to ~5 nm at an annealing temperature of 650°C for 30 minutes. This diffusion depth is much smaller than of epitaxial TaN barriers with 15 nm at 700°C annealing [17]. The diffusivity expression was determined as $D = (2.4 \pm 0.6) \times 10^{-14} \exp\left[-(0.52 \pm 0.3) eV / k_B T\right] cm^2 s^{-1}$ for temperatures from 500 to 650°C. Epitaxial HfN is a promising candidate for Cu diffusion barrier for Cu interconnects.

CHAPTER VIII

COMPUTATIONAL STUDIES OF THE MECHANICAL AND ELECTRONIC PROPERTIES OF TIN, TAN, AND HFN

8.1 Overview

The structural, mechanical and electronic properties of titanium nitride (TiN), tantalum nitride (TaN), and hafnium nitride (HfN) are studied by using first principle calculations within the Density Functional Theory (DFT) approach. This study focuses on three crystal structures such as B1-NaCl, B2-CsCl, and B3-ZnS, and additional hexagonal structures of TaN. The results are expressed in terms of equation of states, structural properties, elastic constants, density of states and band structures. Density of states calculations agree with results of experiments in terms of structural and mechanical properties. The band structure and density of states results explain the electronic properties.

8.2 Introduction

In general, transition metal nitrides are of great interest because of their outstanding physical and chemical properties: high melting point, low resistivity, good thermal conductivity and extremely high hardness [1, 2, 56, 95-101]. These ceramics have chemical and radiation inertness [102-106] and a higher energy of formation required to create defects [107]. They are the material of choice for various applications like protective coating for tools, diffusion barriers or metal gate contact in microelectronics, and lately as radiation resistant shields. Early experimental work found that they can have various crystalline structures [49, 50, 108-110], and subsequent work focused in studying their mechanical properties [111-113]. Metal nitrides' most recent applications involve the semiconductor industry, mainly because of the continued miniaturization of the transistor, the introduction of copper as the interconnect material and the need of novel materials compatible with the process of the IC industry [114].

In this paper, the results from the density functional theory calculations are reported. The calculations were performed for TiN, TaN and HfN, and for the crystal structures B1-NaCl, B2-CsCl, and B3-ZnS; additionally the hexagonal crystal phases ε-TaN, δ-TaN are included. The results of full structure optimization of these systems are reported as structural, mechanical and electronics properties in the way of crystal lattice parameters, equation of states (EOS), elastic constants (C_{11}, C_{12} *and* C_{44}), band structure (BS), density of states (DOS), and phonon band structures.

The theoretical results of this work are comparable with those of available experimental results and other similar theoretical studies. Finally, the importance of these calculations is discussed as well as its future use in large scale modeling on thin film interfaces and nucleation phenomena.

8.3 Calculation Details

Density Functional Theory calculations were performed by using the Vienna Ab-initio Simulation Package (VASP), which treats the periodicity of the system under study by using a plane waves approach. It uses the projected augmented plane wave pseudo-potentials [115] and the Perdew-Berke-Ernzerhof exchange correlation functional [116]. Preliminary calculations include initial testing of the k-point sampling mesh and the cutoff kinetic energy. The initial results turn out a 10×10×10 k-point mesh and a plane wave cutoff energy of 1000 eV for all the transition metal nitrides crystal structures. Additional considerations were taken by using the method of Methfessel-Paxton (MP) of order 1 for the Fermi-surface smearing, with a width of 0.1 eV for the total energy and band of states calculations, and the tetrahedron method with Bloch corrections for density of states calculations.

Full relaxation of the crystal structures was performed for various volumes near the experimental volume. Then, the energy and volume results are correlated and fitted to a third order Birch-Murnaghan equation of state (EOS) (Equation 8.1). From the EOS, important parameters such as equilibrium energy (E_0), equilibrium volume (V_0), bulk modulus (B_0) and the first derivative of the bulk modulus (B'_0) can be calculated.

$$E(V) = E_0 + \frac{9V_0B_0}{16}\left\{\left[\left(\frac{V_0}{V}\right)^{\frac{2}{3}} - 1\right]^3 B_0^{'} + \left[\left(\frac{V_0}{V}\right)^{\frac{2}{3}} - 1\right]^2 \left[6 - 4\left(\frac{V_0}{V}\right)^{\frac{2}{3}}\right]\right\} \qquad \text{.............(8.1)}$$

In the same fashion, in order to compare the previous results, a fitting by using the Rose's Universal binding curve (Equation 8.2) was used. The Rose's equation will permit us to find the lattice parameter (a_0), cohesive energy (E_{coh}), zero pressure volume (V_0), and the bulk modulus (B_0).

$$E(a^*) = -E_{coh}(1 + a^* + ka^{*3})e^{-a^*} \text{..} (8.2)$$

Where:

$$a^* = \frac{a - a_0}{a_0 \lambda}$$

$$\lambda = \sqrt{\frac{E_{coh}}{9V_0 B}}$$

$$k = \frac{\lambda(B' - 1)}{2} - \frac{1}{3}$$

$$B' = \left(\frac{dB}{dP}\right)$$

The mechanical properties such as elastic constants were also calculated. The calculation of the elastic constants can be achieved because the derivative of the energy can be represented as a function of the lattice strain, and then strain tensors are chosen in such a way that the volume was kept constant. The energy can be represented as an exponential even function of the strain. The expansion of the energy as function of the strain only contains even exponential power terms [117, 118]. For the calculation of the elastic constants C_{11} and C_{12} a volume conserving orthorhombic tensor (Equation 8.3) was used. The application of a volume conserving tensor affects the total energy of its unstrained crystal structure E(0), making a shift in energy to a new value E(±δ) (Equation 8.4). The bulk modulus is an important part in the calculations of the elastic constants and was obtained from the previous correlation between energy and volume from the Birch-Murnaghan equation of states. The bulk modulus B makes it possible to find the value of each individual constant C_{11} and C_{12} which are expressed in (Equation 8.5).

$$\varepsilon = \begin{pmatrix} \delta & 0 & 0 \\ 0 & -\delta & 0 \\ 0 & 0 & \dfrac{\delta^2}{1-\delta^2} \end{pmatrix} \quad \text{...}(8.3)$$

$$E(\pm\delta) = E(0) + (C_{11} - C_{12})V\delta^2 + O[\delta^4] \quad \text{...}(8.4)$$

$$B = \frac{C_{11} + 2C_{12}}{3} \quad \text{...}(8.5)$$

Finally the calculation of the elastic constant C_{44} was performed by using a volume conserving monoclinic strain tensor (Equation 8.6), which shifts the total energy of the crystal structure to a value E(±δ). The energy again can be expressed as a sum of even power term but the four power term is irrelevant because of being two orders of magnitude smaller. (Equation 8.7).

$$\varepsilon = \begin{pmatrix} 0 & \frac{1}{2}\delta & 0 \\ \frac{1}{2}\delta & 0 & 0 \\ 0 & 0 & \frac{\delta^2}{4-\delta^2} \end{pmatrix} \text{...(8.6)}$$

$$E(\pm\delta) = E(0) + \frac{1}{2}C_{44}V\delta^2 + O[\delta^4] \text{...(8.7)}$$

8.4 Results and Discussion

In this section, the results of the calculations performed by using the Density Functional Theory approach are presented for TiN, TaN, and HfN. From these results, the equation of states for the different crystal structures of TiN, TaN and HfN are obtained and they are shown in Figures 8.1, 8.2 and 8.3. The most important variables obtained from these calculations are energy, volume and pressure. The relation between energy, volume and pressure are very important parameters in order to understand certain points of a crystal phase, the equilibrium structure, crystal phase transition paths and their stable structures in nature. The density functional theory calculations were performed by systematically changing the volume and conserving the symmetry of the crystal phase which results in a variation of the energy and pressure. The results were correlated and plotted in pairs as Energy-Volume, Pressure-Volume, and Enthalpy-Pressure, shown in figures 8.1, 8.2 and 8.3 for TiN, TaN, and HfN respectively. The equilibrium point for each of the crystalline phases corresponds at a minimum point of their respective Energy-Volume curve. The same point corresponds to the zero pressure at equilibrium volume which can be observed from their respective Pressure-Volume curve. The most important information can be extracted from the Enthalpy-Pressure curve, where pressure induced phase transitions can be observed for all the transition metal nitrides included in this study. For the case of TiN, Figure 8.1c, the Enthalpy–Pressure curve shows the first phase transition from B3-ZnS to B1-NaCl at about -16.4 GPa (expansion), while a second transition from the crystal structure B1-NaCl to B2-CsCl occurs at approximately 345.8 GPa (compression). The Enthalpy-Pressure figure for TiN also shows that the most stable phase, at zero pressure, is the B1-NaCl structure compared to B2-CsCl and B3-ZnS crystal structures. At the equilibrium point, zero pressure, of the Energy-Volume curve the volume is 19.26 Å^3 which turns a lattice parameter of 4.25 Å. For TaN, the curves Energy-Volume, Pressure-Volume and enthalpy-pressure are shown in Figure 8.2. From the enthalpy-pressure curves the most stable phase at zero pressure is the δ-hexagonal phase. Two phase transitions can be observed, the first one from B3-ZnS to the δ-hexagonal and the second from δ-hexagonal to the B2-CsCl at pressures of -26.0 GPa (expansion) and 245.0 GPa (compression) respectively. The equilibrium, at zero pressure, is at a volume of 21.66 Å^3 or lattice parameter values a = 2.94 Å and c = 2.89 Å of the stable hexagonal phase. Finally, the results for HfN are plotted and shown in Figure 8.3 as Energy-Pressure,

Pressure-Volume and Enthalpy-Pressure. The phase transition of HfN is similar to the phase transition of TiN, from B3-ZnS to B1-NaCl at a pressure of -12.9 GPa (expansion) and from B1-NaCl to B2-CsCl (compression) at a relative high pressure of 271.0 GPa. The stable phase, at zero pressure, is the B1-NaCl structure with a volume of 23.38 Å^3 or a lattice parameter value of 4.53 Å.

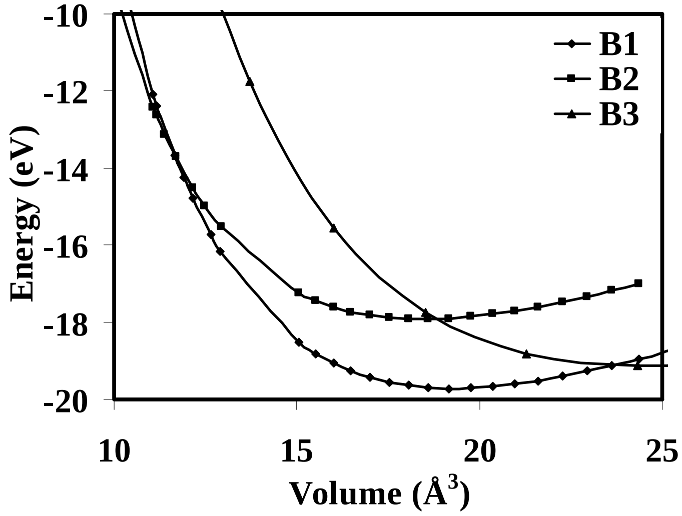

a)

Figure 8.1. (a) Energy-Volume, (b) Pressure-Volume and (c) Enthalpy-Pressure related curves of TiN for the crystal structures B1-NaCl, B2-CsCl and B3-ZnS. The enthalpy as a function of pressure shows the transition from phase B3-ZnS to B1-NaCl at -16.4 GPa (expansion) and the transition of phase B1 to B2 at 345.8 GPa (compression).

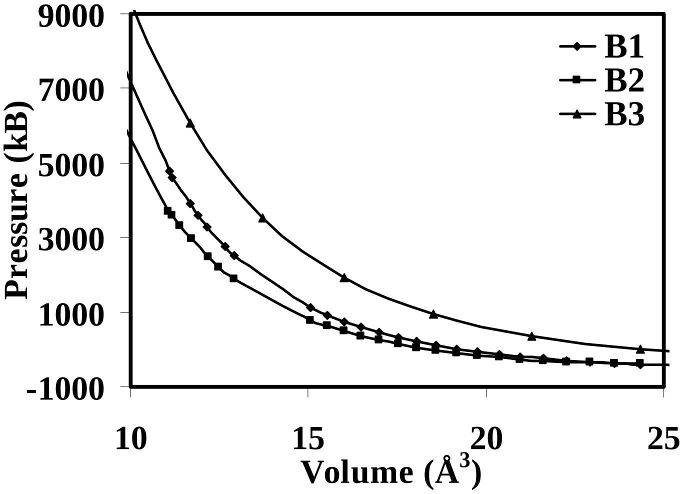

b)

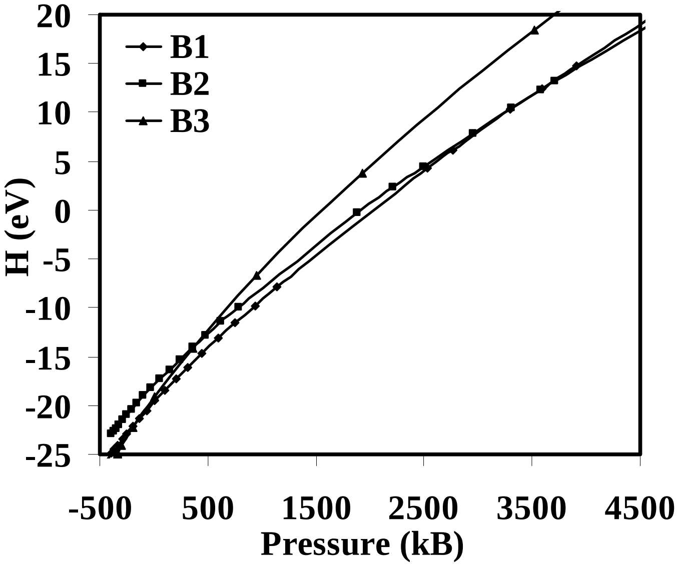

c)

Figure 8.1. Continued.

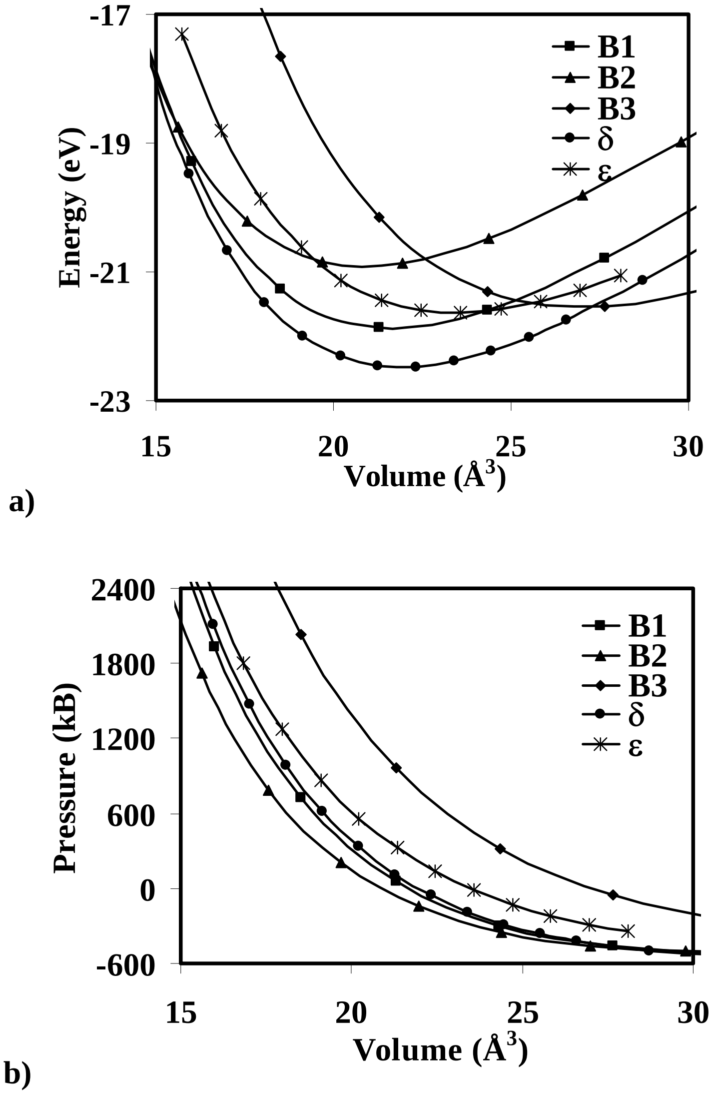

Figure 8.2. (a) Energy-Volume, (b) Pressure-Volume and (c) Enthalpy-Pressure related curves of TaN for the crystal structures B1-NaCl, B2-CsCl and B3-ZnS, ε-hexagonal and δ-hexagonal. The enthalpy as a function of pressure shows the transition phase from B3-ZnS to δ-hex at -26.0 GPa (expansion) and the transition of phase δ-hex to B2 at 245.0 GPa (compression).

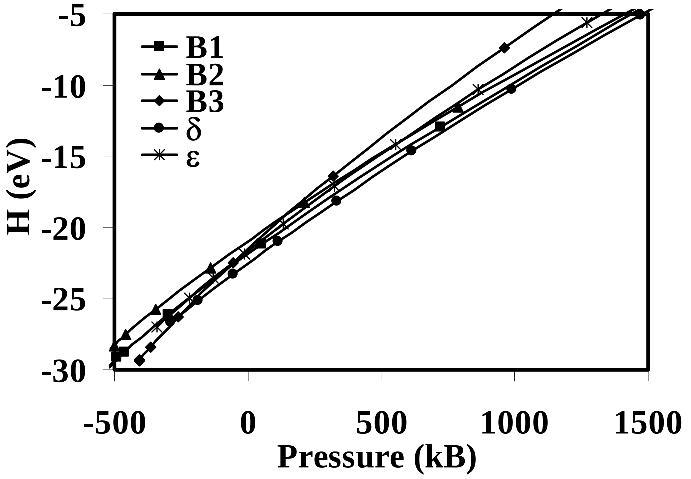

c)

Figure 8.2. Continued.

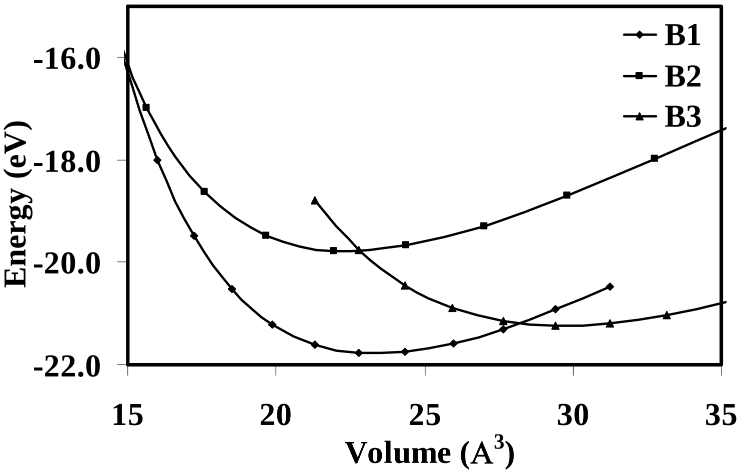

a)

Figure 8.3. (a) Energy-Volume, (b) Pressure-Volume and (c) Enthalpy-Pressure related curves of HfN for the crystal structures B1-NaCl, B2-CsCl and B3-ZnS. The enthalpy as a function of pressure shows the transition from phase B3-ZnS to B1-NaCl at -12.9 GPa (expansion) and the transition from phase B1-NaCl to B2-CsCl at 271.0 GPa (compression).

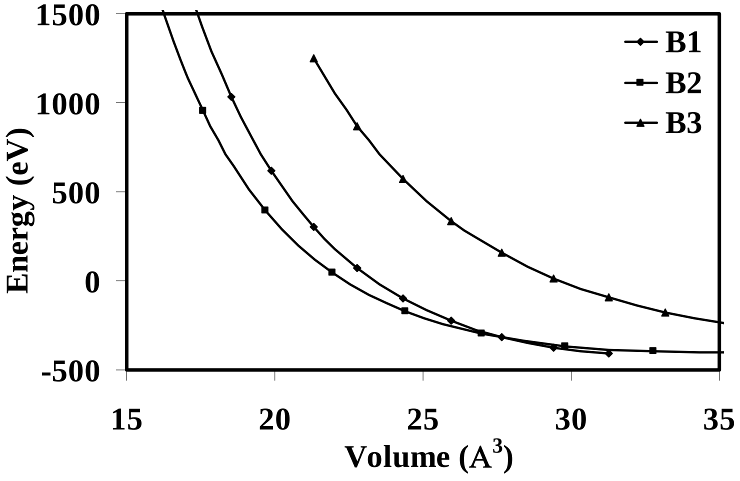

b)

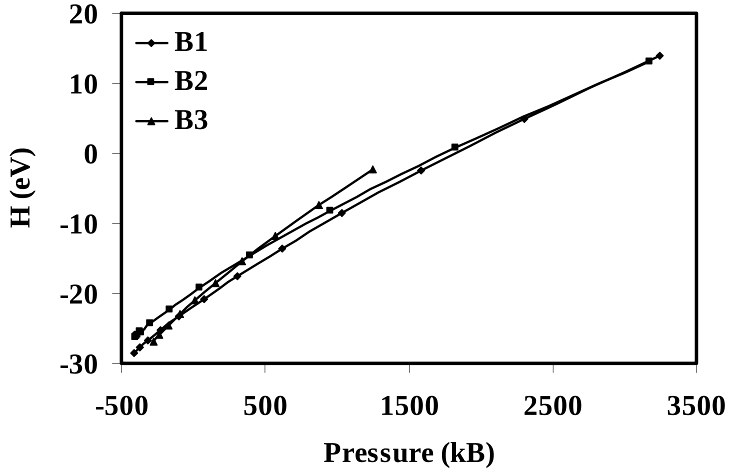

c)

Figure 8.3. Continued.

A summary of the calculated properties is presented in Tables 8.1 – 8.3 for the different crystal phases of TiN, TaN, and HfN. The calculated properties such as lattice parameter, unit cell volume, bulk modulus, derivative of the bulk modulus and elastics constant are listed in Tables 8.1 - 8.3. As previously mentioned, the calculations of these properties involved the use of equations of state approximations and volume conserving tensors. Most metal nitrides research efforts by using Density Functional Theory calculations have been reported only for the B1-NaCl crystal structures which are comparable to the results reported in this work [101, 119].

Tables 8.1 – 8.3 list the calculated elastic constants values which are within good agreement with experimental results, even thought the uncertainty in measuring elastic constants by using neutron scattering techniques could be as high as 10%. The elastic constants have to satisfy the stability conditions for a cubic crystal structure [120], such as:

$$C_{11} + 2C_{12} > 0\,, \qquad C_{44} > 0\,, \qquad \text{and} \qquad C_{11} - C_{12} > 0 \;\ldots\ldots\ldots\ldots\ldots\ldots\ldots\ldots\ldots(8.8)$$

i.e., all the bulk B, shear $G = C_{44}$, and tetragonal shear modulus $G' = (C_{11} - C_{12})/2$ are positive. The results in Tables 8.1 – 8.3 for the B1-NaCl crystal structure satisfy all three criteria (Equation 8.8), therefore they are stable phases consistent with experiments. In general, for the B1-NaCl crystal structure of TiN, TaN and HfN, both theory and experimental results hold that $B > G' > G > 0$ which makes the shear modulus G the main constraint on stability. The tetragonal shear modulus G' measures the response of a crystal under volume conserving tetragonal shear strain, which involves stretching of the metal-N bonds and bending of metal-metal bonds. In these crystals $C_{11} \gg C_{12}$ is satisfied, with C_{11} determined by the nearest-neighbor interaction similar to the bulk modulus B, and G' having the same trend as B. The shear modulus $G(C_{44})$ is one of the most important parameters governing indentation hardness. The hardness of a material is defined as its resistance to another material penetrating its surface and it is determined by the mobility of dislocations. In covalent hard materials, the bond-breaking energy under plastic deformation and the bond-restoring energy under elastic shear strain are very similar, so that one of the determining factors of hardness is the response of covalent bonds to shear strain [121].

In the case of the crystal structure B2-CsCl and B3-ZnS, the stability conditions are not fulfilled completely and therefore the crystal structures are non-stable. For B2-CsCl and B3-ZnS, the condition of $B > G'$ is not satisfied. Additionally, the G value is very low and sometimes even zero. These two failed conditions can be summarized by saying that they are very unlikely to stand an external shear strain or have a very low hardness.

Table 8.1. Results of theoretical calculations show the structural and mechanical properties of various TiN crystal phases. Others experimental and theoretical results are also listed.

Crystal(Method)	***a (Å)***	***Volume (Å^3)***	***B (GPa)***	***B'***	***C_{11} (GPa)***	***C_{12} (GPa)***	***C_{44} (GPa)***
B1*	4.26	19.26	275.3	4.2	565.9	130.3	162.6
B1(exp) [1]	4.24						
B1(exp) [122]			318.0		625	165	163
B1 [123]	4.24		313.0		642	148	159
B1(LDA) [124]			310.0		735	93	250
B1(GGA) [124]			270.0		610	100	168
B1(LDA) [125]	4.18		319.0	4.3	704	125	168
B1(PW91) [125]	4.24		282.0	4.2	600	120	159
B1(PBE) [125]	4.24		282.0	4.2	598	118	159
B1(RPBE) [125]	4.26		266.0	4.2	561	116	156
B1(GGA) [126]	4.25		286.6		585	137	165
B2*	2.64	18.42	254.9	4.2	628.2	68.2	13.4
B3*	4.61	24.50	195.4	3.9	290.1	154.5	93.4

*This work

Table 8.2. Results of theoretical calculations show the structural and mechanical properties of various TaN crystal phases. Others experimental and theoretical results are also listed.

Crystal(Method)	***a (Å)***	***c (Å)***	***Volume ($Å^3$)***	***B (GPa)***	***B'***	***C_{11}(GPa)***	***C_{12} (GPa)***	***C_{44} (GPa)***
B1*	4.42		21.60	320.5	4.6	727.0	117.2	21.0
B1(exp) [1]	4.34							
B1(FLAPW-GGA) [56]	4.42			338.0				
B1(FLAPW) [56]	4.37			378.0				
B2*	2.76		20.98	307.0	4.3	920.9	0.0	79.3
B3*	4.77		27.13	239.2	4.1	282.2	217.7	130.3
δ-hex*	2.94	2.89	21.67	336.0	4.3			
δ-hex exp [49]	2.93	2.86						
ε-hex*	5.23	2.93	69.43	277.3	4.1			
ε-hex exp [1, 49]	5.18	2.90						

*This work

Table 8.3. Results of theoretical calculations show the structural and mechanical properties of various HfN crystal phases. Others experimental and theoretical results are also listed.

Crystal(Method)	***a (Å)***	***Volume (Å^3)***	***B (GPa)***	***B'***	***C_{11} (GPa)***	***C_{12} (GPa)***	***C_{44} (GPa)***
B1*	4.54	23.39	267.6	4.3	593.2	104.8	116.2
B1(exp) [1]	4.52						
B1 (FLAPW-GGA) [56]	4.54		278.0				
B1(FLAPW) [56]	4.37		320.0				
B1(GGA) [126]	4.54		279.8		597.0	121.0	118.0
B2*	2.82	22.36	233.1	4.3	549.8	74.7	-10.3
B3*	4.91	29.61	192.7	4.1	291.3	143.5	94.1

*This work

The electronic properties are presented as density of states (DOS) and electronic band structures (BS) in Figures 8.4, 8.5, and 8.6 for TiN, TaN and HfN respectively. The DOS and BS were calculated at the equilibrium point previously obtained when calculating the density of states for each of their crystal structures. Interestingly, the results from the cubic phases of the three metal nitrides in study show that the B1-NaCl and B2-CsCl crystal structures have a quasi-metallic behavior compared to the semiconducting B3-ZnS crystal phase, where a bandgap can be observed. The corresponding DOS curves show a clear picture about the type of orbital and its contribution to the electronic band structure. The contribution of the density of states around the conduction band energy levels is given mostly by the *d* orbitals of the metal nitride, and the contribution around the valence band energy levels by the *p* orbitals of the nitrogen atoms. The band structures of the metal nitrides are quite similar within the same crystal structure. They all have a characteristic low-lying band, which is derived from non metal *2s* states, as illustrated in their respective DOS curve Figures 8.5 – 8.7 for the cubic structures B1-NaCl, B2-CsCl and B3-ZnS. Above the low-lying band and separated by an energy gap from the non metal *2s* there can be found three overlapping bands which originate from the Γ point. By looking at the adjacent DOS curve, these bands can be observed to derive from the *2p* states of the N atom and the *d* states of the metallic atom. This amount of hybridization varies from crystal structure to crystal structure but essentially keeps the hybrid characteristic. The next bands predominantly derive from the transition metal *d* state with a small contribution of the *2p* states. The highest lying bands represent a mixture of states with different symmetries, originating from both constituents.

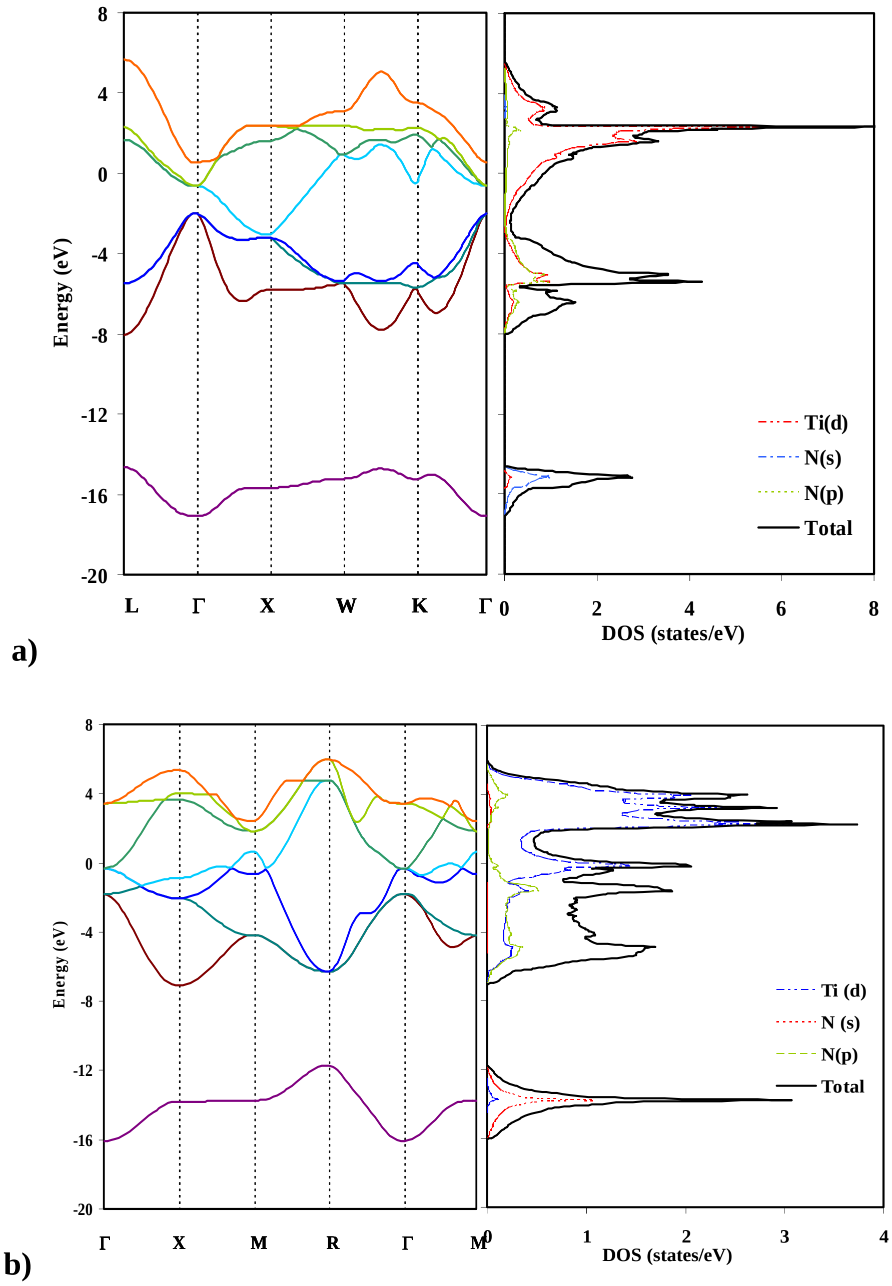

Figure 8.4. Density of states and band structure for TiN (a) B1-NaCl, (b) B2-CsCl and (c) B3-ZnS crystal structure.

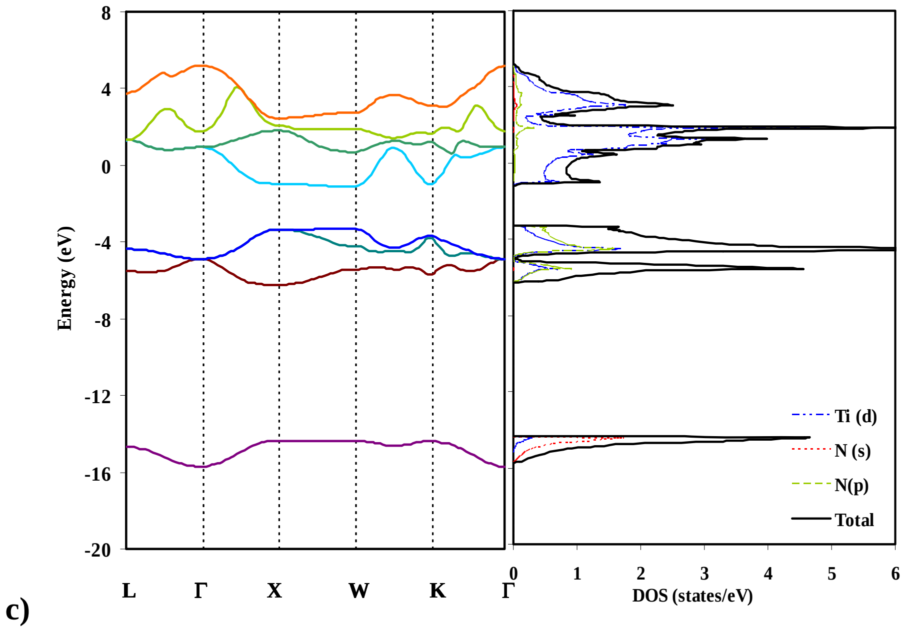

Figure 8.4. Continued.

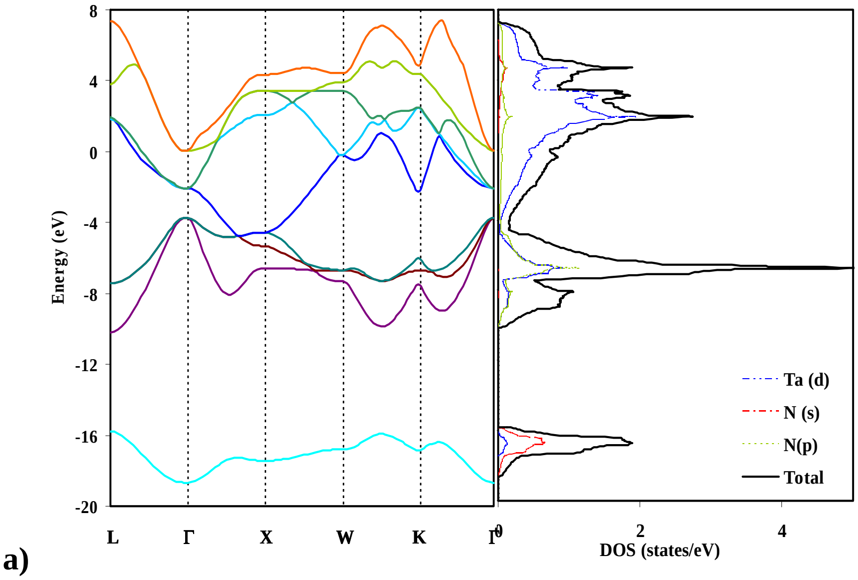

Figure 8.5. Density of states and band structure for TaN (a) B1-NaCl, (b) B2-CsCl and (c) B3-ZnS crystal structure

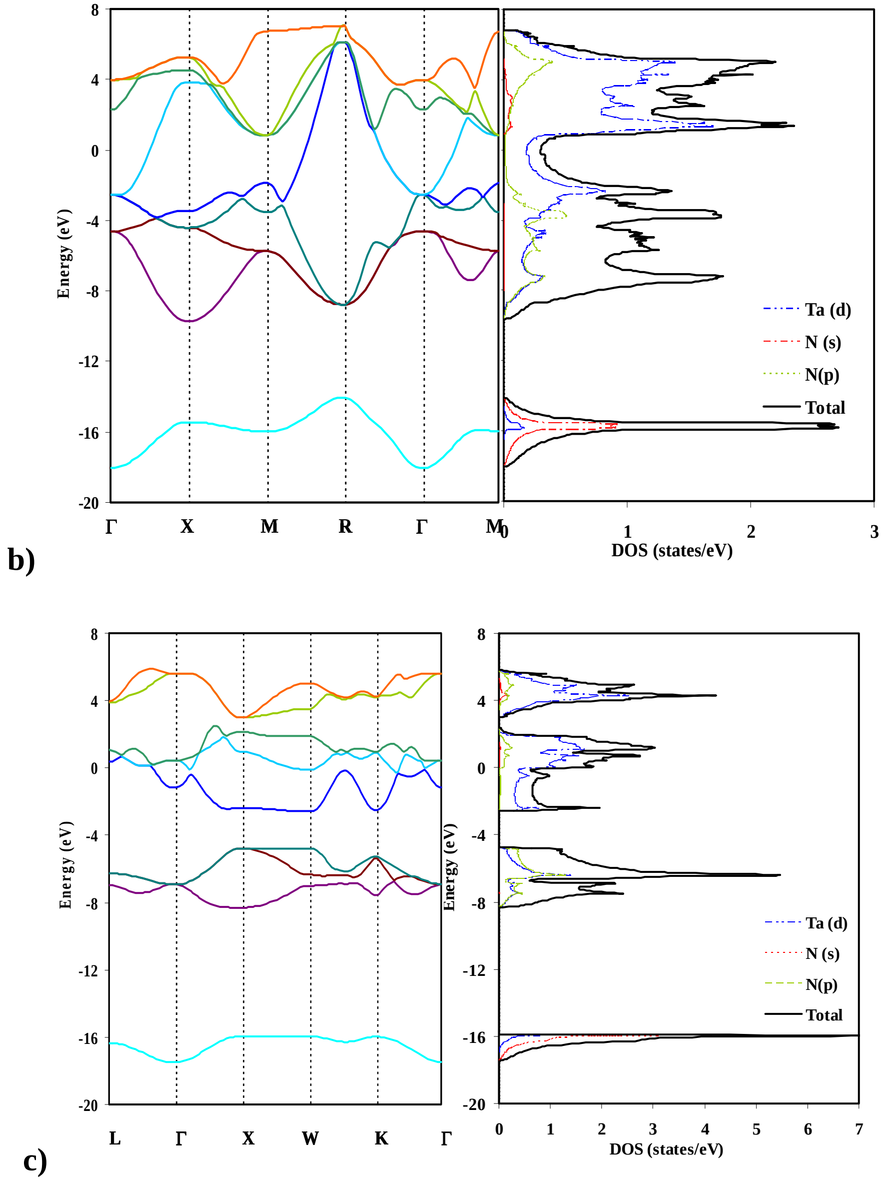

Figure 8.5. Continued.

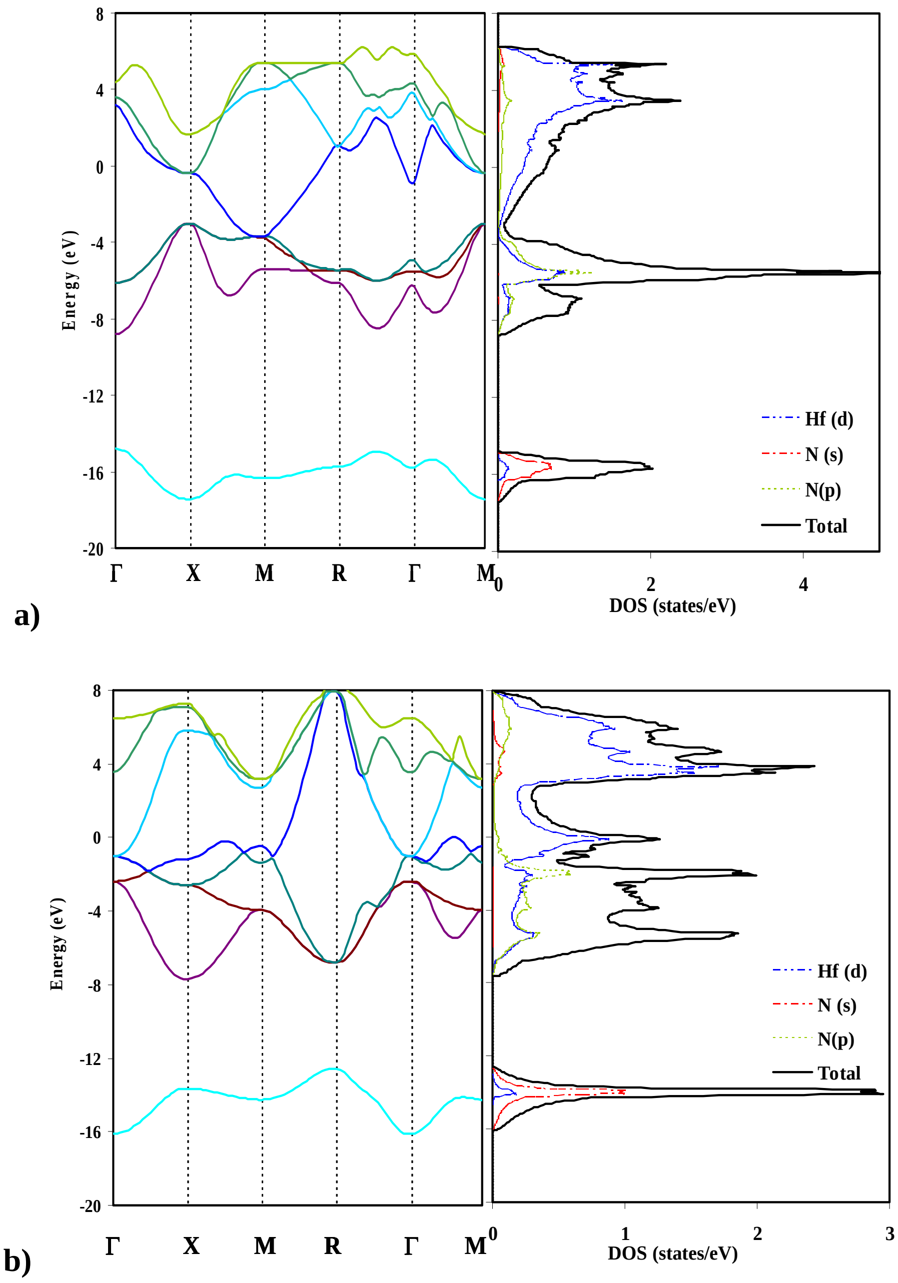

Figure 8.6. Density of states and band structure for HfN (a) B1-NaCl, (b) B2-CsCl and (c) B3-ZnS crystal structure

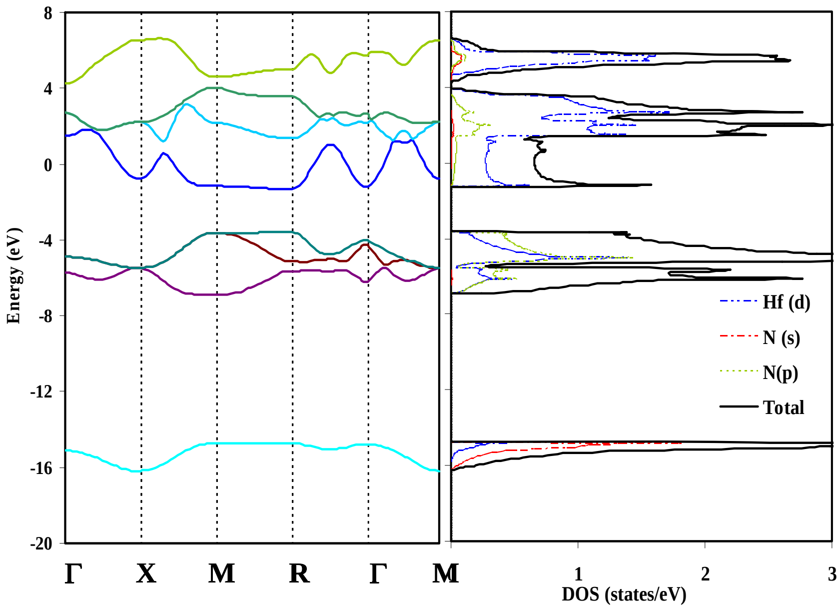

c)

Figure 8.6. Continued.

8.5 Summary

Systematic first principles calculations of the structural, elastic, and electronic properties of the selected metal nitrides TiN, TaN and HfN have been carried out. The structural properties for the crystal structure B1-NaCl are in good agreement with experiments. On the other hand, the elastics and electronics properties are comparable to the available experimental results. The properties of the crystal structures B2-CsCl and B3-ZnS are also calculated and they explain their non-stable behavior. Additionally, the hybrid behavior is well explained by the density of states curves, with covalent and ionic bond contribution between the N and the metal. Finally, by using computational techniques such as density functional theory, new materials properties can be predicted or further explained compared to the ambiguity of some experimental methods.

CHAPTER IX

SUMMARY AND CONCLUSIONS

Novel metal nitride materials, such as TiN, TaN and HfN, have been thoroughly studied as Cu diffusion barriers. The processing and extensive study of their diffusion properties against Cu diffusion has been accomplished. This dissertation was arranged in the following way. Chapter I introduced the current research status of Cu diffusion barriers. Chapters II and III included information about the properties, processing techniques and research methodology. Chapter IV was focused on the growth and diffusion barrier property of an ultra-thin epitaxial cubic TaN diffusion barrier by using a thin TiN seed layer. Chapter V presented the processing of epitaxial and highly textured HfN deposited on MgO and Si substrates respectively. Chapter VI focused on the growth and diffusion barrier of an ultra-thin epitaxial cubic HfN diffusion barrier by using a thin TiN seed layer. Chapter VII explored the Cu diffusion characteristics in epitaxial HfN diffusion barriers growth as specified in Chapter VI. Finally, Chapter VIII presented first principle calculations of the structural, mechanical, and electronic properties of TiN, TaN and HfN.

In Chapter IV, it was shown that an ultra-thin TiN seed layer, as thin as ~1 nm, can stabilize the epitaxial metastable cubic TaN films. Both XRD and cross-section TEM structural characterizations clearly show that cubic TaN with preferred (*00l*) orientation on Si (001) substrates has been established by TiN seed layers with thickness ranging from 15nm to 1 nm. The high quality epitaxial growth, low resistivity, good thermal stability and excellent Cu diffusion barrier property of the TaN/TiN bilayers demonstrate a strong potential for their application as diffusion barriers for Cu interconnects.

In Chapter V, high quality epitaxial and highly textured HfN films have been deposited on MgO and Si substrates, respectively, by PLD. Both XRD and TEM results suggest that HfN has grown on both MgO and Si substrates with a cube-on-cube orientation relationship. The epitaxial quality of HfN on MgO is much higher than that of HfN on Si, which is mainly due to that the large lattice mismatch between HfN and Si (~17.7%) and the relatively small mismatch of HfN on MgO (~8%). The HfN films on both MgO and Si substrates show low electrical resistivity (~ 45 μΩ-cm) and good diffusion barrier properties based on preliminary annealing experiments. These results suggest that HfN is a promising candidate as diffusion barriers for Cu interconnects.

In Chapter VI, epitaxial cubic HfN (B1-NaCl structure) was deposited on Si(001) substrates by using a thin TiN buffer layer. The XRD results show that the lattice parameter of the highly textured cubic HfN (B1-NaCl structure) has strong correlation with the TiN buffer layer thickness. Low magnification TEM images for all the stacks show that the HfN and TiN layers are uniform and free of intermixing at both HfN/TiN and TiN/Si interfaces. The diffusion barrier property of the HfN/TiN stacks was studied by high resolution TEM, showing a Cu diffusion distance of 2 ~ 3 nm for vacuum annealing at 500°C for 30 minutes. The high crystallinity, low resistivity, good thermal stability and excellent Cu diffusion barrier property of the cubic HfN/TiN stacks prove their potential application as next generation diffusion barrier for Cu metallization.

In Chapter VII, the Cu diffusion into epitaxial HfN thin films was studied by high resolution TEM and the results were fitted to an Arrhenius equation based on the diffusion coefficients calculated at different annealing temperatures. HRTEM study demonstrates a good Cu diffusion barrier property for HfN with the Cu diffusion depth up to ~5 nm at an annealing temperature of 650°C for 30 minutes. This diffusion depth is much smaller than TaN 15 nm at 700°C annealing [16]. The diffusivity expression was determined to be $D = (2.4 \pm 0.6) \times 10^{-14} \exp\left[-(0.52 \pm 0.3) eV / k_B T\right] cm^2 s^{-1}$ for temperatures from 500 to 650°C. Epitaxial HfN is a promising candidate for Cu diffusion barrier for Cu interconnects.

In Chapter VIII, a systematic study by using first-principles calculations was carried out. The calculations focused on the structural, elastic, and electronic properties of the selected transition metal nitrides TiN, TaN and HfN. The structural properties for the crystal structure B1 are in good agreement with experimental results; on the other hand, the calculated elastics and electronics properties are comparable to those of similar documented calculations. The properties of the crystal structures B2 and B3 are also calculated and, interestingly, their properties explain their non-stable behavior.

Finally, the electronic hybrid behavior is well explained by the density of states, with covalent and ionic bond contribution between nitrogen and the metal. Finally, by using computational techniques such as density functional theory, new materials properties can be predicted or can clarify the ambiguity from different experimental methods.

REFERENCES

[1] H.O. Pierson, Handbook of Refractory Carbides and Nitrides, Noyes, Westwood NJ, 1996.

[2] E.K. Storms, A Critical Review of Refractories, Los Alamos Scientific Laboratory, Los Alamos NM, 1964.

[3] S. Cho, K. Lee, P. Song, H. Jeon, Y. Kim, Jpn. J. Appl. Phys., Part 1 46 (2007), 4085.

[4] A.E. Kaloyeros, E. Eisenbraun, Annual Review of Materials Science 30 (2000), 363.

[5] H. Kim, J. Vac. Sci. Technol., B 21 (2003), 2231.

[6] R. Nowak, C.L. Li, Thin Solid Films 305 (1997), 297.

[7] K. Postava, M. Aoyama, T. Yamaguchi, Appl. Surf. Sci. 175 (2001), 270.

[8] Y. Wang, C.H. Zhao, Z.X. Song, F. Cao, D.W. Yang, Appl. Surf. Sci. 253 (2007), 8858.

[9] I.W. Park, K.H. Kim, Journal of Materials Processing Technology 130 (2002), 254.

[10] J. Park, D.J. Kim, Y.K. Kim, K.H. Lee, K.H. Lee, H. Lee, S. Ahn, Thin Solid Films 435 (2003), 102.

[11] A. Horling, L. Hultman, M. Oden, J. Sjolen, L. Karlsson, J. Vac. Sci. Technol., A 20 (2002), 1815.

[12] A. Kimura, H. Hasegawa, K. Yamada, T. Suzuki, J. Mater. Sci. Lett. 19 (2000), 601.

[13] J. Musil, H. Hruby, Thin Solid Films 365 (2000), 104.

[14] S.T. Oyama (Ed.), The Chemistry of Transition Metal Carbides and Nitrides, Chapman & Hall, Glasgow UK, 1996.

[15] H. Kim, A.J. Kellock, S.M. Rossnagel, J. Appl. Phys. 92 (2002), 7080.

[16] H. Wang, A. Tiwari, A. Kvit, X. Zhang, J. Narayan, Appl. Phys. Lett. 80 (2002), 2323.

[17] H. Wang, A. Tiwari, X. Zhang, A. Kvit, J. Narayan, Appl. Phys. Lett. 81 (2002), 1453.

[18] R.A. Araujo, J. Yoon, X. Zhang, H. Wang, Thin Solid Films 516 (2008), 5103.

[19] ITRS, The International Technology Roadmap for Semiconductors Update, 2007. http://www.itrs.net

[20] K. Kim, Advanced Metallization and Interconnect Systems for ULSI Applications, Pittsburgh, 1995, p. 281.

[21] C.A. Chang, C.K. Hu, Appl. Phys. Lett. 57 (1990), 617.

[22] S.Q. Wang, I. Raaijmakers, B.J. Burrow, S. Suthar, S. Redkar, K.B. Kim, J. Appl. Phys. 68 (1990), 5176.

[23] M. Danek, M. Liao, J. Tseng, K. Littau, D. Saigal, H. Zhang, R. Mosely, M. Eizenberg, Appl. Phys. Lett. 68 (1996), 1015.

[24] A. Paranjpe, M. Islamraja, J. Vac. Sci. Technol., B 13 (1995), 2105.

[25] J.Y. Yun, S.W. Rhee, Thin Solid Films 312 (1998), 24.

[26] A. Gupta, H. Wang, A. Kvit, G. Duscher, J. Narayan, J. Appl. Phys. 93 (2003), 5210.

[27] M.B. Chamberlain, Thin Solid Films 91 (1982), 155.

[28] L. Hultman, Vacuum 57 (2000), 1.

[29] K.Y. Lim, Y.S. Lee, Y.D. Chung, I.W. Lyo, C.N. Whang, J.Y. Won, H.J. Kang, Appl. Phys. A: Mater. Sci. Process. 70 (2000), 431.

[30] M. Moriyama, T. Kawazoe, M. Tanaka, M. Murakami, Thin Solid Films 416 (2002), 136.

[31] M. Takeyama, A. Noya, T. Sase, A. Ohta, K. Sasaki, J. Vac. Sci. Technol., B 14 (1996), 674.

[32] M.T. Wang, Y.C. Lin, M.C. Chen, J. Electrochem. Soc. 145 (1998), 2538.

[33] K.H. Min, K.C. Chun, K.B. Kim, J. Vac. Sci. Technol., B: Microelectron. Nanometer Struct.--Process., Meas., Phenom. 14 (1996), 3263.

[34] A. Noya, K. Sasaki, M. Takeyama, Jpn. J. Appl. Phys., Part 1 32 (1993), 911.

[35] B. Chin, P.J. Ding, B.X. Sun, T. Chiang, D. Angelo, I. Hashim, Z. Xu, S. Edelstein, F.S. Chen, Solid State Technology 41 (1998), 141.

[36] M.H. Tsai, S.C. Sun, H.T. Chiu, C.E. Tsai, S.H. Chuang, Appl. Phys. Lett. 67 (1995), 1128.

[37] X.M. Chen, G.G. Peterson, C. Goldberg, G. Nuesca, H.L. Frisch, A.E. Kaloyeros, B. Arkles, J. Sullivan, J. Mater. Res. 14 (1999), 2043.

[38] A.E. Kaloyeros, X.M. Chen, T. Stark, K. Kumar, S. Seo, G.G. Peterson, H.L. Frisch, B. Arkles, J. Sullivan, J. Electrochem. Soc. 146 (1999), 170.

[39] X.M. Chen, H.L. Frisch, A.E. Kaloyeros, B. Arkles, J. Sullivan, J. Vac. Sci. Technol., B 17 (1999), 182.

[40] T. Oku, E. Kawakami, M. Uekubo, K. Takahiro, S. Yamaguchi, M. Murakami, Appl. Surf. Sci. 99 (1996), 265.

[41] L. Jiang, P. He, G. He, X. Zong, C. Lee, Jpn. J. Appl. Phys., Part 1 41 (2002), 6525.

[42] S.W. Loh, D.H. Zhang, C.Y. Li, R. Liu, A.T.S. Wee, Thin Solid Films 462-63 (2004), 240.

[43] J. Nazon, B. Fraisse, J. Sarradin, S.G. Fries, J.C. Tedenac, N. Frety, Appl. Surf. Sci. 254 (2008), 5670.

[44] A.W. Weimer (Ed.), Carbide, Nitride and Boride Materials Synthesis and Processing, Chapman & Hall, London, 1997.

[45] L.I. Johansson, Surf. Sci. Rep. 21 (1995), 179.

[46] A.E. Palty, H. Margolin, J.P. Nielsen, Transactions of the American Society for Metals 46 (1954), 312.

[47] A. Brager, Acta Physicochimica URSS 11 (1939), 617.

[48] L.E. Toth, Transition Metal Nitrides and Carbides, Academic Press, London, 1971.

[49] N. Terao, Jpn. J. Appl. Phys., Part 1 10 (1971), 248.

[50] D. Gerstenberg, C.J. Calbick, J. Appl. Phys. 35 (1964), 402.

[51] J.S. Becker, E. Kim, R.G. Gordon, Chem. Mater. 16 (2004), 3497.

[52] Y. Ando, I. Sakamoto, I. Suzuki, S. Maruno, Thin Solid Films 344 (1999), 246.

[53] B.O. Johansson, J.E. Sundgren, U. Helmersson, J. Appl. Phys. 58 (1985), 3112.

[54] M.Y. Liao, Y. Gotoh, H. Tsuji, J. Ishikawa, J. Vac. Sci. Technol., A 22 (2004), 214.

[55] E. Langereis, H.C.M. Knoops, A.J.M. Mackus, F. Roozeboom, M.C.M. van de Sanden, W.M.M. Kessels, J. Appl. Phys. 102 (2007).

[56] C. Stampfl, W. Mannstadt, R. Asahi, A.J. Freeman, Phys. Rev. B: Condens. Matter Mater. Phys. 6315 (2001).

[57] C.N. Berglund, W.E. Spicer, Phys. Rev. A: At., Mol., Opt. Phys. 136 (1964), 1030.

[58] B. Feuerbacher, R.F. Willis, Journal of Physics C: Solid State Physics 9 (1976), 169.

[59] C. Kral, W. Lengauer, D. Rafaja, P. Ettmayer, J. Alloys Compd. 265 (1998), 215.

[60] J.T. Cheung, H. Sankur, Crc Critical Reviews in Solid State and Materials Sciences 15 (1988), 63.

[61] H.M. Smith, A.F. Turner, Appl. Opt. 4 (1965), 147.

[62] X.D. Wu, X.X. Xi, Q. Li, A. Inam, B. Dutta, L. Didomenico, C. Weiss, J.A. Martinez, B.J. Wilkens, S.A. Schwarz, J.B. Barner, C.C. Chang, L. Nazar, T. Venkatesan, Appl. Phys. Lett. 56 (1990), 400.

[63] D.B. Chrisey, G.K. Hubler (Eds.), Pulsed Laser Deposition of Thin Films, John Wiley & Sons, Inc., New York NY, 1994.

[64] R.K. Singh, O.W. Holland, J. Narayan, J. Appl. Phys. 68 (1990), 233.

[65] R.K. Singh, J. Narayan, Phys. Rev. B: Condens. Matter Mater. Phys. 41 (1990), 8843.

[66] C. Suryanarayana, M.G. Norton, X-Ray Diffraction: A Practical Approach, Springer, New York NY, 1998.

[67] B.D. Cullity, Elements of X-ray Diffraction, Addison-Wesley, Reading MA, 1978.

[68] J. Als-Nielsen, D. McMorrow, Elements of Modern X-ray Physics, John Wiley & Sons Ltd., West Sussex UK, 2001.

[69] P.J. Goodhew, F.J. Humphreys, R. Beanland, Electron Microscopy and Analysis, Taylor & Francis, London-New York, 2000.

[70] J.J. Bozzola, L.D. Russell, Electron Microscopy: Principles and Techniques for Biologists, Bartlett Inc., Sudbury MA, 1999.

[71] L.B. Valdes, Proceedings of the Institute of Radio Engineers 42 (1954), 420.

[72] D.K. Schroder, Semiconductor Material and Device Characterization, John Wiley & Sons Inc., New York NY, 2006.

[73] G.S. Chen, S.T. Chen, J. Appl. Phys. 87 (2000), 8473.

[74] G.S. Chen, S.T. Chen, L.C. Yang, P.Y. Lee, J. Vac. Sci. Technol., A 18 (2000), 720.

[75] G.S. Chen, S.C. Huang, S.T. Chen, T.J. Yang, P.Y. Lee, J.H. Jou, T.C. Lin, Appl. Phys. Lett. 76 (2000), 2895.

[76] S.P. Murarka, Materials Science and Engineering: R: Reports 19 (1997), 87.

[77] M. Stavrev, C. Wenzel, A. Moller, K. Drescher, Appl. Surf. Sci. 91 (1995), 257.

[78] ITRS, The International Technology Roadmap for Semiconductors Update, 2006. http://www.itrs.net

[79] A. Georgakilas, P. Panayotatos, J. Stoemenos, J.L. Mourrain, A. Christou, J. Appl. Phys. 71 (1992), 2679.

[80] H. Lu, W.J. Schaff, J. Hwang, H. Wu, G. Koley, L.F. Eastman, Appl. Phys. Lett. 79 (2001), 1489.

[81] C.I. Park, J.H. Kang, K.C. Kim, E.K. Suh, K.Y. Lim, K.S. Nahm, J. Cryst. Growth 224 (2001), 190.

[82] D. Wang, Y. Hiroyama, M. Tamura, M. Ichikawa, S. Yoshida, Appl. Phys. Lett. 77 (2000), 1846.

[83] H. Wang, A. Sharma, A. Kvit, Q. Wei, X. Zhang, C.C. Koch, J. Narayan, J. Mater. Res. 16 (2001), 2733.

[84] H. Kim, C. Detavenier, O. van der Straten, S.M. Rossnagel, A.J. Kellock, D.G. Park, J. Appl. Phys. 98 (2005).

[85] H. Wang, A. Gupta, A. Tiwari, X. Zhang, J. Narayan, J. Electron. Mater. 32 (2003), 994.

[86] B.O. Johansson, U. Helmersson, M.K. Hibbs, J.E. Sundgren, J. Appl. Phys. 58 (1985), 3104.

[87] J. Lannon, C. Pace, S. Goodwin, S. Solomon, P. Bryant, J. Vac. Sci. Technol., A 22 (2004), 1730.

[88] M.H. Lin, S.Y. Chiou, Jpn. J. Appl. Phys., Part 1 43 (2004), 3340.

[89] S. Shinkai, K. Sasaki, Jpn. J. Appl. Phys., Part 1 38 (1999), 2097.

[90] K.L. Ou, S.Y. Chiou, M.H. Lin, R.Q. Hsu, J. Electrochem. Soc. 152 (2005), G138.

[91] R.A. Araujo, X. Zhang, H. Wang, J. Electron. Mater. (2008), in press.

[92] H.S. Seo, T.Y. Lee, I. Petrov, J.E. Greene, D. Gall, J. Appl. Phys. 97 (2005).

[93] R.A. Araujo, X. Zhang, H. Wang, J. Vac. Sci. Technol., B (2008), in press.

[94] S. Shinkai, K. Sasaki, H. Yanagisawa, Y. Abe, Jpn. J. Appl. Phys., Part 1 42 (2003), 6518.

[95] D.I. Bazhanov, A.A. Knizhnik, A.A. Safonov, A.A. Bagatur'yants, M.W. Stoker, A.A. Korkin, J. Appl. Phys. 97 (2005), 044108.

[96] D.I. Bazhanov, A.A. Safonov, A.A. Bagatur'yants, A.A. Korkin, Micro and Nanoelectronics 2003, Society of Photo-Optical Instrumentation Engineers, 2004, p. 418.

[97] W.Y. Ching, Y.-N. Xu, L. Ouyang, Phys. Rev. B: Condens. Matter Mater. Phys. 66 (2002), 235106.

[98] U. Figueroa, O. Salas, J. Oseguera, Thin Solid Films 469-470 (2004), 295.

[99] W.R.L. Lambrecht, M.S. Miao, P. Lukashev, 49th Annual Conference on Magnetism and Magnetic Materials, AIP, Jacksonville, FL (USA), 2005, p. 10D306.

[100] G. Lopez, M.H. Staia, Surf. Coat. Technol. 200 (2005), 2092.

[101] Z. Wu, X.-J. Chen, V.V. Struzhkin, R.E. Cohen, Phys. Rev. B: Condens. Matter Mater. Phys. 71 (2005), 214103.

[102] A. Ferreira da Silva, N. Souza Dantas, J.S. de Almeida, R. Ahuja, C. Persson, J. Cryst. Growth 281 (2005), 151.

[103] A. Gusev, Doklady Akademil nauk 357 (1997), 490.

[104] Q. Hu, T. Noda, H. Tanigawa, T. Yoneoka, S. Tanaka, Nuclear Instruments and Methods in Physics Research Section B: Beam Interactions with Materials and Atoms 191 (2002), 536.

[105] F. Levy, P. Hones, P.E. Schmid, R. Sanjines, M. Diserens, C. Wiemer, Surf. Coat. Technol. 120-121 (1999), 284.

[106] E.F.J.W. M. Lerch, Zeitschrift für anorganische und allgemeine Chemie 622 (1996), 367.

[107] N.E. Christensen, Phys. Rev. B: Condens. Matter Mater. Phys. 50 (1994), 4397.

[108] L.E. Conroy, A.N. Christensen, J. Solid State Chem. 20 (1977), 205.

[109] L.D. Locker, C.L. Naegele, F. Vratny, J. Electrochem. Soc. 118 (1971), 1856.

[110] V.F. Petrunin, N.I. Sorokin, Inorganic Materials 18 (1982), 1733.

[111] U. Helmersson, B.O. Johansson, J.E. Sundgren, H.T.G. Hentzell, P. Billgren, J. Vac. Sci. Technol., A 3 (1985), 308.

[112] T. Jamal, R. Nimmagadda, R.F. Bunshah, Thin Solid Films 73 (1980), 245.

[113] W. Schintlmeister, O. Pacher, K. Pfaffinger, T. Raine, J. Electrochem. Soc. 123 (1976), 924.

[114] D. Edelstein, J. Heidenreich, R. Goldblatt, W. Cote, C. Uzoh, N. Lustig, P. Roper, T. McDevitt, W. Motsiff, A. Simon, J. Dukovic, R. Wachnik, H. Rathore, R. Schulz, L. Su, S. Luce, J. Slattery, 1997, p. 773.

[115] P.E. Blochl, O. Jepsen, O.K. Andersen, Phys. Rev. B: Condens. Matter Mater. Phys. 49 (1994), 16223.

[116] G. Kresse, D. Joubert, Phys. Rev. B: Condens. Matter Mater. Phys. 59 (1999), 1758.

[117] C. Kittel, Introduction to Solid State Physics, Wiley, New York NY, 2005.

[118] M.J. Mehl, Phys. Rev. B: Condens. Matter Mater. Phys. 47 (1993), 2493.

[119] X.-J. Chen, V.V. Struzhkin, Z. Wu, M. Somayazulu, J. Qian, S. Kung, A.N. Christensen, Y. Zhao, R.E. Cohen, H.-k. Mao, R.J. Hemley, PNAS 102 (2005), 3198.

[120] J.H. Wang, S. Yip, S.R. Phillpot, D. Wolf, Phys. Rev. Lett. 71 (1993), 4182.

[121] S.H. Jhi, J. Ihm, S.G. Louie, M.L. Cohen, Nature 399 (1999), 132.

[122] J.O. Kim, J.D. Achenbach, P.B. Mirkarimi, M. Shinn, S.A. Barnett, J. Appl. Phys. 72 (1992), 1805.

[123] J.Q. Li, Y.F. Zhang, S.C. Xiang, Y.N. Chiu, Journal of Molecular Structure-Theochem 530 (2000), 209.

[124] R. Ahuja, O. Eriksson, J.M. Wills, B. Johansson, Phys. Rev. B: Condens. Matter Mater. Phys. 53 (1996), 3072.

[125] M. Marlo, V. Milman, Phys. Rev. B: Condens. Matter Mater. Phys. 62 (2000), 2899.

[126] S. Nagao, K. Nordlund, R. Nowak, Phys. Rev. B: Condens. Matter Mater. Phys. 73 (2006).

VITA

Name: Roy Adolfo Araujo

Address: 706 Jack E. Brown Building, College Station, Texas 77843-3128

Email: raraujo@tamu.edu, roy.araujo@gmail.com

Education:

B.S., Electronics Engineering, Universidad Nacional de Ingenieria,2001

M.E., Electrical and Computer Engineering, University of South Carolina, 2004

Ph.D. Electrical and Computer Engineering, Texas A&M University, 2008

Publications

1. R.A. Araujo, X. Zhang, and H. Wang, (2008), submitted.
2. R.A. Araujo, X. Zhang, and H. Wang, J. Vac. Sci. Technol., B (2008), in press.
3. R.A. Araujo, X. Zhang, and H. Wang, J. Electron. Mater. (2008), in press.
4. R.A. Araujo, J. Yoon, X. Zhang, and H. Wang, Thin Solid Films 516 (2008), 5103.
5. J. Yoon, R.A. Araujo, and H. Wang, Appl. Surf. Sci. 254 (2007), 266.
6. H. Wang, R.A. Araujo, J.G. Swadener, Y. Wang, X. Zhang, E.G. Fu and T. Cagin, Nucl. Instrum. Methods Phys. Res., B 261 (2007), 1162.